Potential depletion of ozone in the mid-latitude lowermost stratosphere in summer under geoengineering conditions

Sabine Robrecht

JÜLICH
Forschungszentrum

Schriften des Forschungszentrums Jülich
Reihe Energie & Umwelt / Energy & Environment   Band / Volume 545

Potential depletion of ozone in the mid-latitude lowermost stratosphere in summer under geoengineering conditions

Sabine Robrecht

Abstract

The world's climate is changing, largely because of anthropogenic emissions of greenhouse gases (GHG). Increasing atmospheric GHG concentrations result in global warming, which changes habitats all around the globe. For limiting the risks of global warming, a supporting option could be the application of sulfate geoengineering. The concept of sulfate geoengineering is to inject sulfate aerosols into the stratosphere extenuating the sunlight, which reaches and thus warms the surface of the Earth. In this way, the surface temperature could possibly be kept at today's level avoiding negative consequences of GHG induced global warming.

However, sulfate geoengineering is not free of risks and these potential risks have to be explored before the application of geoengineering can be considered. This thesis is aimed at assessing the risk of ozone loss known from polar winter to occur in the mid-latitude lowermost stratosphere in summer as a potential side effect of sulfate geoengineering. These ozone loss processes were further proposed to potentially occur in the mid-latitudes for today's conditions in combination with convective overshooting events transporting water vapour into the dry stratosphere. If these ozone loss processes occur, the UV-exposure in the densely populated mid-latitude northern hemisphere would increase in summer.

In this thesis, the chemical ozone loss mechanism in the mid-latitudes and its sensitivity to a variety of conditions is extensively analysed by conducting box-model simulations with the Chemical Lagrangian Model of the Stratosphere (CLaMS). This analysis shows that a threshold in water vapour has to be exceeded for stratospheric ozone loss to occur. This water vapour threshold is mainly determined by the temperature and sulfate content of the air mass. The extent of ozone loss depends on available chlorine and bromine concentrations and the duration of the time period over which chlorine activation can be maintained. However, a simulation for conditions over North America, which are realistic but selected to be most suitable for this ozone loss process, did not show significant chlorine activation.

Moreover, the likelihood for this ozone loss process to occur today or in future scenarios is determined considering both climate change and an additional application of sulfate geoengineering. Therefore, atmospheric conditions causing chlorine activation are determined based on CLaMS box-model simulations and compared with conditions found in the lowermost stratosphere in results of climate simulations using the Geoengineering Large Ensemble Simulations (GLENS). Extensive sensitivity studies in this thesis show a 2–3 times higher likelihood for chlorine activation in the future scenario with sulfate geoengineering than for today. However, even if geoengineering were applied, the likelihood for chlorine activation to occur above North America remains low (max. $\sim$3.3%), destroying less than 0.4% of ozone in the lowermost stratosphere. An upper limit for total ozone column reduction of 0.11 DU (less than 0.1% of column ozone) is deduced in this thesis.

Overall, this thesis demonstrates a negligible risk for chlorine catalysed ozone loss to occur in the lowermost stratosphere over North America in summer for conditions today and in future, even if sulfate geoengineering were applied. This is an important contribution to assessing the risks of a potential application of sulfate geoengineering in future.

Kurzfassung

Das Klima der Erde ändert sich größtenteils aufgrund anthropogener Treibhausgasemissionen. Die ansteigenden Treibhausgaskonzentrationen in der Atmosphäre führen zu einer globalen Erderwärmung, welche Lebensräume überall auf der Erde verändert. Um die Risiken einzudämmen, welche von der globalen Erderwärmung ausgehen, könnte die Anwendung von „Sulfat Geoengineering" eine unterstüzende Maßnahme sein. Die Idee hiervon ist es, durch das Einbringen von Sulfataerosolen in die Stratosphäre Sonnenlicht, welches die Erdoberfläche erreicht und dadurch erwärmen kann, abzuschwächen. Dadurch würde vermieden werden, dass die Temperatur an der Erdoberfläche ansteigt und so würden negative Konsequenzen der globalen Erderwärmung verhindert.

Allerdings birgt Sulfat Geoengineering auch Risiken, welche vor einer möglichen Anwendung erforscht werden müssen. Das Ziel dieser Doktorarbeit ist es, das Risiko für chemischen Ozonverlust in der untersten Stratosphäre der mittleren Breiten während des Sommers zu beurteilen. Es wurde vorgeschlagen, dass chemische Ozonabbauzyklen, welche jährlich im polaren Winter auftreten, auch in den mittleren Breiten im Zusammenhang mit Sulfat Geoengineering oder konvektiven Ereignissen auftreten können, welche Wasserdampf in die trockene unterste Stratosphäre transportieren. Ein Auftreten dieser Ozonabbauzyklen im Sommer der mittleren Breiten könnte zu einer erhöhten UV-Belastung an der Erdoberfläche der dichtbesiedelten Nordhemisphäre führen.

In dieser Arbeit wird der Ozonabbaumechanismus und dessen Sensitivität gegenüber verschiedenen Bedingungen für die mittleren Breiten analysiert, indem Box-Modell-Simulationen mit dem „Chemical Lagrangian Model of the Stratosphere" (CLaMS) durchgeführt werden. Durch diese Analyse wird ein Schwellwert im Wasserdampf Mischungsverhältnis identifiziert, welcher überschritten und erhalten werden muss, damit der Ozonabbaumechanismus auftreten kann. Dieser Schwellwert hängt hauptsächlich von der Temperatur und dem Schwefelgehalt in der Stratosphäre ab. Die Menge des zerstörten Ozons wird dabei vorwiegend vom vorhandenen Chlor und Brom-Mischungsverhältnis sowie von der Länge des Zeitraums kontrolliert, über welchen die Chloraktivierung erhalten bleibt. Eine Simulation basierend auf realistischen Bedingungen, welche dahingehend ausgewählt worden sind Chloraktivierung am wahrscheinlichsten zu ermöglichen, hat allerdings keine relevante Chloraktivierung gezeigt.

Zusätzlich wird im Rahmen dieser Doktorarbeit die Wahrscheinlichkeit bestimmt, dass dieser Ozonabbaumechanismus für heutige und zukünftige Bedingungen auftritt. Dabei wird sowohl ein Klimawandelszenario als auch die zusätzliche Anwendung von Geoengineering analysiert basierend auf Ergebnissen von Klimasimulationen („Geoengineering Large Ensemble Simulations" (GLENS)). Atmosphärische Bedingungen, die zu Chloraktivierung führen, werden mithilfe von CLaMS Box-Modell-Simulationen identifiziert und mit den Bedingungen in der unteren Stratosphäre aus den Ergebnissen der Klimasimulationen verglichen. Durch umfangreiche Sensitivitätstest im Rahmen dieser Arbeit wird gezeigt, dass die Anwendung von Geoengineering in Zukunft zu einer 2–3 mal höhren Wahrscheinlichkeit als für heutige Bedingungen führt, dass der untersuchte Ozonabbaumechanismus auftritt. Dennoch ist die

Wahrscheinlichkeit, dass unter Anwendung von Sulfat Geoengineering Chloraktivierung über zentral Nordamerika auftritt sehr gering (max. ∼3.3%), sodass weniger als 0.4% des Ozons in der unteren Stratosphäre zerstört werden. Dies entspricht einer Obergrenze von ∼0.11 DU (= weniger als 0.1%) der Ozonsäule.

Zusammenfassend wird im Rahmen dieser Doktorarbeit erstmalig gezeigt, dass das Risiko für erhöhten chemischen Ozonabbau, ähnlich dem des polaren Winters, in der unteren Stratosphäre im Sommer über Nordamerika für heutige als auch unter Berücksichtigung von möglichen zukünftigen Bedigung wie „Sulfat Geoengineering" zu vernachlässigen ist. Dies ist ein wichtiger Beitrag für die zukünftige Bewertung möglicher Geoengineering Techniken.

Danksagung

Es gibt viele Menschen, die in unterschiedlicher Art und Weise zu dieser Arbeit beigetragen haben. Ich möchte hier die Gelegenheit nutzen, mich bei ein paar dieser Menschen für ihren Beitrag zu dieser Arbeit zu bedanken.

Vor allem möchte ich PD Dr. Rolf Müller und Dr. Bärbel Vogel für die Möglichkeit danken, meine Dissertation in einem so interessanten Themengebiet anfertigen zu können. Durch ihre fachliche Unterstützung und die vielen Ratschläge haben sie wesentlich zum gelingen dieser Arbeit beigetragen.

Diese Arbeit entstand am Forschungszentrum Jülich im Institut für Stratosphärenforschung (IEK-7). Hier möchte ich Prof. Dr. Martin Riese für die Aufnahme ins Institut danken, wodurch mir eine gute und erfahrungsreiche Zeit in Jülich ermöglicht worden ist. Zudem möchte ich mich bei Prof. Dr. Thorsten Benter dafür bedanken, dass er die Betreuung dieser Arbeit an der Universität Wuppertal übernommen hat.

Auch das Wirken von Dr. Simone Tilmes soll hier nicht unerwähnt bleiben. Simone war für mich nicht nur ein zuverlässiger Ansprechpartner bei fachlichen Fragen sondern war bei meinem Auslandaufenthalt in Boulder (CO) auch darüber hinaus für mich da.

Ich möchte all meinen Kollegen am IEK-7 für die technische Unterstützung, die wissenschaftlichen Diskussionen sowie die positive Arbeitsatmosphäre danken. Durch die offene Art habe ich die vergangenen Jahre am Institut sehr genossen.

Zu guter Letzt möchte ich meiner Familie danken, dass sie mich bis hierher immer unterstützt hat. Auch möchte ich meinen Freunden in Jülich danken, mit denen ich mich über viele Themen austauschen konnte und die immer hilfsbereit waren, wodurch eine Art verrückte aber liebenswerte Familie entstanden ist.

Contents

List of Figures

Appendix **155**

List of Tables

Chapter 1

Motivation

The Earth's climate is changing during the last decades. This climate change is largely caused by an increase of greenhouse gases (GHG) – in particular carbon dioxide (CO_2), methane (CH_4) and nitrous oxide (N_2O) – in the Earth's atmosphere. Human made GHG emissions increase because of a growing economy and the growing world population. Today, concentrations of CO_2, CH_4 and N_2O are significantly higher than in the last 800,000 years (Pachauri et al., 2014).

Effects of the climate change are noticeable all around the globe: The atmosphere and the oceans are warming, the sea level rises, areas covered with snow and ice are diminished. Animals move to other geographic regions and in some regions the tree mortalities increase (Pachauri et al., 2014). Climate change causes more intense and more frequent extreme weather events and thus may be considered as the cause of a higher frequency of storms, floodings, droughts, wildfires and pest infestations in different regions of the Earth. Thus, life everywhere around the globe is affected by the human made climate change. The effect of increasing CO_2 on the Earth's climate is expected to last at least 1000 years (Solomon et al., 2009) and continuous emission of GHG will prolong the effects that climate change has (Pachauri et al., 2014).

Mitigation of GHG emissions and adaptation can limit the risks of climate change. A supporting option could be the application of geoengineering. The term geoengineering comprises several techniques to consciously interfere with the Earth's climate for attenuating the effects of climate change (SPP1689, 2019). In general, geoengineering

techniques are divided into two approaches: Carbon Dioxide Removal (CDR) and Solar Radiation Management (SRM). The focus of CDR is on capturing atmospheric CO_2. The concept of SRM is to manipulate the radiative energy balance of the Earth, e.g. through reducing the sun light, which reaches the surface of the Earth and thus would cause a warming of the Earth (SPP1689, 2019). In this thesis, the focus is on the SRM approach generally referred to as "sulfate geoengineering". Sulfate particles injected into the stratosphere would reflect sun light before reaching the surface of the Earth and thus cool the global temperatures (e.g. Crutzen, 2006; Tilmes et al., 2009). This potentially leads to a reduction of the sea level rise and ice melting. However, this type of geoengineering does not adress other effects of the CO_2 rise in the atmosphere, such as the ocean acidification (SPP1689, 2019).

The application of geoengineering is not free of risks. As an example, sulfate geoengineering may cause polar stratospheric ozone depletion or perturbations of the hydrological cycle (Tilmes et al., 2008; Robock et al., 2009; SPP1689, 2019). Stopping sulfate geoengineering at some point in the future would lead to a rapid warming (Robock et al., 2009; Llanillo et al., 2010). Furthermore, moral conflicts as well as legal and socio-economic aspects have to be taken into account as the question arises who is allowed to apply geoengineering and who would be responsible (Robock et al., 2009). Before deciding for or against geoengineering the potential benefits have to be carefully assessed with respect to the risks. And yet, there are multiple unknown side effects of sulfate geoengineering.

In this thesis one potential side effect of sulfate geoengineering first suggested by Anderson et al. (2012) is investigated extensively. They proposed potential ozone destruction similar to that known from polar late winter and early spring to occur, which could significantly reduce the stratospheric ozone layer in the lowermost stratosphere during North American summer. Since the stratospheric ozone layer absorbs UV-light emitted by the sun, a reduction of stratospheric ozone would increase the risk of radiative damage for plants, wildlife and humans. Anderson et al. (2012) assumed this ozone destruction to be caused by enhancements of water vapour connectively injected into the stratosphere and they expected sulfate geoengineering to increase the likelihood for

considerable ozone destruction in mid-latitude summer.

The aim of this thesis is to assess the risk of this ozone loss process to occur in the mid-latitude lowermost stratosphere as a potential side effect of sulfate geoengineering. Therefore

- first, the chemical mechanism is investigated in detail.

- Further, the sensitivity of this ozone loss process on a variety of conditions is analysed through model simulations.

- Based on these results, the likelihood for this ozone loss process to occur today, in a future with global warming and in a future, where sulfate geoengineering is applied, is determined

- and the impact of the ozone loss process on ozone in particular in the altitude of the lowermost stratosphere as well as on the ozone column is deduced.

In the study by Anderson et al. (2012), a range of initial mixing ratios for HCl and ClONO$_2$ with rather high concentrations of 850 pptv HCl and 150 pptv ClONO$_2$ were assumed. Here, the chemical mechanism is analysed simulating stratospheric chemistry based on aircraft measurements above North America during summertime (see Sec. 4.2 and 4.3). From this investigation also the likelihood for the ozone loss mechanism proposed by Anderson et al. (2012) to occur today is estimated. The likelihood for ozone loss to occur in future scenarios assuming climate change and the additional application of sulfate geoengineering is determined combining chemical box-model simulations and results of a state-of-art global climate model (see Sec. 5.3.2). Likewise, the relevance of this ozone loss mechanism for the stratospheric ozone abundance is deduced (see Sec. 5.3.3 and 5.3.4).

The Chapter 2 introduces the basics of atmospheric chemistry and dynamics. Furthermore, the concept of sulfate geoengineering is explained in some detail and the potential impact of both climate change and sulfate geoengineering on the composition of the lowermost stratosphere is described (see Sec. 2.4). In Chapter 3, the used numerical models are introduced. The focus of Chapter 4 is on the chemical mechanism based on measurements today and the sensitivity of this mechanism to various conditions. In Chapter 5, the likelihood for this ozone loss mechanism to occur in future and today is

determined as well as its relevance for ozone in the stratosphere. Finally, the results are concluded in Chapter 6.

The main parts of this thesis were published in two articles in peer-reviewed scientific journals:

Robrecht, S., Vogel, B. Grooß, J.-U., Rosenlof, K., Thornberry, T., Rollins, A., Krämer, M., Christensen, L. and Müller, R.: Mechanism of ozone loss under enhanced water vapour conditions in the mid-latitude lower stratosphere in summer, Atmos. Chem. Phys., 19, 5805–5833, doi:10.5194/acp-19-5805-2019, 2019.

Robrecht, S., Vogel, B., Tilmes, S., and Müller, R.: Potential of future stratospheric ozone loss in the mid-latitudes under global warming and sulfate geoengineering, Atmos. Chem. Phys., https://doi.org/10.5194/acp-21-2427-2021, 2021.

Chapter 2

Introduction to stratospheric chemistry and dynamics

In this chapter, basics of stratospheric dynamics and chemistry are introduced. Furthermore background information on the concept of sulfate geoengineering is given and the generally expected impact of both climate change and the hypothetical application of sulfate geoengineering on the stratospheric composition is described.

2.1 Basics of stratospheric dynamics

The Earth's atmosphere can be separated in different layers based on the vertical temperature profile. The lowest two layers of the Earth atmosphere are the troposphere and the stratosphere (respectively) with the tropopause separating both layers. Since tropospheric temperatures decrease and stratospheric temperatures increase with the altitude, the most common definition of the tropopause – the thermal tropopause – can be deduced from the changeover between decreasing and rising temperatures. The thermal tropopause is defined as the lowest altitude level at which the temperature decreases to $2\,\mathrm{K/km}$ or less with altitude (WMO, 1957). From this definition, tropopause heights are in the tropics $\sim$16–18 km (100 hPa) and in the polar regions $\sim$6–9 km ($\sim$300 hPa) depending on the season. The tropopause dynamically forms a transport barrier, which in general impedes the stratosphere-troposphere-exchange (Hoinka, 1997).
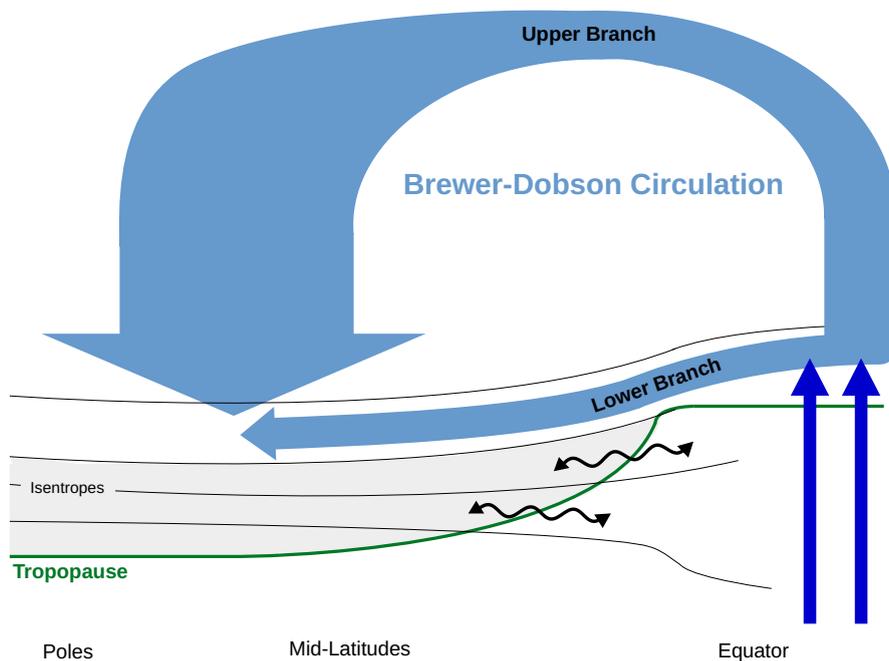
Figure 2.1: Overview on general stratospheric transport processes. The tropopause corresponds to the green line. The dark blue arrows illustrate the troposphere-to-stratosphere transport in the tropics and light blue arrows the Brewer-Dobson-Circulation. Black arrows refer to isentropic transport from the troposphere into the lowermost stratosphere, which is marked by the light grey shading. Addapted from Holton et al. (1995) and Noël et al. (2018).

Tropospheric air enters the stratosphere in the tropics through the cold tropical tropopause layer (Fig. 2.1, dark blue arrows). Subsequent to tropical upwelling, air in the stratosphere is transported poleward and downward so that air leaves the stratosphere and enters the troposphere in the mid- and high-latitudes. This meridional circulation is called Brewer-Dobson-Circulation (BDC), which consists of two branches (Fig. 2.1, light blue arrows) (e.g. Rosenlof et al., 1997; Plumb, 2002; Seinfeld and Pandis, 2006; Bönisch et al., 2011; Butchart, 2014). In the upper branch, air is transported upwards in the tropics into the middle and upper stratosphere before it moves to the poles. The transit time corresponding to the upper branch is in the order of few years. In contrast, the circulation in the lower branch of the BDC is significantly faster with a mean transit time of a year or less (Birner and Bönisch, 2011). In the lower branch

of the BDC, air which recently passed through the tropical tropopause is transported quasi horizontally from the tropics to the mid-latitudes. The chemical composition and the age of stratospheric air depends besides direct transport on mixing of air across stratospheric transport barriers. (e.g. Ploeger et al., 2015a).

On shorter time scales, atmospheric transport is approximately adiabatic, which means there is no exchange of heat between a moved air parcel and its environment. From the second law of thermodynamics can be deduced that adiabatic processes are isentropic as well. Thus, an adiabatically transported air parcel moves along isentropic surfaces, where both pressure and temperature may vary, but the potential temperature (Θ) stays constant. The potential temperature is defined as that temperature, which an air parcel with a certain pressure P and temperature T would have, if the air parcel was adiabatically compressed to a standard pressure (P_0) of 1000 hPa.

$$\Theta = T \cdot \left(\frac{P_0}{P} \right)^{\frac{R}{c_\mathrm{p}}} \tag{2.1}$$

In the adiabatic exponent $\frac{R}{c_\mathrm{p}}$, R is the gas constant and c_p is the specific heat for dry air. The potential temperature increases with altitude independently of the vertical temperature profile, because the pressure decreases exponentially with altitude. Hence, Θ is suitable as an altitude coordinate.

In the stratosphere, horizontal transport is mostly adiabatic, but vertical transport, on longer timescales, is diabatic and intersects isentropic surfaces. Thus, vertical transport requires radiative warming or cooling and is slow compared to isentropic horizontal transport (e.g. Holton et al., 1995; Seinfeld and Pandis, 2006; Birner and Bönisch, 2011).

2.2 The lowermost stratosphere

The transport of air from the troposphere into the stratosphere frequently requires the transport across isentropic surfaces. However, extending from the mid-latitude tropopause up to the height of the tropical tropopause ($\Theta \sim 380$ K) (Fig. 2.1, grey shaded area), the lowermost stratosphere is the only part of the stratosphere, where mixing

with the troposphere is possible along isentropic surfaces (Fig. 2.1, black wavy arrows). Hence, it plays a unique role for the exchange between stratosphere and troposphere (Holton et al., 1995; Rosenlof et al., 1997).

2.2.1   Trace gas correlations

Trace gases, that are mainly released in the troposphere and subject to chemical degradation (e.g. CO), show a high concentration in the troposphere and a low concentration in the stratosphere. Likewise, trace gases mainly formed in the stratosphere (e.g. O_3) have a higher concentration in the stratosphere than in the troposphere. Without mixing between tropospheric and stratospheric air masses, correlations of trace gases mainly released in the troposphere and those mainly produced in the stratosphere form an "L-shape" (e.g. Pan et al., 2004; Vogel et al., 2011), schematically illustrated in Fig. 2.2. The rather horizontal branch (Fig. 2.2) corresponds to tropospheric air masses holding a low concentration of the stratospheric trace gas and the concentration of the tropospheric trace gas is spread over a broader range. The rather vertical branch (Fig. 2.2) likewise corresponds to stratospheric air masses (e.g. Pan et al., 2004; Vogel et al., 2011). In case of ozone as a stratospheric trace gas, an increasing ozone amount is accompanied by an increase in altitude.

In the mid-latitude lowermost stratosphere, an exchange between tropospheric and stratospheric air masses leads to mixing of air masses with different chemical composition. In mixed air parcels, the concentration of the tropospheric tracer is larger than usual for stratospheric conditions and the concentration of the stratospheric tracer is larger than usual in tropospheric air parcels. Thus, this mixing layer between tropospheric and stratospheric air masses generates mixing lines in the tracer-tracer-correlation, which "cut off" the corner of the "L-shape" (Fig. 2.2). The mixing layer is located around the thermal tropopause, but a significant part is located in the lowermost stratosphere (e.g. Pan et al., 2004; Vogel et al., 2011).

Since the correlation of tropospheric and stratospheric trace gases changes strongly in the tropopause region, such correlations can be used to separate stratospheric and tropospheric air masses as well as air masses located in the mixing layer. As an example,
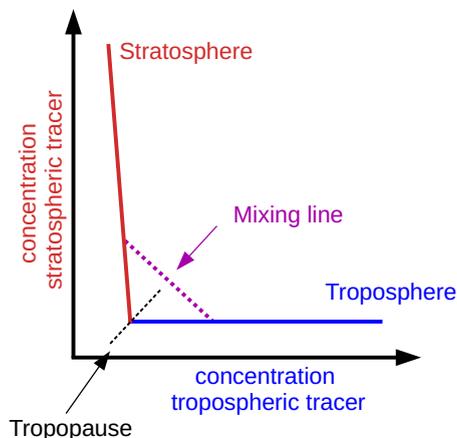
Figure 2.2: Schematic illustration of the trace gas correlation between tropospheric (blue) and stratospheric (red) air masses in the mid-latitude tropopause region. Mixing between tropospheric and stratospheric air masses cause the occurrence of mixing lines in the tracer-tracer correlation (purple). Adapted from Pan et al. (2004).

Pan et al. (2004) assumed air masses with less than $\sim$30 ppbv of the tropospheric trace gas CO to correspond to the stratosphere and air masses with less than 50–100 ppbv O_3 to correspond to the troposphere. Subsequently, air masses holding more than $\sim$100 ppbv O_3 and more than 30 ppbv CO are likely located in the mid-latitude mixing layer. Due to the mixing of tropospheric and stratospheric air masses, unique chemical conditions are created in the lowermost stratosphere.

2.2.2 Water vapour and ozone in the lowermost stratosphere

Lowermost stratospheric water vapour and ozone are especially of interest, because both play an important role for the chemistry and the radiative budget in that region (Holton et al., 1995; Pan et al., 1997) and in addition have an impact on surface climate (e.g. Solomon et al., 2010; Riese et al., 2012). Ozone is mainly formed and located in the stratosphere while the water vapour concentration is much higher in the troposphere than in the stratosphere.

Ozone in the lowermost stratosphere

The ozone concentration in the lowermost stratosphere is dominated by the BDC
transporting ozone formed at higher altitudes downwards (e.g. Brewer, 1949; Ploeger
et al., 2015b). In the mid-latitudes, lowermost stratospheric ozone contributes 6–17%
to the ozone column (Logan, 1999). The ozone column is important as it protects
live on Earth from considerable radiative damage. Exchange of stratospheric air with
tropospheric air masses reduces ozone in the lowermost stratosphere (Wang et al., 1998;
Logan, 1999; Bregman et al., 2001).

Water vapour in the lowermost stratosphere

Water vapour in the mid-latitude stratosphere is controlled by the transport of tropo-
spheric air masses in the tropics to the lower stratosphere and further the distribution
by the Brewer-Dobson-Circulation (e.g. Randel et al., 2004). In the tropics, tropo-
spheric air enters the stratosphere through the cold tropopause. The low tropopause
temperatures yield a "freeze drying" of the entering air masses and thus determine the
amount of water vapour reaching the stratosphere (e.g. Brewer, 1949; Randel et al.,
2004). These dry air masses can be transported isentropically to higher latitudes within
the lower branch of the BDC (Randel et al., 2001, 2004). Alternatively, these air masses
move upwards within the upper branch of the BDC.
Additionally methane enters the stratosphere mainly through the tropical tropopause
layer and is transported upwards within the BDC. This causes an increase of strato-
spheric water vapour at higher altitudes due to methane oxidation (LeTexier et al.,
1988; Rohs et al., 2006). At mid to high latitudes, this moister air of the upper branch
of the BDC air is moved down to lower altitudes, where it mixes with the low water
vapour containing air, which has isentropically moved polewards from the tropics in
the lower branch of the BDC (e.g. Brewer, 1949; Randel et al., 2004; Poshyvailo et al.,
2018). This yields typical mid-latitude lowermost stratospheric water vapour values of
2–6 ppmv, which are drier than in the middle and upper stratosphere.
In the North American summer, a significant amount of tropospheric trace gases can
be transported into the lowermost stratosphere. During the North American Monsoon

(NAM) season, convection followed by advection in the monsoon circulation leads to a transport of water vapour and tropospheric tracers into the lowermost stratosphere (Yan et al., 2019; Schoeberl et al., 2020). An additional source of lowermost stratospheric water vapour are convective overshooting events, which lead to an enhancement of the water vapour mixing ratio above stratospheric background levels. Deep convective storm systems penetrating the tropopause can transport ice crystals into the lowermost stratosphere, where the ice evaporates leading to a local enhancement of water vapour (Hanisco et al., 2007; Schiller et al., 2009; Spang et al., 2015; Herman et al., 2017; Lee et al., 2019).

Hanisco et al. (2007) concluded from stratospheric observations of the H_2O/HDO ratio (HDO is heavy water, where one hydrogen atom is substituted by deuterium) that extra tropical convection significantly accounts for the stratospheric water vapour load. Enhanced water vapour mixing ratios of 10–18 ppmv at an altitude of $\sim$16.5 km (380 K potential temperature, $\sim$100 hPa) (Smith et al., 2017) were observed above North America in summer and were connected with storm systems (Homeyer et al., 2014; Herman et al., 2017; Smith et al., 2017). This findings contribute to the debate on the impact of convectively injected water vapour on mid-latitude stratospheric ozone (Anderson et al., 2012, 2017; Ravishankara, 2012; Clapp and Anderson, 2019).

2.3 Stratospheric ozone chemistry

Stratospheric ozone formation is dominated by the mechanism first described by Chapman (1930). By the absorption of UV-light, oxygen can be photolysed forming $O(^3P)$-radicals (R 1). These can react with oxygen and a third body M (N_2 or O_2) yielding ozone (R 2.) The formed ozone is mainly depleted by photolysis (R 3) or in the reaction with an oxygen-radical (R 4). Under sunlight conditions, ozone and oxygen radicals are in a photochemical equilibrium based on R 2 and R 3. Hence, they can be comprised as the O_x-family ($O_x=O_3+O(^3P)+O(^1D)$).

$$O_2 + h\nu \;\rightarrow\; 2O(^3P) \tag{R1}$$
$$O(^3P) + O_2 + M \;\rightarrow\; O_3 + M \tag{R2}$$
$$O_3 + h\nu \;\rightarrow\; O_2 + O(^3P) \tag{R3}$$
$$O(^3P) + O_3 \;\rightarrow\; 2O_2 \tag{R4}$$
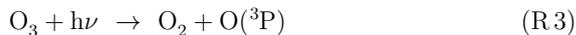
Further stratospheric species other than the O_x-family occur in a photochemical equilibrium as well and hence are comprised in families as the HO_x-(OH+H+HO_2), NO_x-(NO+NO_2+NO_3), ClO_x-(Cl+ClO+2×Cl_2O_2) or BrO_x-family (Br+BrO). Species of these families can catalyse the destruction of ozone in the reactions R5 and R6 (X=OH, NO, Cl, Br) (Bates and Nicolet, 1950; Crutzen, 1970).

$$XO + O(^3P) \;\rightarrow\; X + O_2 \tag{R5}$$
$$X + O_3 \;\rightarrow\; XO + O_2 \tag{R6}$$

$$\rule{8cm}{0.4pt}$$

$$O(^3P) + O_3 \;\rightarrow\; 2O_2 \tag{C1}$$

The contribution of these radical families to the total ozone destruction varies with the altitude (Portmann et al., 2012). In the lower stratosphere HO_x-radicals dominate ozone destruction and NO_x-radicals dominate ozone destruction in the middle stratosphere (see Fig. 2.3). The halogens (ClO_x- and BrO_x-family) contribute most to the stratospheric ozone destruction in the upper stratosphere (however, they do not dominate the ozone destruction, Fig. 2.3). Ozone formation in the Chapman-mechanism depends likewise on the altitude. This yields a maximum ozone-concentration in an altitude of 15–30 km, which is referred to as the ozone layer.
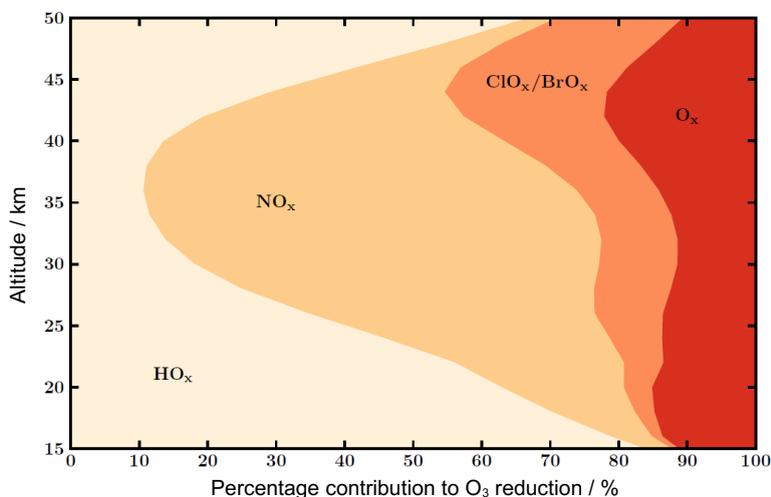
Figure 2.3: Contribution of single radical families to ozone destruction dependent on the altitude. Adapted from (Portmann et al., 2012).

2.3.1 Ozone chemistry in the lowermost stratosphere

In the lower stratosphere, ozone destruction driven by HO_x-radicals in the reactions

$$HO_2 + O_3 \rightarrow OH + 2\,O_2 \qquad (R\,7)$$
$$OH + O_3 \rightarrow HO_2 + O_2 \qquad (R\,8)$$

$$2\,O_3 \rightarrow 3\,O_2 \qquad (C2)$$

dominates the ozone loss processes. However, ozone smog formation known from the troposphere as the oxidation of CH_4 and CO (and other carbon species) in presence of NO_x-radicals can occur. Especially the "Ozone Smog Cycle" (C3), yielding the oxidation of CO to CO_2 with a simultaneous ozone formation (Haagen-Smit, 1952) is relevant in the lowermost stratosphere (Holton et al., 1995; Grenfell et al., 2006; Grooß et al., 2011). CO is oxidized to CO_2 by reacting with an OH-radical (R9). A second product of R9 is the hydrogen-radical H, which quickly reacts with oxygen forming an HO_2-radical (R10). The HO_2-radical reacts with NO forming an OH-radical and NO_2

(R 11). In the photolysis of NO_2, an $O(^3P)$-radical is formed R 12, which leads to ozone formation in reaction R 2.

$$OH + CO \rightarrow CO_2 + H \tag{R 9}$$
$$H + O_2 + M \rightarrow HO_2 + M \tag{R 10}$$
$$HO_2 + NO \rightarrow NO_2 + OH \tag{R 11}$$
$$NO_2 + h\nu \rightarrow NO + O(^3P) \tag{R 12}$$
$$O_2 + O(^3P) + M \rightarrow O_3 + M \tag{R 2}$$

$$CO + 2O_2 \rightarrow CO_2 + O_3 \tag{C3}$$
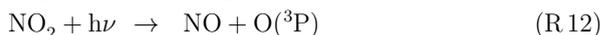
2.3.2 Polar ozone loss cycles

In late Antarctic winter and early spring, polar ozone is almost completely destroyed (e.g. Solomon et al., 2005; Grooß et al., 2011). The area of this ozone destruction is referred to as the *ozone hole* (Stolarski et al., 1986). The strong depletion of ozone in Antarctic spring was first reported by Farman et al. (1985) and is illustrated in Fig. 2.4 (bottom) through the average column ozone detected in October over Antarctic from 1980–2018. In the Antarctic spring, the average column ozone clearly decreases until the year 1987 and remains below the average of the years 1970–1982 (Fig. 2.4 bottom, red line) in the following years. Hence, after the first observation by Farman et al. (1985), the ozone hole can be observed every year in early polar spring (e.g. Jones and Shanklin, 1995; Müller et al., 2008). In the Arctic, this ozone loss occurs as well, but it is usually not as intense as in the southern hemisphere (see Fig. 2.4 top). However, in the winter 2019/2020 a very strong ozone destruction occurred (Witze, 2020; Dameris et al., 2020; Manney et al., 2020; Grooß and Müller, 2020).

In the ozone hole, ozone is almost completely destroyed due to the occurrence of chlorine catalysed ozone loss cycles, mainly the ClO-Dimer-Cycle (C4, Molina and Molina, 1987) and the ClO-BrO-cycle (C5, McElroy et al., 1986). In these cycles, ozone is destroyed in the reaction with Cl- and Br-radicals (R 16, R 18). In the ClO-dimer cycle (C4), ClO radicals formed in R 16 can react with each other forming the
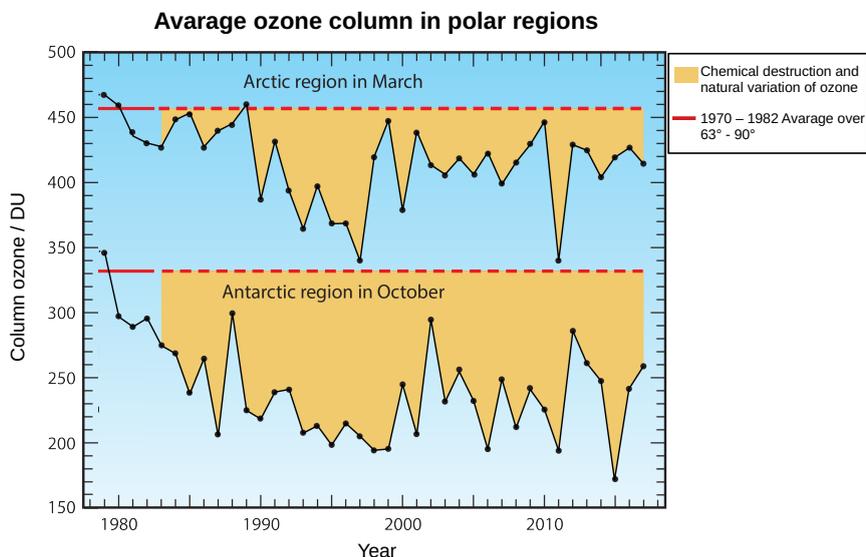
Figure 2.4: Average column ozone in the Arctic in March (top) and in the Antarctic in October (bottom) from 1980–2018. Adapted from Fig. Q11-1: Salawitch et al. (2019).

ClO-Dimer (R 13), which can be decomposed by photolysis back into Cl-radicals (R 14, R 15). Alternatively in cycle C5, ClO- and BrO-radicals formed in the reactions R 16 and R 18 can react with each other forming Cl- and Br-radicals (R 17), which again can attack stratospheric ozone molecules. These cycles drive the rapid ozone loss observed in Antarctic spring (e.g. Solomon, 1999).

$$ClO + ClO + M \rightarrow Cl_2O_2 + M \qquad\qquad (R\,13)$$
$$Cl_2O_2 + h\nu \rightarrow Cl + ClOO \qquad\qquad (R\,14)$$
$$ClOO + M \rightarrow Cl + O_2 + M \qquad\qquad (R\,15)$$
$$(Cl + O_3 \rightarrow ClO + O_2)\times 2 \qquad\qquad (R\,16)$$

$$2O_3 \rightarrow 3O_2 \qquad\qquad (C4)$$

$$ClO + BrO \rightarrow Cl + Br + O_2 \tag{R 17}$$
$$Cl + O_3 \rightarrow ClO + O_2 \tag{R 16}$$
$$Br + O_3 \rightarrow BrO + O_2 \tag{R 18}$$

$$2O_3 \rightarrow 3O_2 \tag{C5}$$
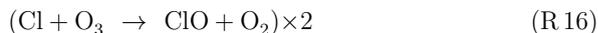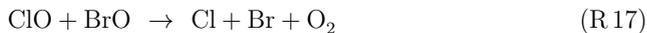
Additionally, Solomon et al. (1986) proposed that an ozone loss cycle (C6) based on ClO and HO_2 radicals could occur. However this cycle turned out to be of minor importance in the polar regions (Solomon, 1999). It is discussed that this cycle (C6) is relevant for ozone loss in the mid-latitude lower stratosphere (Daniel et al., 1999; Ward and Rowley, 2016).

$$ClO + HO_2 \rightarrow HOCl + O_2 \tag{R 19}$$
$$HOCl + h\nu \rightarrow OH + Cl \tag{R 20}$$
$$Cl + O_3 \rightarrow ClO + O_2 \tag{R 16}$$
$$OH + O_3 \rightarrow HO_2 + O_2 \tag{R 8}$$

$$2O_3 + h\nu \rightarrow 3O_2 \tag{C6}$$
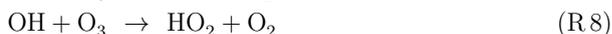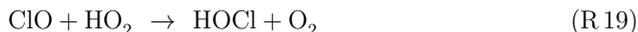
The strong ozone destruction in polar early spring is caused by high concentrations of stratospheric Cl_y (=ClO_x+HCl+$ClONO_2$). These concentrations are high due to industrial emissions of Chlorofluorocarbons (CFCs) and other halogen compounds since the middle of the 20th century. CFCs do not have a significant sink in the troposphere. Hence, they reach the stratosphere, where CFCs are decomposed and Cl-radicals are generated by photolysis. These chlorine radicals do attack stratospheric ozone.

The equivalent effective stratospheric chlorine (EESC) is a measure for the ozone depleting effect of all stratospheric halogen compounds. After the first observation of the ozone hole, the emission of CFC has been regulated by the Montreal Protocol (UNEP, 1987) and its amendments and adjustments. These amendments and adjustments were important for ultimately causing stratospheric halogen levels to decline (see Fig. 2.5). In our days, the stratospheric chlorine concentration is decreasing and the ozone layer
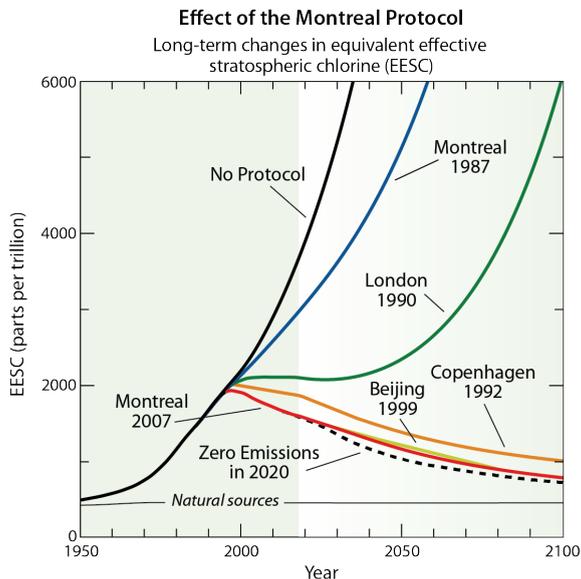
Figure 2.5: The effect of the Montreal protocol and its amendments and adjustments on the atmospheric chlorine abundance is illustrated through the equivalent stratospheric chlorine abundance from 1950–2010 (Fig. Q14-1 of Salawitch et al. (2019)).

begins to recover (Solomon et al., 2016a; WMO, 2018). However, chlorine levels are still enhanced in the stratosphere and it is expected that a complete recovery of the stratospheric ozone layer will take many decades (WMO, 2018).

Heterogeneous processes

Most of the stratospheric chlorine is bound in the reservoir gases HCl and $ClONO_2$. For the occurrence of the ozone loss cycles C4 – C6, activated chlorine ($=ClO_x$) is required. At low temperatures and in the presence of particles in the stratosphere, heterogeneous reactions (R 21–R 23) can convert the chlorine reservoir into Cl_2 and HOCl, which are decomposed in the presence of sunlight to form active ClO_x-radicals (e.g. Solomon, 1999).

$$\text{ClONO}_2 + \text{HCl} \xrightarrow{\text{het.}} \text{Cl}_2 + \text{HNO}_3 \qquad \text{(R\,21)}$$

$$\text{HCl} + \text{HOCl} \xrightarrow{\text{het.}} \text{Cl}_2 + \text{H}_2\text{O} \qquad \text{(R\,22)}$$

$$\text{ClONO}_2 + \text{H}_2\text{O} \xrightarrow{\text{het.}} \text{HOCl} + \text{HNO}_3 \qquad \text{(R\,23)}$$
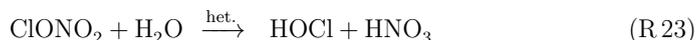
Heterogeneous processes can occur in the bulk and at the surface of ice particles, Nitric Acid Trihydrate (NAT) and liquid binary ($\text{H}_2\text{SO}_4/\text{H}_2\text{O}$) and ternary ($\text{H}_2\text{SO}_4/\text{HNO}_3/\text{H}_2\text{O}$) solutions. For heterogeneous chlorine activation on liquid particles to occur, Drdla and Müller (2012) showed that the temperature has to fall below a threshold temperature in polar regions, which depends on the water vapour content, the sulfate aerosol surface area density and the pressure (altitude).

At the very dry conditions in the polar stratosphere, very low temperatures (below 195 K) are required for heterogeneous chlorine activation through reactions R 21–R 23 (Solomon, 1999; Shi et al., 2001). An enhancement of sulfate leads to a swelling of liquid particles (Drdla and Müller, 2012; Solomon, 1999) and thus enhances the likelihood that chlorine activation takes place on a particle. Furthermore, an enhancement of water vapour above background values would allow chlorine activation to occur at higher temperatures (200–205 K) (Drdla and Müller, 2012). An increase of water vapour leads to a higher water activity in the particle and hence the solubility of HCl and ClONO_2 increases. Since the uptake of ClONO_2 usually limits heterogeneous chlorine activation in R 21 and R 23, the probability for the occurrence of the reactions R 21 and R 23 (Shi et al., 2001) increases with higher water vapour mixing ratios.

Chlorine activation and deactivation

At the time when the chlorine activation transforms chlorine reservoir species into active ClO_x, in parallel chlorine deactivation processes convert ClO_x into HCl and ClONO_2. The most relevant reactions for chlorine deactivation in the Antarctic winter are

$$CH_4 + Cl \rightarrow HCl + CH_3 \qquad\qquad (R\,24)$$
$$\text{and } HCHO + Cl \rightarrow HCl + HCO \qquad\qquad (R\,25)$$
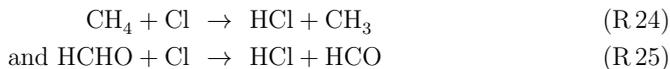
(e.g. Müller et al., 2018). In polar winter, increasing chlorine activation rates (R 21 – R 23) cause higher Cl mixing ratios and thus leads to an accelerated chlorine deactivation (R 24, R 25). Net chlorine activation occurs, as soon as the rates of the heterogeneous chlorine activation reactions R 21 – R 23 exceed the rates of chlorine deactivation in reaction R 24 and R 25 (Crutzen et al., 1992; Grooß et al., 2011; Robrecht, 2016).

Net chlorine activation results in an increase in the ClO_x concentration. Chlorine is commonly defined to be activated, if the ClO_x mixing ratio accounts to at least 10% of total Cl_y (Drdla and Müller, 2012). After the chlorine activation step, chlorine activation and chlorine deactivation rates balance each other. This maintains activated chlorine and thus enables the catalytic ozone loss cycles C4 – C6 to proceed (Crutzen et al., 1992; Grooß et al., 2011; Robrecht, 2016; Müller et al., 2018; Zafar et al., 2018). Once chlorine deactivation rates (R 24, R 25) exceed the chlorine activation rates (R 21 – R 23), the balance between chlorine activation and deactivation breaks. Activated chlorine is not longer maintained and the catalytic ozone loss cycles stop. This imbalance can be based on an increase in temperatures, which results in a reduction of heterogeneous reaction rates, or on very low ozone mixing ratios, which increase the Cl/ClO-ratio and thus favour chlorine deactivation in reaction R 24 and R 25 (Grooß et al., 2011).

Chlorine activation in mid and low latitudes

The combination of temperatures, water vapour and the aerosol abundance determines whether the heterogeneous reactions R 21 – R 23 occur in the atmosphere. Hence, chlorine activation does not necessarily need to occur only in polar winter. Solomon et al. (2016b) and von Hobe et al. (2011) observed enhanced ClO mixing ratios in combination with the occurrence of cirrus clouds in the tropical upper troposphere and lower stratosphere. Borrmann et al. (1996, 1997) found an influence of cirrus clouds on ozone chemistry as well.

In the mid-latitude tropopause region, an enhancement of chlorine radicals was reported with respect to elevated amounts of aerosol particles (Keim et al., 1996; Berthet et al., 2007). Anderson et al. (2012, 2017) proposed that an enhancement of water vapour in the mid-latitude lowermost stratosphere due to convective overshooting events in combination with low temperatures may lead to heterogeneous chlorine activation and thus the occurrence of catalytic ozone loss cycles (e.g. ClO-Dimer-cycle C4 and ClO-BrO-cycle C5) known from the polar regions. Further, Clapp and Anderson (2019) assumed a removal of stratospheric nitric acid to occur after convective overshooting events through an uptake of HNO_3 into aerosol particles and subsequent sedimentation. This may also effect chlorine catalysed ozone chemistry in the lowermost stratosphere. Because temperatures, water vapour and the aerosol abundance determine the conditions yielding chlorine activation, Anderson et al. (2012) concluded that the likelihood for this ozone loss process to occur may increase in the future as well. Thereby both a climate change scenario and a scenario assuming the additional application of sulfate geoengineering are of interest for the potential occurrence of this ozone loss process. In this thesis, the aim is to investigate how much water vapour has to be enhanced for chlorine activation to occur for a variety of conditions and to deduce the likelihood for ozone destruction to occur in the mid-latitude lowermost stratosphere caused by heterogeneous chlorine activation.

2.4 Climate change and sulfate geoengineering

Strong emissions of greenhouse gases (GHG) by the human population lead to global warming, which drives climate change accompanied by sea level rise, melting of glaciers and an increase in extreme weather events such as droughts and floodings (e.g. IPCC, 2014). The emission of GHG affects the radiation energy balance of the Earth. Therefore, a recently discussed concept to overcome global warming is the injection of sulfate particles into the stratosphere, which would influence the energy balance of the Earth. Such an injection of sulfate particles is discussed as a way to moderate negative effects of GHG on the global temperatures. For understanding the concept of sulfate
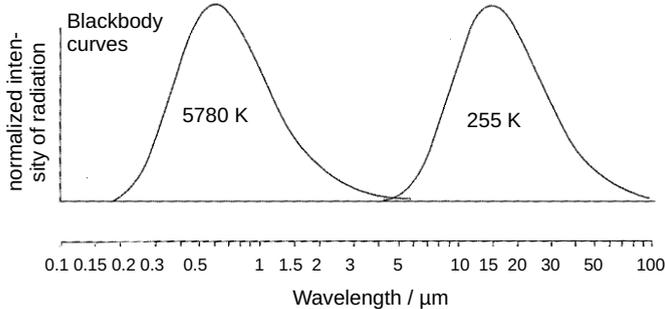
Figure 2.6: Outline of the blackbody wavelength distribution of the sun (left) and the Earth (right). Adapted from Wallace and Hobbs (2006).

geoengineering, background knowledge about the energy balance of the Earth is necessary. Hence, in this section first, the energy balance of the Earth is introduced before explaining the idea of sulfate geoengineering and describing the impact of both climate change and sulfate geoengineering on stratospheric chemistry and dynamics.

2.4.1 Energy balance of the Earth

The sun emits radiation in the whole electromagnetic spectrum and can be characterized as a blackbody with a surface temperature of ∼5780 K (Seinfeld and Pandis, 2006). A black body emits light not uniformly for all wavelength, but exhibits one wavelength of peak emission, where the intensity of emitted light is highest. The higher the temperature of a blackbody the lower is the wavelength of peak emission and the more energy a blackbody emits. An outline of the blackbody emission spectrum of the sun is schematically shown in Fig. 2.6 (left peak). The sun mainly emits in the UV/vis spectrum and its λ_{max} is ∼480 nm (e.g. Seinfeld and Pandis, 2006; Visconti, 2001; Wallace and Hobbs, 2006).

A part of the energy emitted by the sun reaches the Earth. The incoming and outgoing radiation energy of the Earth is schematically illustrated in Fig. 2.7. The incoming solar radiation refers to the width of the yellow arrows. A part of the incoming solar radiation is reflected at the surface of the Earth or by clouds and aerosol particles. The
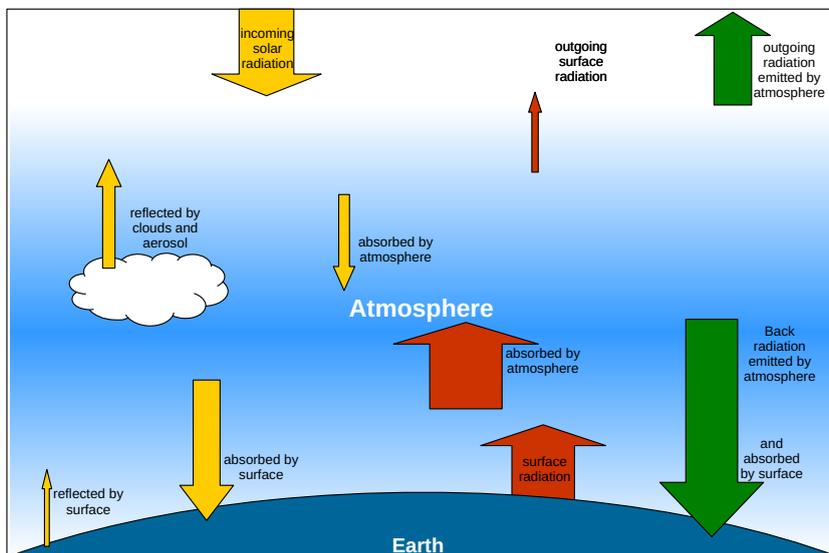
Figure 2.7: Illustration of the Earth radiation budget. Yellow arrows illustrate incoming solar radiation, red arrows radiation emitted by the surface of the Earth and green arrows the radiation emitted by the atmosphere. The thickness of the arrows illustrates the amount of energy absorbed, emitted or reflected in that specific case. Adapted from Seinfeld and Pandis (2006).

other part of the solar radiation is absorbed either by the surface of the Earth or by the atmosphere (Seinfeld and Pandis, 2006). The fraction of reflected light is described by the Earth's albedo. The higher the albedo, the more radiation is reflected and is not absorbed.

Absorption of radiation causes a warming of the Earth. Hence the Earth itself can be considered as a blackbody and emits radiation (red arrows in Fig. 2.7). Since the blackbody temperature of the Earth is around $255\,\mathrm{K}$, it emits in the infrared (IR) spectrum with a peak emission at a wavelength of $\sim 11\,\mu\mathrm{m}$. Thus, the emission spectrum of the Earth is shifted in comparison with the sun spectrum (illustrated in Fig. 2.6; Wallace and Hobbs, 2006).

Without an atmosphere, the entire radiation emitted by the Earth would be radiated

to the space. Since the Earth atmosphere is a good IR-absorber, the radiation emitted by the Earth is mainly absorbed by the atmosphere. The atmosphere itself warms and emits radiation both upwards to the space and downwards to the Earth (Fig. 2.7, green arrows) (Seinfeld and Pandis, 2006). At the surface of the Earth, the energy emitted by the atmosphere is absorbed causing a further warming. Finally a radiative equilibrium is reached and the energy absorbed by the Earth is equal to the emitted energy (Seinfeld and Pandis, 2006; Visconti, 2001; Wallace and Hobbs, 2006).

However, if more energy is absorbed by the Earth than emitted, the surface of the Earth warms due to radiative forcing. Absorbing radiation in the IR, the continuous anthropogenic emission of GHG – such as CO_2, CH_4, N_2O – causes a warming of the atmosphere and the surface (Stocker et al., 2013).

2.4.2   Concept of sulfate geoengineering

With the aim to reduce some of the negative consequences of global warming, the idea of sulfate geoengineering was discussed by Crutzen (2006). The concept of sulfate geoengineering is to cool the surface of the Earth temperature by reducing the solar radiation energy which reaches the surface of the Earth. The injection of sulfur particles into the stratosphere would increase the fraction of sun light scattered back into the space. This idea is based on the effect strong volcanic eruptions have on the Earth's temperature. Releasing high amounts of SO_2 which cause the formation of sulfate aerosol particles, strong volcanic eruptions increase the Earth albedo and can cool the global surface temperature. As an example, the strongest volcanic eruption of the last century is the eruption of Mt. Pinatubo in 1991, which reduced the global mean temperature by $0.5\,K$ in the year following the eruption 1992 (McCormick et al., 1995; Dutton and Christy, 1992).

Sulfur dioxide (SO_2) released into the atmosphere through volcanic eruptions is oxidized to SO_3 in the reaction with the hydroxy radical (OH) and the subsequent reaction with oxygen.

$$SO_2 + OH + M \;\rightarrow\; HOSO_2 + M \qquad\qquad (R\,26)$$
$$HOSO_2 + O_2 \;\rightarrow\; HO_2 + SO_3 \qquad\qquad (R\,27)$$
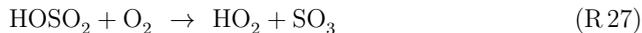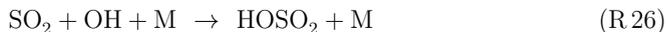
In the presence of water vapour, SO_3 reacts to H_2SO_4.

$$SO_3 + H_2O + M \;\rightarrow\; H_2SO_4 + M \qquad\qquad (R\,28)$$

Subsequently, sulfate aerosol particles consisting of binary H_2O/H_2SO_4 form by co-condensation of H_2O and H_2SO_4 (Seinfeld and Pandis, 2006).

Aerosol particles reduce the surface temperature of the Earth, because they reflect sunlight back into space. However, the sulphate particles also absorb infrared radiation and thus locally warm the atmosphere. How large the cooling effect of sulfate particles released for geoengineering is, mainly depends on three factors: the lifetime of the aerosol in the atmosphere, the fraction of light scattered back into space and the amount of absorbed radiation energy (e.g. Pitari et al., 2014; Niemeier and Timmreck, 2015). Larger particles sediment faster and thus have a shorter lifetime than smaller particles. Additionally large sulfate particles reflect light less efficiently and have a larger warming effect due to absorption of infrared radiation. Thus, smaller particles are expected to have a higher cooling efficiency than large particles (Lacis et al., 1992; Rasch et al., 2008; Tilmes et al., 2009; Pitari et al., 2014; Niemeier and Timmreck, 2015).

The lifetime of sulfate aerosols in the troposphere accounts to around one week. Since the lifetime in the stratosphere is 1–2 years, sulfate particles should be injected into the stratosphere to gain an efficient cooling effect from geoengineering. As an option to transport SO_2 into the stratosphere, Crutzen (2006) proposed for example to launch balloons carrying burning sulfur or H_2S into the stratosphere. Combustion of S_2 or H_2S would form SO_2. Crutzen (2006) estimates the costs of sulfate geoengineering between 25 and 50 billion US-\$ per year, depending on the required amount of SO_2. To justify the application of sulfate geoengineering, this costs must be compared to the environmental and social benefits gained. However, not only the possible benefits

gained from sulfate geoengineering have to be taken into account before the application but also possible risks through the occurrence of unintended side effects.

2.4.3   Impact of global warming on the stratosphere

Greenhouse gases released into the atmosphere lead to a warming of the troposphere. How much the troposphere warms depends amongst others on the emitted GHG amount. There are different representative concentration pathways (RCP) used in science to describe different scenarios of global warming by the year 2100. For example, the RCP2.6 scenario assumes a low GHG emission resulting in a relatively low global warming, which stays constant after the year 2100. In contrast the RCP8.5 scenario assumes a worst case scenario with high GHG emissions and thus a large increase of the global mean temperature, which continues to increase after 2100. However, the RCP scenarios assume only few options for possible pathways (Pachauri et al., 2014). The effect GHG have on the stratospheric temperatures depends on the balance between absorbed and emitted infrared radiation. Radiation absorbed by a GHG causes a warming. In contrast in the stratosphere radiation emitted by a GHG goes into space and thus cools the stratosphere. For stratospheric CO_2, the emission of radiation has a larger effect than the absorption resulting a cooling effect throughout the stratosphere. For stratospheric CH_4 and N_2O, emission and absorption are balanced in the lower stratosphere, but in the upper stratosphere the cooling effect dominates. Hence, in the stratosphere GHG generally lead to a cooling (e.g. Ramaswamy et al., 2001; Oman et al., 2010).

Global warming will lead to more water vapour in the troposphere, because increasing tropospheric temperatures will cause more evaporation and less condensation of water (Lacis et al., 2010). Also stratospheric water vapour increases because of a warming of the tropical tropopause layer, where the tropopause temperature determines how much water vapour enters the stratosphere. This enhances especially water vapour in the lowermost stratosphere (e.g. Dessler et al., 2013; Revell et al., 2016).

Absorbing infrared radiation, atmospheric water vapour is an important GHG and forces the global warming. Hence, there is a feedback between global warming, which

enhances atmospheric water vapour, and increasing atmospheric water vapour, which forces global warming (Dessler and Sherwood, 2009; Lacis et al., 2010). Stratospheric water vapour contributes likewise to this feedback (Dessler et al., 2013).

As greenhouse gases increase in the atmosphere, models predict that more water may be convectively transported into the stratosphere (Trapp et al., 2009; Van Klooster and Roebber, 2009). Besides water vapour penetrating the stratosphere, methane oxidation is an additional relevant source for stratospheric water vapour. Increasing tropospheric methane results in more methane to be transported in the stratosphere. However, Revell et al. (2016) found that increasing tropopause temperatures enhance stratospheric water vapour more than higher stratospheric methane concentrations.

The stratospheric ozone concentrations will change as well because of climate change. Global warming will affect mixing patterns in the stratosphere and is expected to overall accelerate the BDC. This yields a decline in tropical ozone and an increase in the extra-tropics (e.g. Rind et al., 1990; Butchart, 2014; Ploeger et al., 2015b; WMO, 2018), because more ozone is transported polewards from the tropics. In contrast, Fu et al. (2019) found a deceleration of the annual mean BDC from the years 2000–2018. This deceleration is likely related to the healing of the ozone hole (Solomon et al., 2016a) in the southern hemisphere through reduced stratospheric Cl_y mixing ratios.

Multiple changes in ozone chemistry are expected to occur in future: A reduction of ozone depleting substances (ODS) due to the Montreal protocol and its amendments and adjustments will reduce halogen driven catalytic ozone destruction (WMO, 2018). Lower stratospheric temperatures decelerate gas phase ozone destruction cycles. Increasing CO and CH_4 may yield more ozone formation in ozone smog cycles (e.g. cycle C3). Increasing N_2O may increase NO_x driven ozone destruction in the middle and upper stratosphere (Ravishankara et al., 2009; Portmann et al., 2012). The enhancement of water vapour leads to higher HO_x-concentrations potentially resulting in more HNO_3 formation and thus a reduction of the NO_x-cycle in the middle and upper stratosphere. Furthermore, enhanced HO_x concentrations could increase the gas-phase chlorine activation (HCl+OH) and thus push ozone loss due to the ClO_x-cycle in the

upper stratosphere (Evans et al., 1998; Shindell, 2001; Randeniya et al., 2002; Stenke and Grewe, 2005; Iglesias-Suarez et al., 2016). Overall, the decline in ODS and slowlier ozone destruction cycles due to lower temperatures dominate future stratospheric ozone chemistry, leading to an overall increase in stratospheric ozone (Fels et al., 1980; Iglesias-Suarez et al., 2016).

In the lowermost stratosphere, especially an increase in ozone formation due to methane and CO oxidation (e.g. in cycle C3) as well as an increase in catalytic ozone destruction based on HO_x radicals (cycle C2) will affect ozone chemistry. Anyway, lowermost stratospheric ozone is expected to increase dominated by the acceleration of the BDC (Oman et al., 2010; Reader et al., 2013; Iglesias-Suarez et al., 2016).

Concluding, a climate change is expected to cool the stratosphere, warm the tropopause and hence allow more water vapour to enter the stratosphere. Upper stratospheric ozone is expected to increase based on reduced ODS and decelerated ozone destruction cycles in combination with lower temperatures. The acceleration of the BDC is expected to result in an increase in extratropical ozone and more ozone transported into the lowermost stratosphere.

2.4.4 Impact of geoengineering on the stratosphere

Global warming will affect the stratospheric composition, chemistry and dynamics, but the application of sulfate geoengineering would likewise lead to changes in the stratosphere. The effectiveness and the simulated impact of geoengineering on stratospheric chemistry and dynamics depend on various parameters as the injection altitude, its location or the model setup (Pitari et al., 2014; Richter et al., 2017; Tilmes et al., 2018). However, some consistent trends were found in a variety of studies.

Since the idea of sulfate geoengineering is based on the impact of volcanic eruptions on tropospheric temperatures, observations made after volcanic eruptions indicate a potential impact of sulfate geoengineering on the stratosphere. Pitari et al. (1993) reported a local stratospheric warming in the volcanic plume due to the absorption of radiation by sulfate particles. Few month after the eruption of Mt. Pinatubo, a warming of the tropical lower stratosphere was noticed (Labitzke and McCormick, 1992;

Young et al., 1994) and a decrease of the ozone column was observed (Grant et al., 1992; Schoeberl et al., 1993; Telford et al., 2009). Such a long term decline of column ozone could likewise be observed after less strong volcanic eruptions (e.g. Andersson et al., 2013; Jing et al., 2020).

A stratospheric warming and a warming of the tropical tropopause layer is expected as well, if sulfate geoengineering is applied (Pitari et al., 2014; Visioni et al., 2017a). Due to the cooling of the troposphere and the warming of the stratosphere the exchange between troposphere and stratosphere in the mid-latitudes would be reduced (Visioni et al., 2017b). A warming of the tropical tropopause layer would lead to a stratospheric moistening (Dessler et al., 1995; Visioni et al., 2017a) and would affect the BDC. The upwelling in the upper branch of the BDC would be enhanced, the transport within the lower branch of the BDC reduced (Pitari et al., 2014; Visioni et al., 2017b) and the downwelling of the BDC from the stratosphere to the troposphere accelerated (Visioni et al., 2017b).

The chemical impact of sulfate geoengineering on stratospheric ozone is mainly based on an enhancement of heterogeneous chemical reactions. In polar regions, increasing aerosol concentrations will enhance heterogeneous reactions and thus yield more activated chlorine radicals. This may delay the recovery of the ozone hole by 30–70 years (Tilmes et al., 2008, 2012).

In the middle stratosphere, the main impact is the shift of NO_x into NO_y due to the occurrence of the heterogeneous reaction

$$N_2O_5 + H_2O \ \rightarrow \ 2HNO_3 \cdot \tag{R 29}$$

This shift decreases the ozone destruction in the NO_x-cycle (C1, X=NO) but at the same time, NO_x reduction increases ozone destruction due to ClO_x, BrO_x and HO_x radicals (Heckendorn et al., 2009; Tilmes et al., 2009, 2018; Pitari et al., 2014). Pitari et al. (2014) found, that the reduction of the NO_x-cycle is balanced by the increase in catalytic ozone destruction through ClO_x-radicals until the mid of the 21st century. After the year 2050, they reported an increase of ozone due to the decline of stratospheric Cl_y.

In the lowermost stratosphere, increasing ozone concentrations in the middle stratosphere may reduce the UV-intensity and thus reduce the ozone formation trough the Chapman mechanism (see Sec. 2.3) in this altitude. Furthermore an increase of water vapour will release more HO_x radicals, which dominate catalytic ozone destruction (cycle C2) in the lowermost stratosphere (Heckendorn et al., 2009).

How sulfate aerosols in the lowermost stratosphere affect the chemistry could be observed after volcanic eruptions. As an example, the aerosol surface area density in the lower stratosphere ranges between 0.5 and $1.5\,\mu m^2\cdot cm^{-3}$ under non-volcanic conditions (Thomason and Peter, 2006), while the perturbation of Mt. Pinatubo yielded peak values of more than $40\,\mu m^2\cdot cm^{-3}$ (Thomason et al., 1997). Prather (1992) noticed that an increase in the aerosol surface area by volcanic eruptions first would reduce gas phase NO_x mixing ratios before a fast chlorine-catalyzed ozone destruction can occur. The study of Webster et al. (1998) focused on the heterogeneous chlorine activation step and found that the impact of volcanic sulfate aerosols on stratospheric HCl depends on the temperature as well. In the mid-latitude tropopause region, Keim et al. (1996) and (Thornton et al., 2007) observed enhanced ClO and reduced NO concentrations in combination with enhanced water vapour and aerosol abundance. These observations were discussed in respect to heterogeneous reactions as R 21 and R 23.

Heterogeneous chlorine activation causing catalytic ozone destruction processes similar to those known from polar late winter and early spring was proposed by Anderson et al. (2012) to potentially occur in the lowermost stratosphere in combination with sulfate geoengineering, but also with enhanced water vapour. However, the detailed mechanism of this ozone loss process and the likelihood that this ozone loss process will occur today or in future yet needs to be investigated in detail. Therefore, the focus of this thesis is on the detailed analysis of the mechanism and its sensitivities on a variety of conditions as well as the likelihood for this ozone loss process to occur and its impact on ozone in the lowermost stratosphere. For investigating these subjects, box-model simulations are performed and simulations of a global model are used.

Chapter 3

Numerical models

For investigating the chemical mechanism of heterogeneous chlorine activation causing ozone destruction and its likelihood to occur in mid-latitudes, box-model simulations are performed with the Chemical Lagrangian Model of the Stratosphere (CLaMS). The likelihood that ozone loss occurs is determined for conditions today and in future combining CLaMS box-model simulations with results of the Geoengineering Large Ensemble Simulations (GLENS), which were performed with a global Earth System Model (ESM).

In this chapter, Lagrangian box-models as well as more complex models with higher dimensions are introduced for better understanding of the CLaMS and GLENS simulations used in this thesis. Further, an overview on the CLaMS box-model and GLENS is given. The setup for the conducted CLaMS simulations as well as the selection of GLENS results is described later in this thesis, when the specific studies are introduced (see Sec. 4.1 and Sec. 5.1).

3.1 Introduction to numerical atmospheric models

The atmosphere is a complex system coupling various chemical and dynamical processes. While measurements provide important information about the current state of the atmosphere, atmospheric models provide the framework to study details of single processes and to link them to the whole atmospheric system. Thus, atmospheric models

implemented based on knowledge gained from measurements allow the interaction of various atmospheric processes to be analysed. Based on the current state of knowledge, models can likewise be used to predict and to interfere uncertainties of the future development of the atmosphere.

The simplest type of an atmospheric model is a box-model, which simulates the chemical composition of a single air parcel. Box-models are very well suited to study detailed chemical or microphysical processes. Describing the air parcel as a well mixed box, trace gas concentrations and external parameters (such as the temperature, the pressure and the solar zenith angle) are assumed to be everywhere same within that box. Accordingly, box models are zero dimensional and changes of trace gas concentrations and external parameters only depend on time. The composition of an air parcel varies due to chemical formation and decomposition as well as the emission, deposition and transport of trace gases.

Chemical reaction kinetics can be described through a set of differential equations. Since in the atmosphere chemical reactions and processes differ in reaction order and require very different time scales, stiff differential equations have to be solved numerically to calculate the time dependent composition of the air parcel. Atmospheric chemistry mainly depends on the pressure, the temperature and the solar zenith angle. These are input parameters for the chemical model. In a Lagrangian box-model, the single air parcel is transported with the wind along a trajectory, which describes the time dependence of temperature, pressure and location of that air parcel (e.g. Wallace and Hobbs, 2006; Seinfeld and Pandis, 2006).

For describing the global distribution of trace gases and their behaviour accurately, more dimensional models are necessary. The more chemical, physical and dynamical processes are included within the simulations the more complex is the model. A three dimensional model provides the atmospheric composition dependent on the longitude, latitude and altitude. Therefore air parcels are arranged and computed in three dimensional space. The resolution of the three dimensional model is determined by the horizontal and vertical distance between single computing points (which are single air parcels in a Lagrangian 3-dimensional model) .

For describing atmospheric dynamics, winds and temperatures have to be considered. If these parameters are taken from external meteorological fields (e.g. provided by the European Centre for Medium-Range Weather Forecasts (ECMWF)), the model type is referred to as a *Chemistry Transport Model*. In contrast, in a *Chemistry Climate Model* both atmospheric chemistry and meteorology are calculated in the same model. If the atmospheric model is coupled with models simulating further components of the Earth system as the ocean, the surface or the biosphere, the model is referred to as an *Earth System Model*.

Box-models and higher dimensional models have different strengths and applications. Since box-models need less computing time than higher dimensional models, they are a useful tool for detailed analyses of processes, e.g. chemical mechanisms, which often have to be simplified in higher dimensional models. However, atmospheric dynamics and global trace gas distributions are only reasonably described in three-dimensional models.

3.2 Chemical Lagrangian Model of the Stratosphere

The CLaMS is a Lagrangian chemical transport model described by McKenna et al. (2002a,b) and extended for the application in three dimensions by Konopka et al. (2004). CLaMS is structured in four main modules: a trajectory module to calculate the movement of an air parcel, a chemistry module for simulating chemical processes, a mixing module enabling mixing between air parcels and a sedimentation module, which considers the sedimentation of aerosols. For the box-model simulations conducted in this thesis, the trajectory and the chemistry module are used. Thus, the CLaMS simulations performed in this thesis neglect mixing between neighbouring air parcels.

Trajectory module

In the trajectory module, the movement of air parcels is calculated assuming a diabatic transport, which allows air parcels to cross isentropes and thus move vertically. Determining a location prior to the simulation, forward and backward trajectories are

calculated based on temperatures and winds from meteorological fields (Swinbank and
O'Neill, 1994; McKenna et al., 2002b; Konopka et al., 2004). Vertical velocities are
deduced from the total diabatic heating rates, which comprise heating through radiation
as well as release of latent, and sensible heat (e.g. latent heating in clouds due to
condensation or freezing; Ploeger et al., 2010). In this thesis, realistic trajectories are
calculated based on total diabatic heating rates as well as winds and temperatures
derived from ERA-Interim data (Dee et al., 2011). ERA-Interim is a global atmospheric
reanalysis for the time span 01.01.1979 – 31.08.2019 provided by the ECMWF.

Chemistry module

Stratospheric chemistry in CLaMS is simulated along a trajectory considering bi- and
termolecular gas phase reactions as well as heterogeneous reactions and photolysis
(McKenna et al., 2002a; Grooß et al., 2014, 2018). In total 42 species and 131 chemical
reactions are considered (see Appendix A). The mixing ratio of all chemical species has
to be initialized before the box-model simulations can be started. Chemical reaction
kinetics are taken from Sander et al. (2011) and to determine photolysis rates, a spherical
geometry of the molecules is assumed (Meier et al., 1982; Becker et al., 2000) in CLaMS.
Heterogeneous reaction rates for R 21–R 23 are calculated based on the study of Shi
et al. (2001) for liquid particles. To solve the stiff differential equations, which describe
chemical reaction kinetics, the ASAD (A Self-contained Atmospheric chemistry coDe)
code (Carver et al., 1997) with the SVODE-solver (Brown et al., 1989) is used in the
version of CLaMS employed here.

Generally in CLaMS, heterogeneous reactions on liquid binary and ternary solutions,
ice and NAT (Nitric Acid Trihydrate) particles are considered (e.g. Grooß et al., 2014,
2018). However, for this thesis heterogeneous reactions are only considered in and at the
surface of liquid particles. For heterogeneous particle formation, the initial liquid aerosol
number density (N_0), the standard deviation of the logarithmic normal distribution of
the particle size (σ), and the gas phase equivalent of the amount of sulfuric acid in the
aerosol are set prior to the simulation. The gas phase equivalent is used to calculate

the density of liquid particles as described in the study of Shi et al. (2001) for binary solutions and of Luo et al. (1996) for ternary solutions. Based on the density of liquid particles, the aerosol number density and the standard deviation of the particle size, the surface area density of aerosol particles is calculated. For being independent of the size of the simulated air parcels, the surface aerosol density is used instead of just the surface area.

With the chemistry module, stratospheric chemistry can be simulated along artificial and realistic trajectories. Chemistry can be initialized based on measurements (e.g. from aircraft, balloon, satellite) or on results of global model simulations.

3.3 Geoengineering Large Ensemble Simulations

The GLENS simulations were performed with an Earth System Model on a global scale to provide a comprehensive data set for studying the limitations, side-effects and risks of sulfate geoengineering (Tilmes et al., 2018). Two scenarios are simulated in GLENS: a climate change scenario following the RCP8.5 assumption and a geoengineering scenario additionally injecting SO_2 into the stratosphere. The GLENS project includes three ensemble members from the year 2010 to the end of the 21st century following the RCP8.5 scenario and twenty ensemble members of the geoengineering scenario comprising the years 2020–2099 (Tilmes et al., 2018).

The simulations were performed with version 1 of the Community Earth Sytem Model (CESM1, Hurrell et al., 2013). In the GLENS simulations, the Whole Atmosphere Community Climate Model (WACCM, Marsh et al., 2013) is used as the atmospheric component. The resolution in determined through a $0.9° \times 1.25°$ (latitude $\times$ logitude) grid further comprising 70 vertical layers from the ground up to a pressure of 10^{-6} hPa. WACCM is coupled to land, sea ice and the ocean models and includes fully interactive middle atmosphere chemistry, simplified chemistry in the troposphere as well as sulfate bearing gases, which are important for the formation of stratospheric sulfate (Mills et al., 2017). The 3-mode version of the model aerosol module (MAM3, Mills et al., 2016) was used to properly represent aerosol microphysics and the sulfate aerosol formation from injected SO_2.

The ability of the model (CESM1 with WACCM) to properly represent both atmospheric chemistry and dynamics as well as the atmospheric response on a strong stratospheric SO_2 injection was proven by Mills et al. (2017). A comparison of observations with four free running simulations for the years 1975–2016 initialized with conditions from 1 January 1975 showed a good agreement regarding temperatures, atmospheric dynamics, stratospheric water vapour and ozone. Simulations of the Mt. Pinatubo's eruption 1991 were in agreement with the observed aerosol optical depth. Especially the radiative impacts (namely the absorbed solar radiation and the outgoing long wave radiation) were matching the observations very well, which is important to properly simulate the effect of sulfate geoengineering on stratospheric chemistry and dynamics.

The geoengineering scenario of GLENS is based on the RCP8.5 scenario, but aims to hold the global mean temperature, the inter-hemispheric temperature gradient and the equator-to-pole gradient at the level of the year 2020 by applying geoengineering (Kravitz et al., 2017)). To reach the temperature targets, SO_2 is simultaneously injected into the stratosphere at four injection locations beginning from the year 2020. These locations are at 15°N and 15°S at an altitude of 25 km and at 30°N and 30°S at an altitude of 22.8 km. These injection altitudes lay around 5 km above the tropopause. Tilmes et al. (2018) reported that SO_2 injections in these altitudes cool more efficient than in lower altitudes and non-equatorial injections are better transported to middle and higher latitudes than equatorial injections. However, injections at 50° North and South are removed quickly from the stratosphere by the downwelling branch of the BDC. MacMartin et al. (2017) found that injecting at different locations enables a variety of global aerosol distributions. They proposed that this gained flexibility could be used to reach not only a temperature target for the global mean temperature but also for the inter-hemispheric temperature gradient and the equator-to-pole gradient (which the GLENS project is aiming for). The injection amount at each location is determined using a feedback algorithm that annually adjusts the location rates (MacMartin et al., 2014; Kravitz et al., 2016, 2017). To reach the temperature targets, more than $50\,\mathrm{Tg\,a^{-1}}$ SO_2 would have to be emitted at the end of the 21st century. This is five times as much as the emitted amount by the Mt. Pinatubo eruption in the year 1991 (Tilmes et al., 2018).

Chapter 4

Chlorine activation and ozone loss in the mid-latitude lowermost stratosphere

Heterogeneous chlorine activation causing ozone loss in the mid-latitude lowermost stratosphere was discussed in previous studies to potentially occur in combination with convective overshooting events, stratospheric cooling due to a climate change or the application of sulfate geoengineering which leads to an enhancement of liquid sulfate aerosols (Anderson et al., 2012, 2017; Ravishankara, 2012; Schwartz et al., 2013; Clapp and Anderson, 2019). In this chapter of the thesis, the ozone loss mechanism and its sensitivity to various stratospheric conditions is analysed in detail. Therefore, a box-model study with CLaMS is conducted based on measurements of the Studies of Emissions and Atmospheric Composition, Clouds and Climate Coupling by Regional Surveys (SEAC[4]RS) aircraft campaign (further described in Sec. 4.1.1).

First, the model setup is described in Section 4.1 including a brief overview on the used measurements of the SEAC[4]RS aircraft campaign, a description of the selected standard trajectory for further analysis and the chemical initialization. In Sec. 4.2, the chlorine activation step, catalytic ozone loss cycles and the maintenance of activated chlorine levels in the mid-latitude stratosphere are investigated in detail. The sensitivity of the mechanism to water vapour, sulfate content, temperature, Cl_y mixing ratio and reactive

nitrogen (NO_y) is explored in Sec. 4.3. Case studies, which extend the simulated time period, assume conditions based on SEAC^{4}RS measurements, investigate the sensitivity to inorganic bromine (Br_y) and an extreme case assuming conditions used in the study of Anderson et al. (2012), further demonstrate these sensitivities in Sec. 4.4.

The main results of this chapter are published in the journal of atmospheric chemistry and physics:

Robrecht, S., Vogel, B. Grooß, J.-U., Rosenlof, K., Thornberry, T., Rollins, A., Krämer, M., Christensen, L. and Müller, R.: Mechanism of ozone loss under enhanced water vapour conditions in the mid-latitude lower stratosphere in summer, Atmos. Chem. Phys., 19, 5805–5833, doi:10.5194/acp-19-5805-2019, 2019

and the presentation in this chapter closely follows this publication.

4.1 Model setup

CLaMS box-model simulations (see Sec. 3.2) described in this section are performed aiming to investigate the chemical ozone loss mechanism for mid-latitudes summer in detail as well as to estimate how likely this ozone loss process occurs today for convective overshoot conditions in the lowermost stratosphere during the North American summertime. Therefore, the simulations are initialized based on measurements taken during the SEAC^{4}RS aircraft campaign.

4.1.1 Measurements

The box-model simulations are initialized using water vapour, ozone and CH_4 measurements taken during the SEAC^{4}RS aircraft campaign (more information on the chemical initialization is provided in Section 4.1.3). During the SEAC^{4}RS campaign three aircrafts were used including the NASA ER2-aircraft, which is qualified for high-altitude science missions (up to 21 km) and therefore able to sample air masses in altitudes of

the mid-latitude lowermost stratosphere. SEAC[4]RS was based in Houston, Texas, and took place during August and September 2013 (Toon et al., 2016). One aim of this campaign was to investigate the impact of deep convective clouds on the water vapour content and the chemistry in the lowermost stratosphere.

The model simulations presented here were initialized using measurements taken on 8 August 2013 during flights of the NASA ER-2 high altitude research aircraft. Considered water vapour measurements were sampled by the Harvard Lyman-α photofragment fluorescence hygrometer (HWV, Weinstock et al., 2009). Ozone is initialized in the simulations using O_3 measurements from the National Oceanic and Atmospheric Administration (NOAA) UAS-O_3-instrument (Gao et al., 2012). Initial Cl_y and NO_y are determined using tracer-tracer correlations (for more informations see Sec. 4.1.3) based on methane measurements with the Harvard University Picarro Cavity Ring down Spectrometer (HUPCRS) (Werner et al., 2017).

4.1.2 Trajectory calculations

Atmospheric chemistry is simulated along realistic trajectories calculated with CLaMS using total diabatic heating rates as well as winds and temperatures derived from the ECMWF ERA-Interim reanalysis (see Sec. 3.2). Since an enhancement of the water vapour content is expected to favour heterogeneous chlorine activation (Shi et al., 2001) and thus the ozone loss process analysed here, calculated trajectories are initialized at locations where enhanced stratospheric water vapour mixing ratios of more than 10 ppmv was measured in the lowermost stratosphere.

Figure 4.1 (top) shows the relative distribution of occurrence frequency of SEAC[4]RS measurements sampled above the tropopause in the temperature-H_2O correlation hereafter referred to as relative frequency distribution. The number of samples in temperature and water vapour bins of the size of $1\,K \times 1\,ppmv$ H_2O is calculated considering a water vapour range of 0–30 ppmv and temperatures between 195 and 230 K. The number of data points of each temperature-H_2O bin is normalized by the total number of samples taken above the tropopause during the SEAC[4]RS campaign. These fractions are colour-coded in Fig. 4.1.
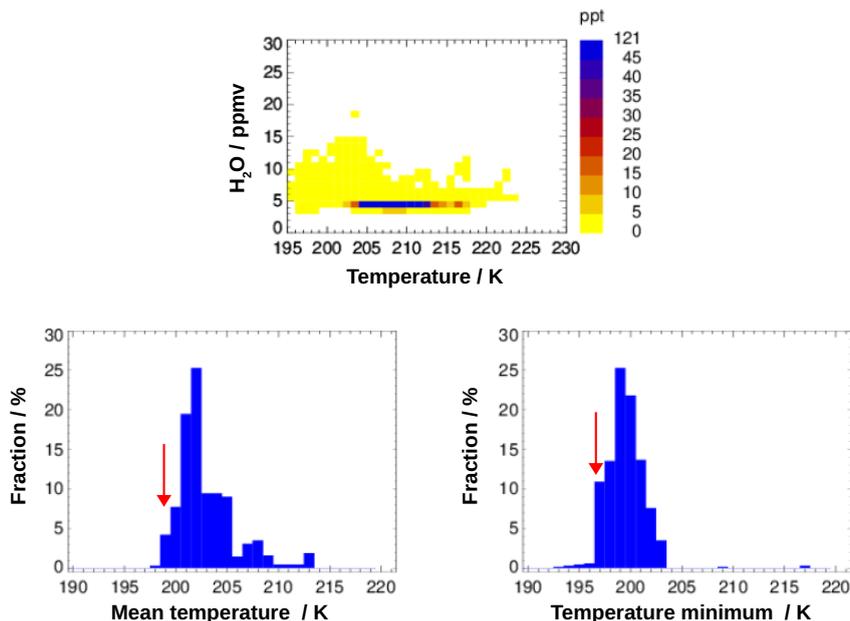
Figure 4.1: Relative frequency distribution of water vapour mixing ratios and temperatures measured above the tropopause during all ER2-flights of the SEAC⁴RS campaign (top). The colour scheme illustrates the fraction of measurements within a temperature- and water vapour bin in a size of $1\,K \times 1\,ppmv\ H_2O$ between $195\,K$ and $230\,K$ and from 0–$30\,ppmv\ H_2O$. The bottom panels show the temperature along all calculated forward and backward 7 day trajectories initialized at the time and location of a measurement with a water vapour mixing ratio lager than $10\,ppmv$. On the y-axis, the fraction of trajectories in that temperature regime is plotted. The mean temperature (left) and the minimum temperature (right) of each trajectory is shown.

Stratospheric water vapour mixing ratios measured during the SEAC⁴RS aircraft campaign mostly account to $\sim 5\,ppmv$, while measured temperatures mainly range between $205\,K$ and $212\,K$. Only 0.2% of the sampled air parcels hold significantly enhanced water vapour mixing ratios of more than $10\,ppmv$. The location of these measurements with enhanced water vapour are used to calculate 7 day forward and backward trajectories.

The temperature distribution of the calculated trajectories is shown in Fig. 4.1 (bottom) with respect to the mean temperature (left) and the minimum temperature (right) of a trajectory. The height of the bars represents the fraction of trajectories within

a temperature bin of 1 K in the range of 190–220 K. Most of the calculated forwards and backwards trajectories exhibit a mean temperature of 200–205 K and a minimum temperature of 198–201 K.

One of the calculated trajectories is selected as standard trajectory for analysing the mechanism of potential catalytic ozone destruction in mid-latitudes. This trajectory is chosen for the chemical analysis, because its initial conditions exhibit enhanced water vapour relative to the overall background (10.6 ppmv H_2O), low temperatures and enhanced Cl_y (higher than for comparable water vapour and temperature conditions). Cl_y is calculated from tracer-tracer correlations (see Sec. 4.1.3). The mean temperature of the selected trajectory is 199 K and the minimum temperature 197 K (marked with a red arrow in Fig. 4.1). This trajectory is then most suitable for the occurrence of the mechanism proposed by Anderson et al. (2012) due to the chemical initialization and the temperature along this trajectory.

The backward trajectory selected as standard trajectory here as well as a forward trajectory initialized based on the same SEAC[4]RS measurements are exemplary shown in Fig. 4.2. In the left panel, the backward trajectory is presented in the range of −7 to 0 days from the time of measurement (red line) and the forward trajectory in the range from 0 to 7 days. In the right panel, the location of the measurement is shown by a red square and the begin of the backward trajectory is marked by a green arrow. The backward trajectory is determined here to start at its earliest point in time and ends at the point of measurement.

The shown trajectories (Fig. 4.2, a forward and a backward trajectory) are based on measurements on 8 August 2013 during the SEAC[4]RS campaign. With a potential temperature of 380 to 390 K, these trajectories are above the tropopause of ∼366 K (Fig. 4.2 left, grey line), deduced from the temperature profile measured during the flight. Both, the forward and backward trajectories stay in the region of the North American continent. For the SEAC[4]RS campaign, the temperature range of the backward trajectory varies between 197 and 202 K and the forward trajectory exhibits increasing temperatures.

Since low temperatures and enhanced water vapour are expected to push stratospheric
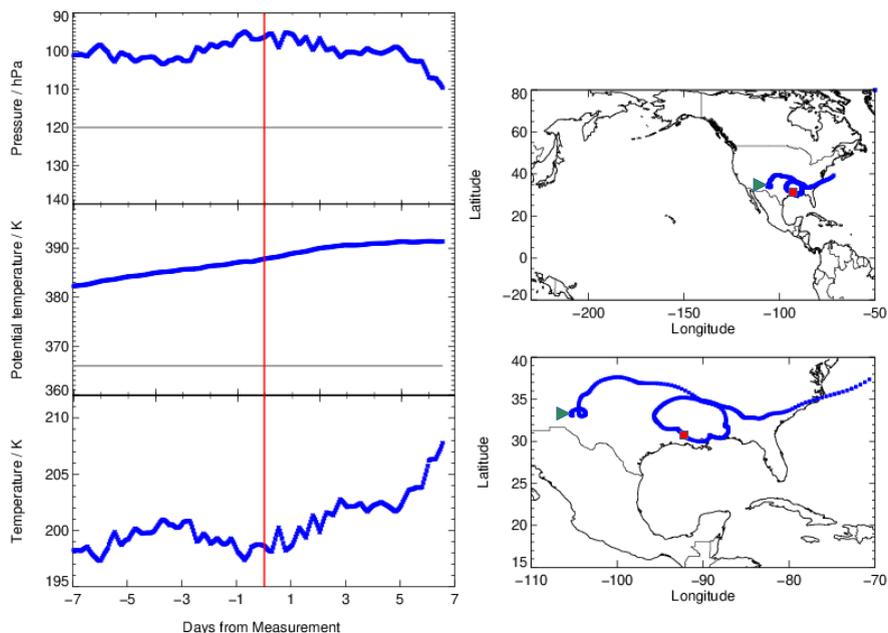
Figure 4.2: Pressure, potential temperature, temperature and location of selected 7-day trajectories (forward and backward) calculated based on measurements with enhanced water vapour during the SEAC[4]RS aircraft campaign. In the left panels, the backward trajectory starts at day -7 and ends at day 0 and the forward trajectory comprises the days 0–7. The grey line marks the approximate tropopause altitude, deduced from the temperature profile measured during the flight. The red line (left panel) marks the time of measurement and red squares (right panels) mark the location of the measurement. For the right panels, the bottom panel exhibits a zoom from the top panel and the begin of the backward-trajectory (1 August) is marked by a green arrow. The backward trajectory shown here is used as standard trajectory to analyse stratospheric chemistry under enhanced water vapour conditions.

ozone depletion in mid-latitudes (Anderson et al., 2012) due to faster heterogeneous chemical reactions and thus faster chlorine activation, the SEAC[4]RS backward trajectory (Fig. 4.2, day -7 to 0) is selected here as the standard trajectory. This trajectory is used to analyse the chemical mechanisms affecting lower stratospheric ozone under various water vapour conditions, and to explore the sensitivity of these processes to different initial conditions.

4.1.3 Chemical initialization

Stratospheric chemistry is simulated with the chemistry module of the CLaMS model (see Sec. 3.2) along the selected standard trajectory. Important trace gases for ozone chemistry – O_3, Cl_y and NO_y – are initialized based on measurements during the SEAC[4]RS aircraft campaign over North America (see Sec. 4.1.1). Ozone and water vapour were measured directly during the aircraft campaign. Cl_y and NO_y are inferred from tracer-tracer correlations using CH_4 measured on the aircraft employed. The initialization of all further trace gases except of water vapour are taken from the full chemistry 3D-CLaMS simulation (Vogel et al., 2015, 2016) for summer 2012 at the location of the measurement. Chemistry is initialized 7 days before the measurement. However, this time shift does not affect the sensitivities and the mechanism investigated here, because the trace gases Cl_y and NO_y are initialized based on measured CH_4 mixing ratios, which are not significantly changing during a 7-day box-model simulation.

Prior to the simulation, the initial aerosol number density is set to $N_0=10.0\,cm^{-3}$ and the standard deviation of the particle size normal distribution σ is set to 1.8. To investigate the impact of the sulfate amount on the chemical mechanism, three different sulfate amounts are assumed: a H_2SO_4 gas phase equivalent corresponding to the common chemical background amount ($0.2\,ppbv\,H_2SO_4$) as well as a threefold and a tenfold enhancement of H_2SO_4 (0.6 and $2.0\,ppbv\,H_2SO_4$ respectively, see Tab. 4.1).

Standard case

In the standard case, the initial values of O_3, Cl_y and NO_y are determined based on an observation with an enhanced water vapour content of $10.6\,ppmv$ (measured by

Table 4.1: Mixing ratios and sources used for initialization of relevant trace gases. The standard initialization is based on SEAC[4]RS measurements. Cl_y and NO_y values are determined based on tracer-tracer correlations (see Sec. 4.1.3). The high Cl_y case is based on Fig. 2 from Anderson et al. (2012). Initial mixing ratios of ClO_x species are assumed to be zero for all cases.

Species	Standard case			Case of high Cl_y	
	Value	Source	Sensitivity simulation	Value	Source
O_3	303.2 ppbv	UAS-O_3		303.2 ppbv	UAS-O_3
CH_4	1.76 ppmv	CLaMS-3D		1.76 ppmv	CLaMS-3D
CO	49.6 ppbv	CLaMS-3D		49.6 ppbv	CLaMS-3D
Cl_y	156 pptv	tracer corr.	80% Cl_y	1.00 ppbv	Anderson et al. (2012)
HCl	149.5 pptv	tracer corr.		850 pptv	Anderson et al. (2012)
$ClONO_2$	6.2 pptv	tracer corr.		150 pptv	Anderson et al. (2012)
NO_y	782.9 pptv	tracer corr.	80% NO_y	1.89 ppbv	
HNO_3	493.2 pptv	tracer corr.		1.19 ppbv	see section 4.1.3
NO	144.8 pptv	tracer corr.		325 pptv	Anderson et al. (2012)
NO_2	144.8 pptv	tracer corr.		375 pptv	Anderson et al. (2012)
Br_y	6.9 pptv	CLaMS-3D	50% Br_y	6.9 pptv	CLaMS-3D
H_2O	5–20 ppmv		5–20 ppmv	5–20 ppmv	
H_2SO_4	0.2 ppbv		0.6 ppbv, 2.0 ppbv	0.2 ppbv, 0.6 ppbv	
Temperature		standard trajectory	const. temp (195–220 K)		standard trajectory

the HWV-instrument) from the SEAC[4]RS (Toon et al., 2016) aircraft campaign. A gas phase equivalent mixing ratio for background sulphuric acid (H_2SO_4) of 0.20 ppbv is assumed. Initial CO (49.6 ppbv) is taken from the 3D-CLaMS simulation (Vogel et al., 2015), which is higher than the measured value of 34.74 ppbv (measured by the HUPCRS instrument). Simulations assuming the measured CO mixing ratio showed only a minor difference to the results presented here. The initial values for the main trace gases for the standard case are summarized in Table 4.1. Note, in the 3D-CLaMS simulation, the mixing ratios of HCl (131 ppt, CLaMS), O_3 (206 ppb, CLaMS) and

HNO_3 (354 ppt, CLaMS) are at the location of the SEAC^{4}RS measurement lower than in the standard initialization (see Tab. 4.1).

Since Cl_y and NO_y were not measured during the SEAC^{4}RS ER2-flights in the lowermost stratosphere, values for Cl_y and NO_y are calculated through tracer-tracer correlations (Grooß et al., 2014, see Appendix B for equations) based on a SEAC^{4}RS CH_4 measurement (of 1.776 ppmv) on 8 August 2013. The used Cl_y-CH_4 correlation was calculated from measurements of the Airborne Chromatograph for Atmospheric Trace Species (ACATS) during flights of the ER-2 aircraft and from measurements by the cryogenic whole air sampler of the university of Frankfurt (on board of the TRIPLE balloon gondola) during balloon flights at mid and high latitudes in the year 2000 (Grooß et al., 2002). Between the year 2000 and 2013, stratospheric CH_4 increased and Cl_y decreased. Hence, the change of both lowermost stratospheric CH_4 and Cl_y has to be taken into account when using this tracer-tracer correlation. The increase in CH_4 is estimated to be equivalent to the growth rate for tropospheric CH_4. This growth rate is calculated to be 45.8 ppbv from the year 2000 to 2013 by determining and adding every annual mean of the tropospheric CH_4 growth rate given in the GHG Bulletin (2014). Subtracting this increase of CH_4 from the measured CH_4 mixing ratio yields a CH_4 equivalent for the year 2000. From the CH_4 equivalent, an equivalent Cl_y mixing ratio for the year 2000 is calculated using the tracer-tracer correlation (Grooß et al., 2014, , see App. B). The annual decrease of Cl_y is assumed to be 0.8% (WMO, 2014) from the year 2000 to 2013, and thus the initial Cl_y is calculated to be 156 pptv. Since most Cl_y is deactivated in the mid-latitude lowermost stratosphere, the initial mixing ratio of ClO_x species is assumed to be zero. A simulation assuming a ClO mixing ratio of 1% of total Cl_y, does not yield a significant difference to the standard case.

Initial NO_y is calculated through a correlation with N_2O. Since no N_2O was measured on the ER2-flights during SEAC^{4}RS, stratospheric N_2O is first estimated through a methane correlation (Grooß et al., 2002), which is based on measurements from the year 2000. Hence, the equivalent CH_4 mixing ratio for the year 2000 (see above) is used to calculate an N_2O equivalent. Considering an estimated increase in N_2O of 10.4 ppbv from 2000 to 2013, which is determined in the same way as the CH_4 change (GHG

Bulletin, 2014), the N_2O mixing ratio related to the time of the measurement in 2013 is calculated. Afterwards NO_y is calculated with a correlation from (Grooß et al., 2014, see App. B) to be 782.9 pptv.

Because of the uncertain conditions in convective overshooting plumes, sensitivity box-model simulations are conducted. Furthermore, testing the impact of various parameters on chemical ozone loss is intended to yield a better understanding of the balance between stratospheric ozone production and ozone loss, which is a key aspect for potential mid-latitude ozone depletion. The sensitivity to variations in water vapour conditions on stratospheric ozone is tested by conducting simulations with standard conditions but varying the assumed water vapour mixing ratio from 5 to 20 ppmv in varying increments. In addition, simulations assuming the same water vapour range and a constant temperature in a range from 195–220 K are conducted assuming sulfate background conditions with a gas phase equivalent of 0.20 ppbv and 10×enhanced sulfate (2.00 ppbv) for illustrating the dependence of ozone loss on water vapour and temperature. Furthermore, sensitivity simulations are conducted, assuming 80% Cl_y, 80% NO_y or 50% Br_y, and a standard case simulation along a 19-day trajectory is calculated. An overview on the sensitivity simulations is given in Tab. 4.1.

Case of high Cl_y

Simulations referred to as "Case of high Cl_y" are conducted assuming high Cl_y and NO_y concentrations taken from Fig. 2 in Anderson et al. (2012). Fig. 2 in Anderson et al. (2012) presents a first example on the potential impact of enhanced water vapour mixing ratios on chemistry in the lowermost stratosphere by plotting the mixing ratios of HCl, ClO, $ClONO_2$, NO_2 and NO received within a 3 day box model simulation assuming both background and enhanced water vapour. Since the study of Anderson et al. (2012) was criticized in subsequent studies (Ravishankara, 2012; Schwartz et al., 2013) to assume chlorine mixing ratios higher than expected for realistic conditions, here the "Case of high Cl_y" constitutes a worst case scenario regarding the impact of a water vapour enhancement on lowermost stratospheric ozone in mid-latitudes.

In the "Case of high Cl_y", HNO_3 is determined to be 1.19 ppbv assuming the same ratio

for HNO_3 (63% of total NO_y) and $NO+NO_2$ (37% of total NO_y) as in the standard case. An overview of the important trace gases in the initialization is given in Tab. 4.1. The results of the case initialized with high Cl_y are compared with the results obtained from standard case simulations.

4.2 Mechanism of mid-latitude ozone chemistry

Mid-latitude ozone chemistry in the lowermost stratosphere depends amongst others on the water vapour abundance and the temperature. Here, the focus is on the water vapour dependence of stratospheric ozone chemistry by analysing chemical processes occurring in a box-model simulation along a realistic trajectory (the standard trajectory introduced in Sec. 4.1.2) in the temperature range from 197-202 K under several water vapour conditions.

In Figure 4.3, the mixing ratio of ozone, ClO_x and NO_x is shown for two simulations assuming 5 ppmv (dashed line) and 15 ppmv (solid line) H_2O. These water vapour mixing ratios are chosen, because they are clearly in the regime of the low water vapour background (5 ppmv) in the lower mid-latitude stratosphere and of enhanced water vapour (15 ppmv) as it can be reached through convective overshooting events. For the low water vapour (5 ppmv) case, net ozone formation occurs, the ClO_x mixing ratio remains low and the NO_x mixing ratio high. The fluctuations in the mixing ratios are due to the diurnal cycle. Assuming a water vapour mixing ratio of 15 ppmv, ozone depletion occurs, accompanied by a decrease in NO_x and coupled with chlorine activation as indicated by the increasing ClO_x mixing ratio.

In Figure 4.4 (top), the ozone values reached at the end of the 7-day box-model simulation (final ozone, blue squares) are plotted as a function of the water vapour mixing ratio assumed during a simulation. The initial (observed) ozone value of 303.2 ppbv is marked by the grey line. Blue squares lying above that line are cases with ozone production, those lying below that line are cases with ozone destruction.

The decrease of final ozone with higher water vapour mixing ratios is related to chlorine activation. The time until chlorine activation occurs in this simulation is plotted in
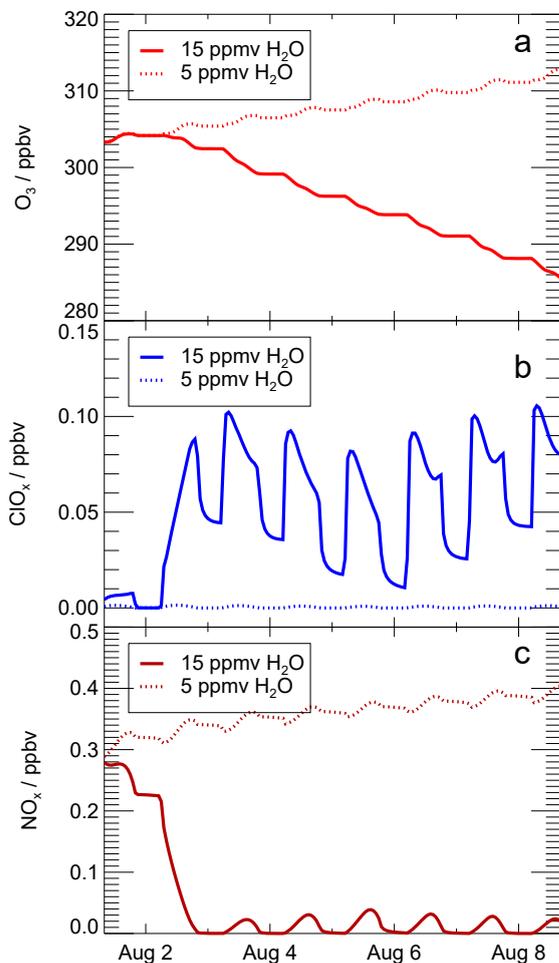
Figure 4.3: Volume mixing ratio of O_3 (a), ClO_x (b) and NO_x (c) during a simulation with 15 ppmv H_2O and a simulation with 5 ppmv H_2O. These water vapour mixing ratios are chosen, because they are clearly in the regime of low (5 ppmv) and elevated (15 ppmv) water vapour. Fluctuations in the mixing ratios are due to the diurnal cycle. The x-axis ticks refer to 00:00 local time (06:00 UTC).
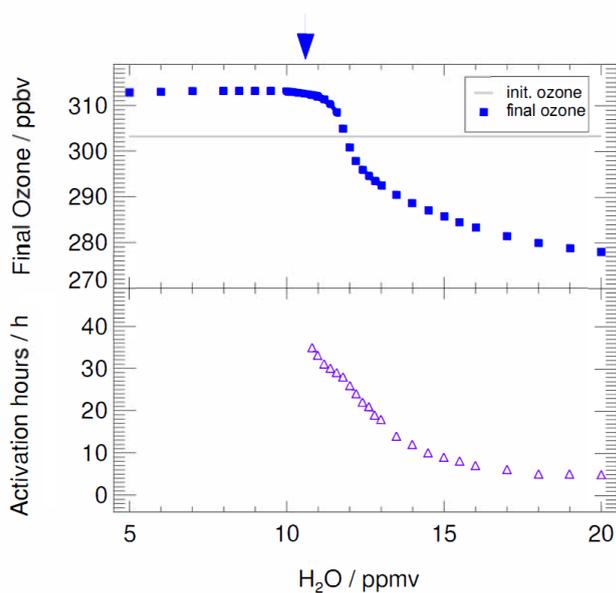
Figure 4.4: Impact of the water vapour content on the ozone mixing ratio (final ozone, blue squares) reached at the end of the 7-day simulation along the standard trajectory and assuming standard conditions. Water vapour mixing ratios plotted on the x-axis refer to the water vapour mixing ratio assumed during a simulation. The initial ozone amount is marked by the grey line. The arrow marks the water vapour threshold, which has to be exceeded for chlorine activation at standard conditions to occur. In the bottom panel, violet triangles show the time until chlorine activation occurs. For low water vapour mixing ratios no chlorine activation time is plotted, because no chlorine activation occurs.

Fig. 4.4 (bottom), assuming that chlorine activation occurs when the ClO_x mixing ratio exceeds 10% of total Cl_y (Drdla and Müller, 2012). Shown is the time when chlorine activation first occurs in the model. Since the ClO_x/Cl_y ratio depends on the diurnal cycle, the 24-hours mean value of the ClO_x mixing ratio is used to determine the chlorine activation time. For low water vapour mixing ratios, no chlorine activation time is plotted, because no chlorine activation occurs.

For chlorine activation to occur, a threshold in water vapour has to be reached. Here, the lowest water vapour mixing ratio at which chlorine activation occurs is determined as the water vapour threshold (marked by a blue arrow in Fig. 4.4). In the standard

case, this threshold is reached at a water vapour mixing ratio of 10.6 ppmv. Between 10.6 and 11.8 ppmv H_2O, chlorine activation leads not to an ozone destruction during the 7-day simulation. For 10.6–11.2 ppmv H_2O, chlorine only remains activated for up to 28 h, because of increasing temperatures of the standard trajectory. Thus, almost no impact on final ozone is observable. By 12.0 ppmv of water vapour, chlorine activation causes ozone destruction within the 7-day simulation. Near the water vapour threshold, the activation time is 24 to 36 hours and it decreases with increasing water vapour mixing ratios. Chlorine activation requires 5 hours at 20 ppmv H_2O. The shorter the chlorine activation time, the longer activated chlorine exists during the simulation causing greater ozone depletion.

The processes causing ozone depletion at high water vapour conditions as well as ozone formation at low water vapour are analysed in the subsequent sections. For this investigation, the simulated reaction rates are used for each chemical reaction along the course of the calculation. For high water vapour mixing ratios the roles of both chlorine activation and a decrease in the NO_x mixing ratio (as shown in Fig. 4.3) are discussed.

4.2.1 Ozone formation at low water vapour mixing ratios

At water vapour mixing ratios up to 11.8 ppmv, net ozone formation occurs during the 7-day simulation (see Fig. 4.4). This ozone formation is mainly driven by the photolysis of O_2 (R 1). Additionally the "Ozone Smog Cycle" (C3) (Haagen-Smit, 1952) known from tropospheric chemistry can yield ozone formation in the lower stratosphere (Grenfell et al., 2006; Grooß et al., 2011). The rate of this cycle is determined by reaction R 9

$$OH + CO \ \rightarrow \ CO_2 + H \hspace{3cm} (R\,9)$$

at low water vapour mixing ratios. The ozone formation through cycle C3 contributes around 40% to the total ozone formation at 5 ppmv in the box model standard simulation. Hence, the ozone formation which occurs in the simulations assuming low water vapour mixing ratios is due to both the photolysis of O_2 and cycle C3.

4.2.2 Ozone loss at high water vapour mixing ratios

For water vapour mixing ratios higher than 12 ppmv, net ozone depletion is simulated (Fig. 4.4) in the 7-day standard simulation. The ozone loss mechanism generally consists of two phases: in the first phase chlorine activation dominates transferring inactive chlorine (mainly HCl) into active ClO_x followed by the second phase dominated by catalytic ozone loss processes (Anderson et al., 2012). In this section, both phases are analysed the chlorine activation step and subsequent catalytic ozone loss cycles potentially occurring in mid-latitudes in the lower stratosphere under enhanced water vapour conditions. Since ozone depletion is larger at high water vapour mixing ratios, conditions with a water vapour mixing ratio of 15 ppmv are chosen here to analyse the chemical ozone loss mechanism. Figure 4.5 shows an overview on important mixing ratios and reaction rates during the 7-day simulation. The temperature (black line) and the surface area density of liquid particles (blue line) are shown in Fig. 4.5 a.

The first phase of the ozone loss mechanism (dark grey background in Fig. 4.5) is dominated by the occurrence of heterogeneous reactions. The most important heterogeneous chlorine activation reaction is R 21 (Fig. 4.5b, light blue), which leads to the chlorine activation chain (von Hobe et al., 2011)

$$ClO + NO_2 + M \rightarrow ClONO_2 + M \qquad (R\,30)$$

$$ClONO_2 + HCl \xrightarrow{het.} Cl_2 + HNO_3 \qquad (R\,21)$$

$$Cl_2 + h\nu \rightarrow 2\,Cl \qquad (R\,31)$$

$$2 \times (Cl + O_3 \rightarrow ClO + O_2) \qquad (R\,16)$$

$$HCl + NO_2 + 2\,O_3 \rightarrow ClO + HNO_3 + 2\,O_2 \cdot$$
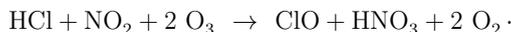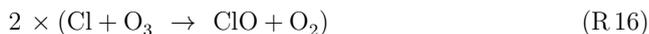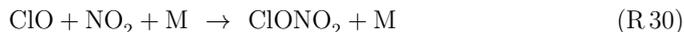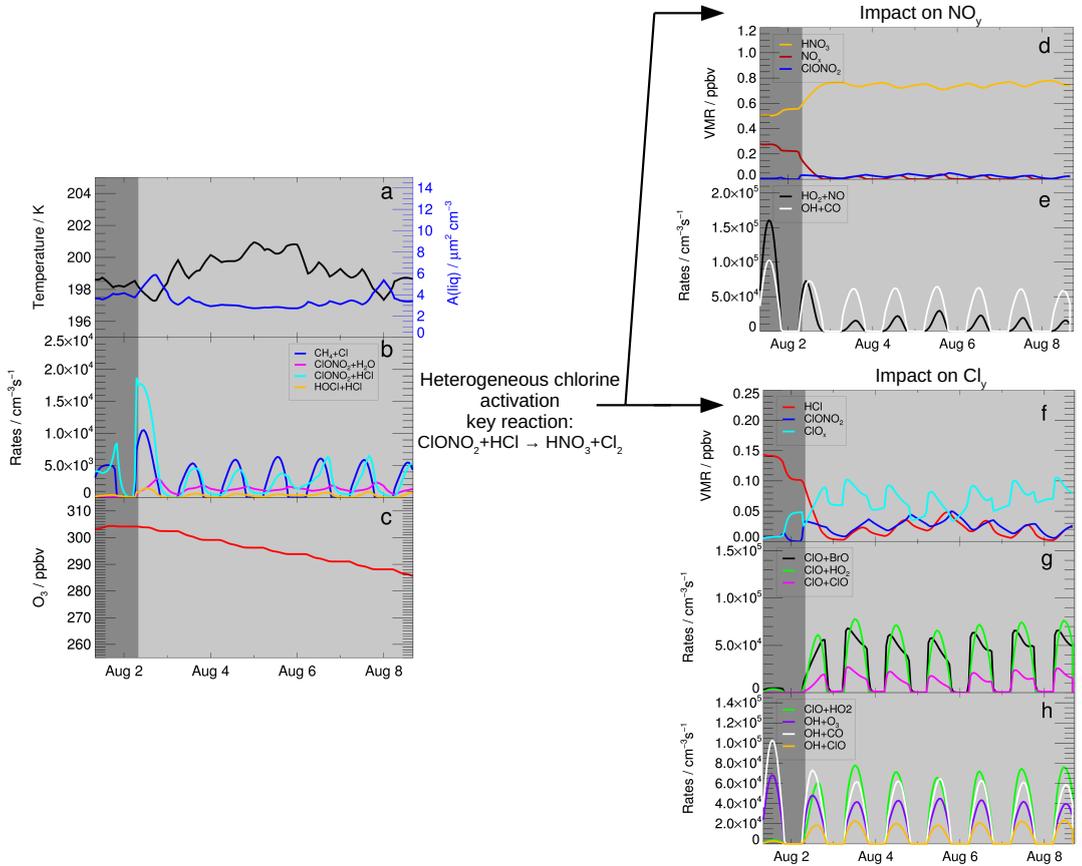
Figure 4.5: Reaction rates and mixing ratios important for the ozone loss mechanism in the standard simulation assuming 15 ppmv H_2O. The chlorine activation phase is shaded in dark grey, while the phase of ozone loss has a light grey background. Shown are the temperature of the trajectory and the liquid surface area density (a) and the ozone mixing ratio (c). Further, heterogeneous reaction rates (R 21–R 23) are shown (b) as well as the rate of the gas phase reaction $CH_4 + Cl$ (R 24) (b). For demonstrating the role of NO_y for the ozone loss process, the mixing ratio of HNO_3 (gas phase + condensed), NO_x and $ClONO_2$ is shown (d). Reaction R 9 (OH+CO) (e) limits ozone formation in cycle C3 at high NO_x mixing ratios and R 11 ($HO_2 + NO$) at lower NO_x concentrations. The role of chlorine for ozone loss is demonstrated by showing the mixing ratio of HCl, ClO_x and $ClONO_2$ (f), main reaction rates (R 13 (ClO+ClO), R 17 (ClO+BrO), R 19 (ClO + HO_2)) for catalytic ozone loss cycles (g) and potential reaction pathways for the OH-radical (R 9 (OH+CO), R 32 (OH+ClO), R 8 (OH+O_3)) as possible reaction chains following R 19 (ClO+HO_2) (h). Fluctuations in the mixing ratios are caused by the diurnal cycle. The x-axis ticks refer to 00:00 o'clock local time (06:00 UTC).

This chlorine activation chain yields a transformation of inactive HCl into active ClO_x as well as of NO_x into HNO_3. The ozone loss due to this reaction chain is negligible and no depleting effect on ozone occurs during the first phase (Fig. 4.5c). In Fig. 4.5d, the NO_x mixing ratio is seen to decrease during the first phase and HNO_3 increases due to R 21. Further, the HCl mixing ratio decreases, causing an increase of ClO_x (Fig. 4.5f). Both decreasing NO_x and increasing ClO_x influence ozone chemistry during the second phase of the ozone loss mechanism (light grey background in Fig. 4.5), which is characterized by a decreasing ozone mixing ratio (Fig. 4.5c). The role of NO_x and ClO_x is discussed in detail in the next sections.

Role of NO_x

NO_x-radicals are transferred into HNO_3 is due to R 30 (ClO +NO_2) and subsequent the occurrence of the heterogeneous reactions R 21 ($ClONO_2$ + HCl) and R 23 ($ClONO_2$ + H_2O), which form HNO_3. This behaviour was also found in former studies (e.g. Keim et al., 1996; Pitari et al., 2016; Berthet et al., 2017), investigating the impact of volcanic aerosols on stratospheric ozone chemistry. Dependent on the temperature and water vapour content, the HNO_3 formed remains in the condensed particles. In the standard simulation using 15 ppmv H_2O, 64% of HNO_3 remains in the condensed phase on the day with the lowest temperature (197.3 K, 2 Aug 2013), while at higher temperatures (4–7 August 2013) 85% of HNO_3 are released to the gas phase. After the transformation of NO_x into HNO_3, the NO_x mixing ratio remains low in the second phase of the mechanism (Fig. 4.5d, light grey region) while the HNO_3 mixing ratio (condensed + gas phase) remains high.

The transformation of NO_x radicals into HNO_3, due to the occurrence of heterogeneous reactions at elevated water vapour amounts, affects stratospheric ozone chemistry. In the presence of a high NO_x concentration (as at low water vapour mixing ratios), ozone formation in cycle C3 is determined by the rate of R 9 (OH+CO). If the NO_x concentration is low (as in the second phase of the mechanism), this ozone formation cycle is rate limited by R 11 (NO + HO_2). For the standard case at 15 ppmv H_2O, both rates are shown in Fig. 4.5e. In the first phase before NO_x is transferred into HNO_3,

cycle C3 is limited by R 9 (OH+CO) which peaks on 1 August 2013 with a maximum rate of $1.0 \cdot 10^5 \, \text{cm}^{-3} \text{s}^{-1}$. In the second phase at low NO_x concentrations, cycle C3 is limited by R 11 ($NO + HO_2$) which peaks on 3 August 2013 with a maximum rate of $1.5 \cdot 10^4 \, \text{cm}^{-3} \text{s}^{-1}$. Hence, due to the transformation of NO_x to HNO_3 through the heterogeneous reaction R 21 the net ozone formation decreases in the first phase of the mechanism (dark grey in Fig. 4.5).

Role of ClO_x

In the first phase of the mechanism, the transformation of inactive chlorine (mainly HCl) into active ClO_x results in chlorine activation (Fig. 4.5f). Net chlorine activation occurs when the rates of the heterogeneous reactions R 21 ($ClONO_2 + HCl$), R 22 ($HCl + HOCl$) and R 23 ($ClONO_2 + H_2O$) exceed the gas phase HCl formation dominated by the reaction

$$Cl + CH_4 \rightarrow HCl + CH_3 \cdot \qquad \text{(R 24)}$$

Enhanced ClO_x concentrations induce catalytic ozone loss cycles at low temperatures, as the ClO-Dimer-cycle (C4) (Molina et al., 1987), the ClO-BrO-cycle (C5) (McElroy et al., 1986) and the cycle with ClO and HO_2 (C6) (Solomon et al., 1986). Under conditions of low water vapour (stratospheric background), the rate limiting steps of these cycles are the reactions

$$ClO + ClO + M \rightarrow ClOOCl + M \qquad \text{(R 13)}$$
$$ClO + BrO \rightarrow Br + Cl + O_2 \qquad \text{(R 17)}$$
$$\text{and} \quad ClO + HO_2 \rightarrow HOCl + O_2 \cdot \qquad \text{(R 19)}$$
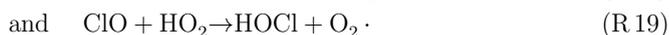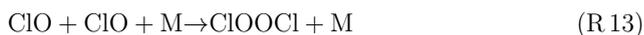
The rates of the reactions R 13, R 17 and R 19 increase strongly in the second phase of the mechanism (light grey area in Fig. 4.5g) and thus catalytic ozone loss cycles occur. Under the assumed conditions, ozone depletion is mainly driven by reaction pathways following both R 17 and R 19. The reaction rates peak on August 3 with a value of $7.8 \cdot 10^4 \, \text{cm}^{-3} \text{s}^{-1}$ for R 19 ($ClO+HO_2$), $6.8 \cdot 10^4 \, \text{cm}^{-3} \text{s}^{-1}$ for R 17 ($ClO+BrO$) and $2.7 \cdot 10^4 \, \text{cm}^{-3} \text{s}^{-1}$ for R 13 ($ClO+ClO$).
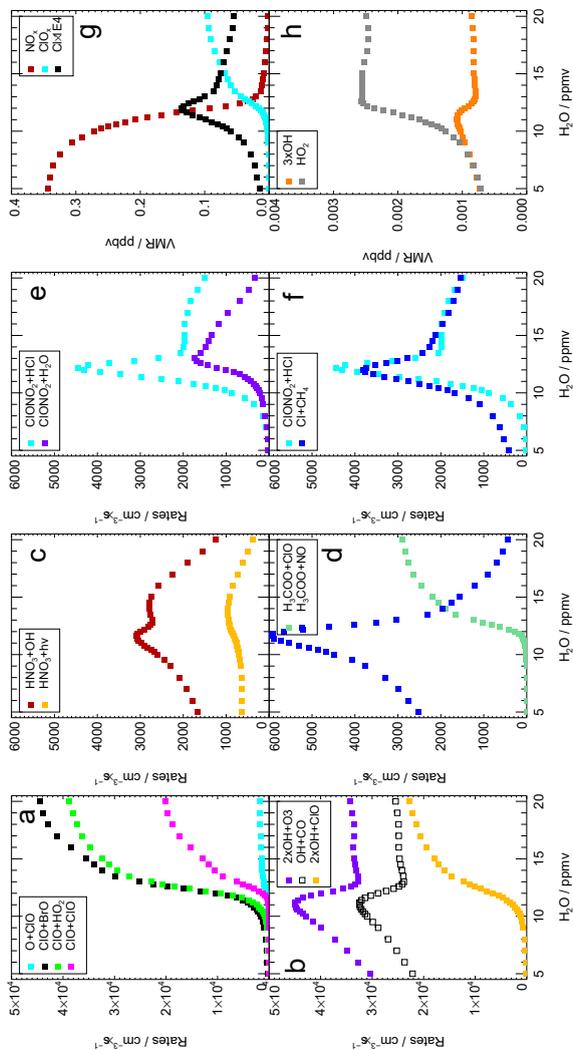
Figure 4.6: Average reaction rates and volume mixing ratios from the standard simulations on 3rd of August dependent on the water vapour content. The rates of the reactions R 13 (ClO + ClO), R 17 (ClO + BrO), R 19 (ClO + HO$_2$) and ClO + O(^{3}P) → Cl + O$_2$ (a) resulting in ozone reduction are shown as well as possible reaction pathways for the OH radical (R 8 (OH + O$_3$), R 9 (OH + CO) and R 32 (OH + ClO)) (b), reactions yielding depletion of HNO$_3$ (R 33 (HNO$_3$ + OH), R 34 (HNO$_3$ + hν)) (c), reactions of the H$_3$COO-radical R 35 (H$_3$COO + NO) and R 36 (H$_3$COO + ClO) (d), important heterogeneous reactions (R 21 (ClONO$_2$ + HCl), R 23 (ClONO$_2$ + H$_2$O)) (e), and the balance between R 21 (ClONO$_2$ + HCl) and R 24 (CH$_4$ + Cl) (f). Further, the mixing ratios of NO$_x$, ClO$_x$ and 10×Cl (g) and of OH and HO$_2$ (h) are shown.

The sensitivity of the rates of these reactions to the water vapour mixing ratio is tested. In Figure 4.6, the mean reaction rates on 3 August are plotted against the water content assumed during the simulation. The ClO-BrO-cycle C5 (based on R 17) and cycle C6 (based on R 19) accelerate beginning from a water vapour mixing ratio of 11 ppmv (Fig. 4.6 a). The rate determining reaction of the ClO-Dimer-Cycle C4 (based on R 13) increases at a higher water vapour mixing ratio. In contrast, the rate of ozone loss due to the reactions between ClO_x and O_x species is negligible here (as shown by the low rate of the reaction $ClO + O(^3P) \rightarrow Cl + O_2$, Fig. 4.6a).

At stratospheric background conditions with a low water vapour mixing ratio, the rate determining step of cycle C6 is R 19 (Solomon et al., 1986; Ward and Rowley, 2016). For the conditions with enhanced water vapour of 15 ppmv in the standard simulation, the rate of R 8 ($OH+O_3$) limits this cycle (Fig. 4.5f). An investigation of possible reaction pathways of the OH-radical yields that reactions of OH with CO (R 9) and ClO (R 32) exhibit a rate similar to the reaction with ozone (R 8, Fig. 4.6b).

$$OH + CO \quad \rightarrow \quad H + CO_2 \qquad\qquad (R\,9)$$
$$OH + ClO \quad \rightarrow \quad HO_2 + Cl \qquad\qquad (R\,32)$$

Based on these reactions, two further reaction chains affecting ozone can be deduced. In cycle C7, the OH-radical reacts with CO yielding CO_2 and a hydrogen radical, from which HO_2 is formed. Subsequently HOCl can be formed via R 19 ($ClO+HO_2$) and photolysed in reaction R 20. Thus, the net reaction of this pathway is the oxidation of CO to CO_2 and the simultanous destruction of ozone (C7).

$$OH + CO \quad \rightarrow \quad H + CO_2 \qquad\qquad (R\,9)$$
$$H + O_2 + M \quad \rightarrow \quad HO_2 + M \qquad\qquad (R\,10)$$
$$ClO + HO_2 \quad \rightarrow \quad HOCl + O_2 \qquad\qquad (R\,19)$$
$$HOCl + h\nu \quad \rightarrow \quad Cl + OH \qquad\qquad (R\,20)$$
$$Cl + O_3 \quad \rightarrow \quad ClO + O_2 \qquad\qquad (R\,16)$$

$$\overline{\qquad\qquad\qquad\qquad\qquad\qquad\qquad\qquad}$$

$$CO + O_3 + h\nu \rightarrow CO_2 + O_2 \qquad\qquad (C7)$$
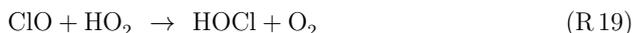
Furthermore, the catalytic ozone loss cycle C8 results when the OH-radical reacts with ClO.

$$
\begin{array}{rcll}
OH + ClO & \rightarrow & HO_2 + Cl & \text{(R 32)} \\
ClO + HO_2 & \rightarrow & HOCl + O_2 & \text{(R 19)} \\
HOCl + h\nu & \rightarrow & Cl + OH & \text{(R 20)} \\
2 \text{ x } (Cl + O_3 & \rightarrow & ClO + O_2) & \text{(R 16)} \\
\hline
\end{array}
$$

$$2O_3 \rightarrow 3O_2 \qquad\qquad \text{(C8)}$$
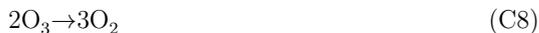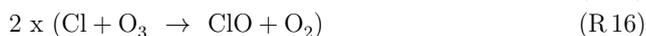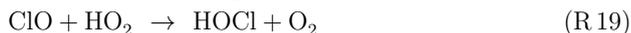
In the cycles C6 and C8 two ozone molecules are destroyed, while one ozone molecule is destroyed in C7. To assess the effectiveness regarding ozone loss of C6 – C8, the rate of R 9 (limiting C7) is compared with two times the rate of R 8 (limiting C6) and R 32 (limiting C8). This comparison shows that cycle C6 is more relevant for ozone loss than C7 and C8 (Fig. 4.6b). However, the relevance of C8 for catalytic ozone destruction increases for higher water vapour mixing ratios.

A requirement for the effectiveness of the ozone loss cycles is a high mixing ratio of activated chlorine (ClO_x). In Fig. 4.5b, the rate of the main HCl-formation reaction R 24 (Cl +CH_4, dark blue) is shown, which causes a formation of HCl. This HCl formation is mainly balanced by the heterogeneous HCl-destruction reaction R 21 ($ClONO_2$ +HCl) holding the HCl mixing ratio low and thus ClO_x values high. The balance between chlorine activation (R 21, $ClONO_2$ +HCl) and chlorine deactivation (R 24, Cl+CH_4) is schematically illustrated with blue arrows in Fig. 4.7 and similar to HCl-null-cycles (Müller et al., 2018), which balance gas phase HCl-formation and heterogeneous HCl-destruction under Antarctic polar night conditions. In these polar HCl-null-cycles, each HCl formed in reaction R 24 is depleted through the heterogeneous reaction R 22 (HCl+HOCl). For the conditions in the mid-latitudes during summer considered here, a higher NO_x mixing ratio prevails than under Antarctic ozone hole

conditions. As a consequence R 21 ($ClONO_2$ + HCl) is here mainly responsible for
HCl-depletion.

Reaction R 21 combined with R 30 (ClO + NO_2) yields additionally the transformation
of NO_x into HNO_3. This HNO_3 formation is balanced by reaction

$$HNO_3 + OH \rightarrow H_2O + NO_3 \qquad \text{(R 33)}$$

(schematically illustrated in Fig. 4.7, green), leading to a steady HNO_3 mixing ratio in
the second phase of the mechanism (Fig. 4.5d, light grey). A further option to convert
HNO_3 into active NO_x may be the HNO_3-photolysis

$$HNO_3 + h\nu \rightarrow NO_2 + OH, \qquad \text{(R 34)}$$

but the rate of reaction R 33 is more than 2.5 times larger than the rate of the HNO_3
photolysis (R 34, Fig. 4.6c).

Hence, the heterogeneous reaction R 21 couples two pathways: A pathway balancing
HCl-destruction in R 21 and HCl-formation in R 24 (Cl + CH_4) and thus maintaining a
high ClO_x mixing ratio, and a pathway balancing HNO_3-formation in R 21 and HNO_3
destruction in R 33 and thus maintaining a low NO_x mixing ratio.

Radical species converted in these pathways (HO_x, ClO_x, NO_x) are likewise balanced,
additionally linking the pathway balancing HCl-formation and -destruction (Fig. 4.7
blue) with the pathway balancing HNO_3 formation and destruction (Fig. 4.7 green).
This balance is schematically illustrated in Fig. 4.7 (pastel colours). In reaction R 24,
besides HCl a methylperoxy radical (H_3COO) is formed, which reacts either with NO
or with ClO leading to HO_x-formation (grey in Fig. 4.7).

$$H_3COO + NO \;\rightarrow\; HCHO + H + NO_2 \qquad \text{(R 35)}$$
$$H_3COO + ClO \;\rightarrow\; HCHO + HO_2 + Cl \qquad \text{(R 36)}$$
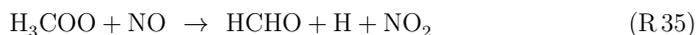
HO_x-radicals contribute to the balance between HCl and HNO_3 formation and destruc-
tion (Fig. 4.7, yellow).
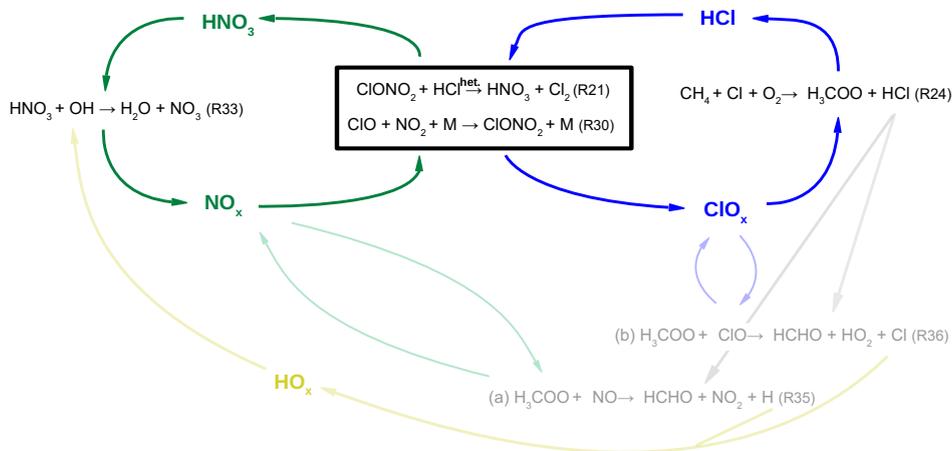
Figure 4.7: Reaction scheme to illustrate the balance between chlorine activation and chlorine deactivation (blue, right) and NO_x activation and deactivation (green, left). The heterogeneous reaction $ClONO_2$+HCl (R 21) links both cycles. Additional reaction pathways, which balance radicals are shown in light colours.

How the H_3COO-radical reacts, depends on the mixing ratios of ClO_x and NO_x. For water vapour mixing ratios around the water vapour threshold, the NO_x mixing ratio is higher than the ClO_x mixing ratio (Fig. 4.6g). Hence, the methylperoxy radical rather reacts with NO than with ClO (Fig. 4.6d) leading to pathway (a) in Fig. 4.7. At higher water vapour mixing ratios, H_3COO rather reacts with ClO (R 36) leading to pathway (b) in Fig. 4.7. Anyway, both pathway (a) and pathway (b) describe the additional balance of radical species accompanying the balance between HCl-formation and -destruction as well as HNO_3-formation and -destruction in the reactions R 21 ($ClONO_2$ + HCl), R 24 (CH_4 + Cl) and R 33 (HNO_3 + OH). The reaction pathway balancing HCl and HNO_3 formation and destruction at high water vapour mixing ratios was analysed by Müller et al. (2018) and Robrecht (2016) and is further described in the Appendix C.

Here, the heterogeneous HCl-destruction (R 21, $ClONO_2$ +HCl) does not balance the HCl-formation (R 24, CH_4 + Cl) completely (Fig. 4.5b), because the temperatures of the standard trajectory increase (Fig. 4.5a). Higher temperatures decelerate the heteroge-

neous HCl-destruction and thus result in the slightly increasing HCl-mixing ratio from
4 August–7 August 2013 (Fig. 4.5f). Such temperature fluctuations (Fig. 4.5a) affect the
balance between HCl formation and destruction less at higher water vapour mixing
ratios, because the heterogeneous HCl-destruction rate (R 21) increases for both low
temperatures and high water vapour mixing ratios (see Sec. 4.3). Thus, regarding the
balance between HCl formation and HCl destruction (and hence the balance between
chlorine deactivation and chlorine activation), a high water vapour mixing ratio can
compensate a small range of temperature fluctuations.

In summary, the key step for ozone loss cycles to occur is the heterogeneous reaction
R 21 transforming inactive HCl in active ClO_x radicals. After chlorine activation, high
ClO_x mixing ratios are maintained by chlorine activation dominated by reaction R 21
balancing chlorine deactivation in reaction R 24. This is essential for catalytic ozone
loss cycles (C4, C5, C6–C8) to proceed in the second phase of the mechanism.

4.3 Analysis of chlorine activation

As shown in the previous section, there is a threshold for water vapour in the temperature
range of 197–202 K, which has to be exceeded to yield chlorine activation and thus
to enable substantial ozone destruction. Now, the sensitivity of this threshold on the
sulfate content, temperature, Cl_y and NO_y mixing ratio is investigated.

4.3.1 Sensitivity of the water vapour threshold

Modifying the temperature, sulfate amount or the mixing ratios of Cl_y or NO_y leads to
a shift of the water vapour threshold. Figure 4.8 shows the ozone values reached at the
end of the 7-day simulation (final ozone) for a variety of sensitivity cases assuming the
standard trajectory. For each case, the water vapour threshold is marked with an arrow
in the colour of the corresponding case.

The water vapour dependent final ozone values for the standard case are plotted as blue
squares (Fig. 4.8) with a water vapour threshold of 10.6 ppmv (see Sec. 4.2). Raising the
trajectory temperature by 1 K over the standard case leads to a higher water vapour

threshold of 13.0 ppmv (open red squares), while increasing the sulfate content by a factor of 3 results in a lower threshold region of $\sim$9.0 ppmv (yellow diamonds). An even larger enhancement of the sulfate content ($10\times$ H_2SO_4, magenta diamonds) lowers the water vapour threshold further to a value near $\sim$8 ppmv. Reducing the NO_y mixing ratio to 80% of the standard case yields a shift of the threshold to a lower water vapour mixing ratio (green filled triangles), while an equivalent reduction in the Cl_y mixing ratio shifts the threshold to higher water vapour mixing ratios (black circles). A reduction in Cl_y also reduces ozone destruction and hence results in higher ozone mixing ratios at the end of the simulation. The observed sensitivity of the water vapour threshold to temperature, sulfate abundance and Cl_y and NO_y mixing ratio is explained in the next Section (Sec. 4.3.2).

  As a further example for an event with high stratospheric water vapour mixing ratios based on airborne measurements, simulations based on measurements during the Mid-latitude Airborne Cirrus Properties Experiments (MACPEX Rollins et al., 2014) are conducted. This campaign was based in Texas during springtime 2011 and hence prior to the formation of the North American Monsoon (NAM). A detailed description of this MACPEX case is given in the Appendix (App. D). For the MACPEX case, changes in sulfate, Cl_y and NO_y mixing ratios affect the water vapour threshold similarly to that observed for the SEAC[4]RS trajectory. Thus, the MACPEX results confirm the SEAC[4]RS findings. Therefore, it can be concluded that in the considered temperature range ($\sim$197–202 K), an ozone reduction occurs after exceeding a certain water vapour threshold and that this threshold varies with Cl_y, NO_y, sulfate content and temperature.

4.3.2 Explanation of the water vapour threshold

In the previous section was shown, that the mixing ratio of Cl_y and NO_y, the temperature and the sulfate abundance affect the water vapour threshold. In this section it is investigated in more detail, how the threshold in water vapour is affected. Therefore, the focus is on the balance between heterogeneous chlorine activation mainly due to R 21 ($ClONO_2 + HCl$) and gas phase chlorine deactivation mainly due to R 24 ($Cl + CH_4$). Net chlorine activation takes place when the chlorine activation rate exceeds the chlorine
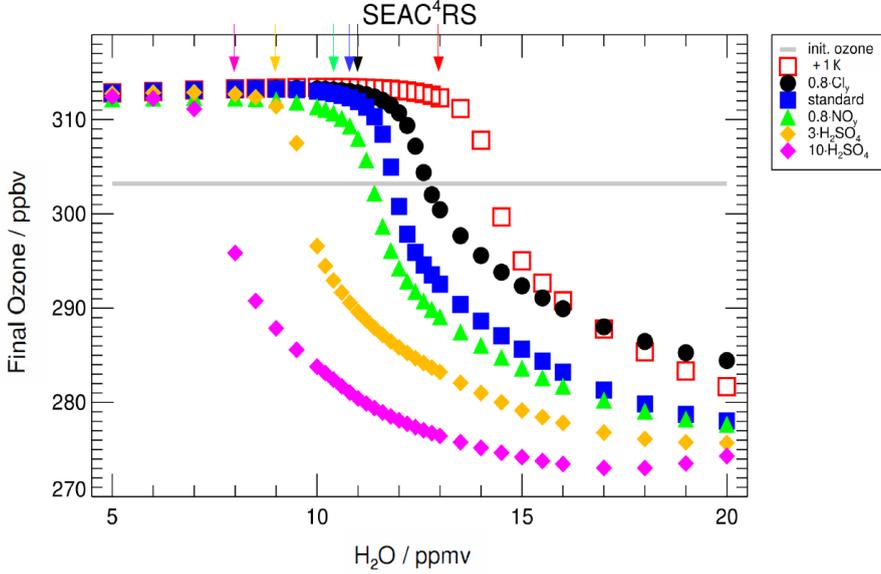
Figure 4.8: Impact of the water vapour content on the ozone mixing ratio (final ozone) reached at the end of the 7-day simulation along the standard trajectory (SEAC^{4}RS). The standard case is shown in blue and the initial ozone amount is marked by the grey line. An impact on the final ozone mixing ratios is observable after exceeding a critical threshold in water vapour, which is marked with an arrow for the different cases. This threshold changes with a shift in trajectory temperature ($+1\,\mathrm{K}$, red), the $\mathrm{Cl_y}$ mixing ratio to $0.8\,\mathrm{Cl_y}$ (black), the $\mathrm{NO_y}$ mixing ratio ($0.8\,\mathrm{NO_y}$, green) and the sulfate content ($3\times$ standard $\mathrm{H_2SO_4}$, yellow and $10\times$ standard $\mathrm{H_2SO_4}$, magenta).

deactivation rate. Reaction R 21 is the key reaction in the chlorine activation process. Therefore, in the following, first the dependence of R 21 on the water vapour content is analysed in detail. Second, the balance between chlorine activation and deactivation is investigated, also considering the impact of $\mathrm{Cl_y}$, $\mathrm{NO_y}$, sulfate and temperature on the water vapour threshold.

In general the rate of R 21 ($\mathrm{ClONO_2 + HCl}$) $v_{\mathrm{R\,21}}$ is determined through:

$$v_{\mathrm{R\,21}} = k_{\mathrm{R\,21}} \cdot c_{\mathrm{ClONO_2}} \cdot c_{\mathrm{HCl}} \qquad (1)$$

The concentrations of $ClONO_2$ c_{ClONO_2} and HCl c_{HCl} are associated with the gas phase mixing ratio and the rate constant k_{R21}, as a measure of the reactivity of the heterogeneous reaction, depends in this case on the γ-value γ_{R21}, the surface area density of the liquid particle A_{liq}, the temperature T and c_{HCl} (Eq. 2) (Shi et al., 2001).

$$k_{R21} \propto \frac{\gamma_{R21} \cdot A_{liq} \cdot \sqrt{T}}{1 + c_{HCl}} \tag{2}$$

The γ-value describes the uptake of $ClONO_2$ into liquid particles due to the decomposition of $ClONO_2$ in reaction R 21 and is thus a measure of the probability of the occurrence of this heterogeneous reaction (Shi et al., 2001). Laboratory studies showed a dependence of γ_{R21} on the solubility of HCl in the droplet, which generally increases for a lower H_2SO_4 fraction in the particle (H_2SO_4 wt%) (Elrod et al., 1995; Hanson, 1998; Zhang et al., 1994; Hanson and Ravishankara, 1994). From Eq. 2 it is obvious that a large surface area A_{liq} and a high γ-value γ_{R21} increase k_{R21} and thus the heterogeneous reaction rate v_{R21}.

In Figure 4.9, the impact of the water vapour content on the H_2SO_4 weight-percent, the γ-value γ_{R21}, the surface area density A_{liq}, the rate constant k_{R21} and the reaction rate v_{R21} is shown. To avoid the influence of R 21 itself on these parameters as much as possible, these parameters are selected for 1 August 2013 at 13:00 UTC. This point in time corresponds to the values after the first chemistry time step during the chemical simulation. The particles H_2SO_4 wt% decreases with increasing water vapour from more than 50 wt% at 5 ppmv H_2O to around 20 wt% at 20 ppmv H_2O due to an increasing uptake of H_2O in the thermodynamic equilibrium.

The standard case is illustrated in blue squares (Fig.4.9) and exhibits a strongly increasing γ-value especially for water vapour mixing ratios between 9 and 14 ppmv due to the decrease in H_2SO_4 wt%. In the same water vapour range, the liquid surface area density A_{liq} increases slightly. It increases more for higher water vapour mixing ratios because of HNO_3 uptake into the particles. Due to the increasing γ-value with increasing water vapour, the rate constant k_{R21} increases (Eq. 2, Shi et al., 2001) and thus induces a larger reaction rate v_{R21} with an increasing water vapour mixing ratio (Eq. 1).

At low water vapour mixing ratios, not only the rate of R 21 ($ClONO_2 + HCl$) but also
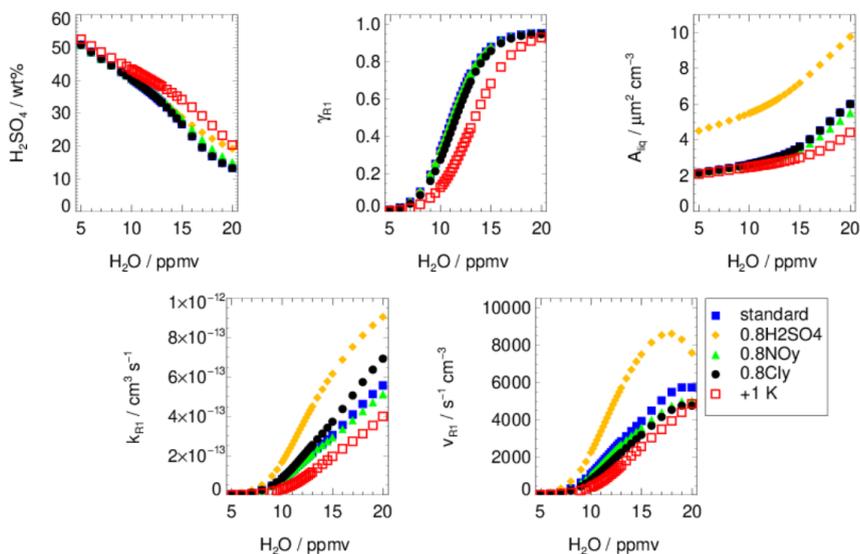
Figure 4.9: Dependence on water vapour of the H_2SO_4 wt-%, the γ-value $\gamma_{R\,21}$, the liquid surface area density A_{liq}, the rate coefficient $k_{R\,21}$ and the rate of the main heterogeneous chlorine activation reaction R 21 $v_{R\,21}$. Presented parameters correspond to the values after the first chemistry time step of the box-model simulation. Additionally the impact of an enhanced sulfate content (0.8 ppbv H_2SO_4, yellow), reduced NO_y (0.8 NO_y, green), reduced Cl_y (0.8 Cl_y, black) and enhanced temperatures (red) is shown. The standard case is shown as blue squares.

of R 24 ($CH_4 + Cl$) increases with an increasing water content (Fig. 4.6f). An increasing heterogeneous reaction rate (R 21) results in both a lower NO_x mixing ratio and more HCl converted into ClO_x. A higher ClO_x concentration causes a higher Cl mixing ratio and thus an increase in the rate of R 24 ($CH_4 + Cl$). Since both the rates of R 21 and R 24 increase, no significant net chlorine activation occurs. Around the water vapour threshold, the Cl-mixing ratio peaks (Fig. 4.6g), because less ClO is converted into Cl through

$$ClO + NO \rightarrow Cl + NO_2 \qquad\qquad (R\,37)$$

due to the decreasing NO_x mixing ratio. The lower Cl mixing ratio reduces the HCl formation in R 24 ($CH_4 + Cl$). Hence, the increasing heterogeneous reactivity $k_{R\,21}$ yields a higher rate of R 21 and in the same way it impedes R 24 by reducing the NO_x mixing ratio. As a consequence the rate of R 21 exceeds the rate of R 24 and a net chlorine activation takes place, leading to a reduction of HCl. At high water vapour mixing ration, the decline in both HCl and NO_x yields smaller rates of R 21 and R 24 and thus a peak of R 21 and R 24 (Fig. 4.6f). Hence, the increasing heterogeneous reactivity ($k_{R\,21}$) of R 21 with increasing water vapour mixing ratios destabilizes the balance between chlorine activation and deactivation by promoting the chlorine activation (due to an increasing rate of R 21) and impeding chlorine deactivation (due to a reduction of R 24). This yields heterogeneous chlorine activation to exceed gas phase HCl-formation in the water vapour threshold region.

For an enhanced sulfate content (Fig. 4.9, yellow diamonds), the particle surface area density (A_{liq}) is larger, leading to a stronger increase of the heterogeneous reactivity ($k_{R\,21}$) and hence a higher heterogeneous reaction rate $v_{R\,21}$ than in the standard case. Due to this higher heterogeneous reactivity (k_{R21}), the chlorine activation rate exceeds the chlorine deactivation at a lower water vapour mixing ratio and the net chlorine activation is reached at a lower water vapour threshold. A shift to higher temperatures (Fig. 4.9, red) yields almost no change in the surface area density (A_{liq}) but a reduced γ-value due to a higher H_2SO_4 fraction in the particles (H_2SO_4 wt%) and thus a lower heterogeneous reactivity ($k_{R\,21}$). The reduced reactivity causes the net chlorine activation to occur at a higher water vapour threshold.

In contrast, the shift of the threshold for simulations with only 80% of standard NO_y (0.8 NO_y, Fig. 4.9 green) or Cl_y (0.8 Cl_y, Fig. 4.9 black) can not be explained only by focussing on the heterogeneous reactivity ($k_{R\,21}$). In these cases, further effects on the balance between chlorine activation and chlorine deactivation have to be taken into account. The water vapour threshold in the 0.8 NO_y simulation (green triangles) is shifted to lower water vapour values due to a smaller Cl/ClO-ratio for lower NO_x concentrations (through reaction R 37). This causes a reduced HCl formation through R 24 ($CH_4 + Cl$) than in the standard case and thus impedes chlorine deactivation.

The reduced chlorine deactivation affects the balance between chlorine activation and deactivation in a way that the water vapour threshold in the $0.8\,NO_y$ case is lower than in the standard case.

In the $0.8\,Cl_y$ case (Fig. 4.9, black), the HCl and $ClONO_2$ mixing ratios are reduced. This leads to a lower chlorine activation rate $v_{R\,21}$ than in the standard case, despite of the slight higher heterogeneous reactivity ($k_{R\,21}$), which is due to the inverse dependence of $k_{R\,21}$ on the HCl concentration (Eq. 2). Reaction R 24 (Cl+CH$_4$) is less dependent on the Cl_y mixing ratio than reaction R 21 (HCl + $ClONO_2$). This promotes chlorine deactivation (R 24) in the balance between chlorine activation and deactivation and hence shifts the water vapour threshold to higher water vapour mixing ratios. Additionally caused by the lower rate of R 21 ($ClONO_2$ + HCl) for reduced Cl_y, the NO_x mixing ratio decreases more slowly. This enhances the rate of R 24 (CH$_4$ + Cl) compared with the standard case as well, because more NO_x yields a higher Cl/ClO-ratio.

In summary, the water vapour threshold is determined by the balance between chlorine activation and deactivation and is thus in a certain temperature range especially sensitive to the water dependence of the heterogeneous reactivity ($k_{R\,21}$) mainly described through the γ-value $\gamma_{R\,21}$ and the particle surface A_{liq}. These parameters are dependent on the present temperature and sulfate content. However, further parameters influencing this balance, such as the NO_y and Cl_y mixing ratio, have an impact on the water vapour threshold as well.

4.3.3   Temperature dependence

The water vapour threshold, which has to be exceeded for chlorine activation and stratospheric ozone loss to occur, is mainly dependent on the temperature. To illustrate the impact of both the temperature and the water vapour mixing ratio on stratospheric ozone, the relative ozone change occurring after a 7-day simulation, in which a constant temperature and water vapour concentration (with Cl_y and NO_y values of the standard case) are assumed (Fig. 4.10). In the left panel, ozone change as a function of temperature and water vapour is plotted for non-enhanced sulfate amounts. In the right panel, the relative ozone change is shown for $10\times$ standard sulfate to estimate a potential impact

of volcanic eruptions or sulfate geoengineering on stratospheric ozone. Since mixing of neighbouring air parcels is neglected in the box-model study, the relative ozone change calculated corresponds to the largest possible ozone change for the conditions assumed. A mixing of moist tropospheric air with dry stratospheric air is expected to reduce the water vapour mixing ratio during the time period of the 7-day trajectory and hence could stop ozone depletion before the end of the trajectory is reached. In addition to the relative ozone change, the threshold for chlorine activation is shown as a white line in both panels (Fig. 4.10). When temperature is held constant, this threshold corresponds to the water vapour threshold discussed above. Chlorine activation occurs at higher water mixing ratios and lower temperatures relative to the chlorine activation threshold plotted as a white line (Fig. 4.10). Here, chlorine is defined to be activated, if the ClO_x/Cl_y ratio exceeds 10%.

For climatological non-enhanced sulfate amounts (Fig. 4.10, left), the temperature has to fall below 203 K for chlorine activation to occur, even for high water vapour mixing ratios of 20 ppmv. Assuming the water vapour mixing ratio of 10.6 ppmv from the measurement, the temperature has to stay lower than ~199.5 K during the 7-day simulation to cause both chlorine activation and ozone destruction. For the simultaneous presence of high water vapour and low temperatures an ozone loss of 9% (max. 27 ppbv O_3) is found. This maximal ozone loss occurs for a range of low temperatures (~195–200 K) and enhanced water vapour mixing ratios (~10–20 ppmv), because of a similar time until chlorine activation occurs. If the temperatures are higher and water vapour mixing ratios lower than the chlorine activation threshold, the ozone mixing ratio increases around 3.5% (~10 ppbv O_3).

At enhanced sulfate conditions (Fig. 4.10, right), an ozone loss of max. 10% (30 ppmv O_3) occurs for low temperatures and high water vapour mixing ratios. For a water vapour mixing ratio of 20 ppmv the temperature has to fall below 205 K for ozone loss to occur. For the water vapour mixing ratio of the measurement (10.6 ppmv), temperatures have to be lower than ~201 K to cause chlorine activation. If the temperatures are very low (~195–200 K) and the water vapour is high (~10–20 ppmv) ozone loss is slightly reduced. This turnaround occurs, because at a high sulfate loading in combination with
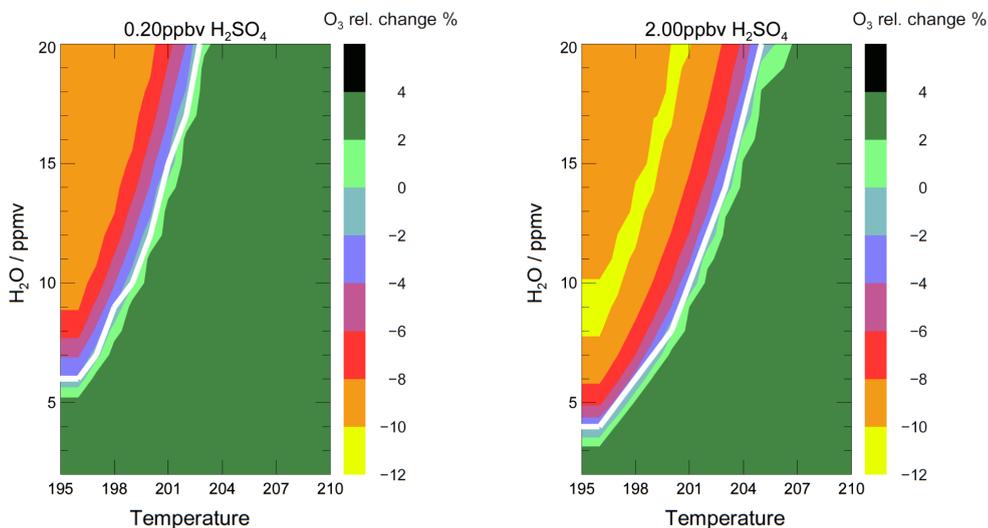
Figure 4.10: Relative ozone change, during 7-day simulations assuming constant temperatures, dependent on temperature and H_2O mixing ratio for climatological non enhanced (left) and enhanced (right) sulfate conditions. The white line corresponds to the water and temperature dependent chlorine activation threshold.

high water and low temperatures more HCl is taken up by condensed particles. This leads to less Cl_y in the gas phase and thus lower rates of catalytic ozone loss.

In summary, the combination of low temperatures, enhanced sulfate concentrations and high water vapour mixing ratios promotes an ozone decrease of up to $\sim$10% (corresponding to maximum -30 ppbv O_3). In comparison to the study of Anderson et al. (2012), the temperatures have to fall below 203 K (here) instead of 205 K (in Anderson et al. (2012)) for non enhanced sulfate conditions and below 205 K instead of 208 K (in Anderson et al. (2012)) for enhanced sulfate conditions and a water vapour mixing ratio of 20 ppmv for chlorine activation and thus ozone loss to occur. Anderson et al. (2012) were the first, who proposed this ozone loss mechanism to potentially occur in the mid-latitude lowermost stratosphere. However, the study of Anderson et al. (2012) assumes Cl_y and NO_y much larger than inferred from tracer-tracer correlations here. Hence, Anderson et al. (2012) found ozone loss in mid-latitudes at high water

vapour mixing ratios for temperatures 2 to 3 K higher than in the here performed simulations.

4.4 Case studies

Case studies are conducted to illustrate the sensitivities described above on ozone loss and to estimate the impact of realistic conditions and an upper boundary on the ozone loss process. In the "case based on observations", standard conditions and the measured water vapour mixing ratio of 10.6 ppmv are assumed using both the low sulfate content of the standard case and a slightly enhanced sulfate content, which represents the possible impact of volcanic eruptions or sulfate geoengineering conditions. As a kind of worst case study (upper boundary), the "Case of high Cl_y" is simulated using Cl_y and NO_y mixing ratios based on the study of Anderson et al. (2012), which uses Cl_y and NO_y much larger than inferred from tracer-tracer correlations (Table 4.1). In the "reduced Br_y case", standard conditions with a 50% reduced Br_y mixing ratio are assumed to test uncertainties in current observations of the stratospheric bromine burden. Additionally, the previously noted standard 7-day trajectory is extended to a 19-day trajectory to infer the dependence of ozone loss on the simulated time period.

4.4.1 Case based on observations

The simulation of the case based on observations during the SEAC[4]RS aircraft campaign corresponds to the most realistic case for today's chemical conditions. It is identical to that of the standard case but assumes the fixed water vapour mixing ratio of 10.6 ppmv observed on 8 August 2013. Although the water vapour threshold for the standard case is found to correspond to the measured water vapour value (10.6 ppmv), only minor chlorine activation due to R 21 ($ClONO_2 + HCl$) and no catalytic ozone loss cycles (e.g. based on ClO+BrO) can be observed in the simulation (Fig. 4.11, left). Chlorine activation requires temperatures lower than $\sim$199.5 K (see Fig. 4.10) for a water vapour mixing ratio of 10.6 ppmv. Such low temperatures are maintained in the realistic standard trajectory only for few hours and hence the maintenance of chlorine
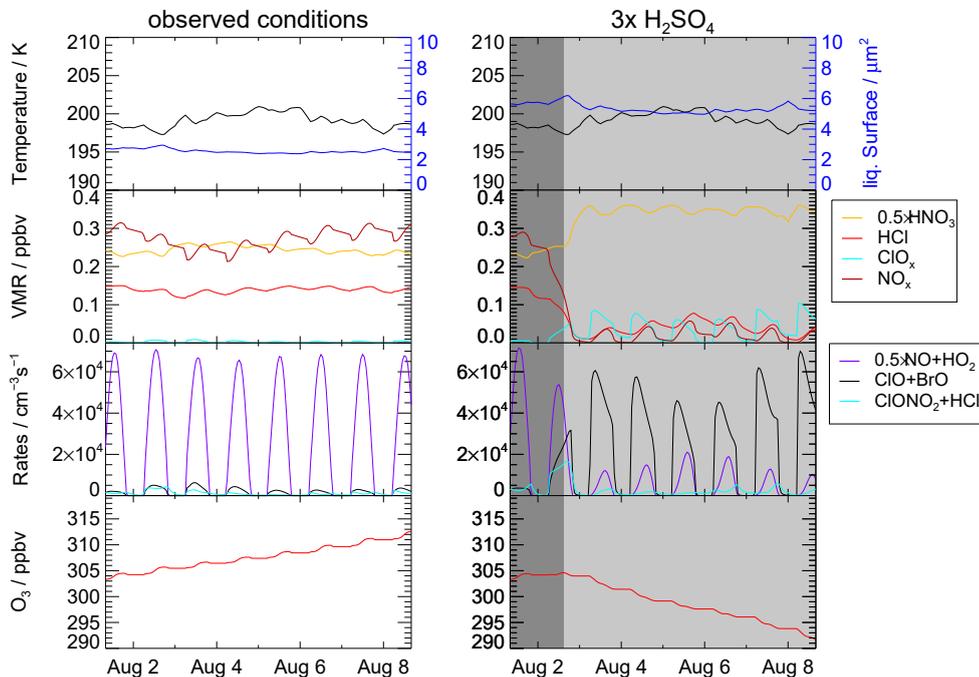
Figure 4.11: Left panels present the temperature, liquid surface area density, ozone mixing ratio, reaction rates of R 21 ($ClONO_2 + HCl$, cyan), R 17 (ClO+BrO, black) (as an example for ozone loss cycles), R 11 ($NO + HO_2$, violet) which limits ozone formation at low NO_x concentrations as well as volume mixing ratios of HCl (red), ClO_x (light blue), NO_x (black) and HNO_3 (scaled with 0.5) for the "Case based on observations" with 10.6 ppmv H_2O and 0.20 ppbv H_2SO_4. The panels on the right show the same quantities, but for enhanced sulfate conditions (0.60 ppbv H_2SO_4). The x-axis ticks refer to 00:00 local time (06:00 UTC) of that day.

activation likewise only lasts few hours. Instead, ozone is formed in this simulation. In comparison, the same simulation with 0.6 ppbv gas phase equivalent H_2SO_4 instead of 0.2 ppbv is conducted (Fig. 4.11, right). The enhanced sulfate content leads to a larger liquid surface area density and thus an increased heterogeneous reactivity. Hence, reaction R 21 occurs in the $3 \times H_2SO_4$ simulation significantly, leading to a slightly increasing ClO_x mixing ratio and a decrease of the NO_x mixing ratio. Both a reduced ozone formation in C3 (which is at decreased NO_x concentrations limited by R 11) and ozone loss cycles (e.g. cycle C5 based on the reaction ClO+BrO or cycles C6 and C8
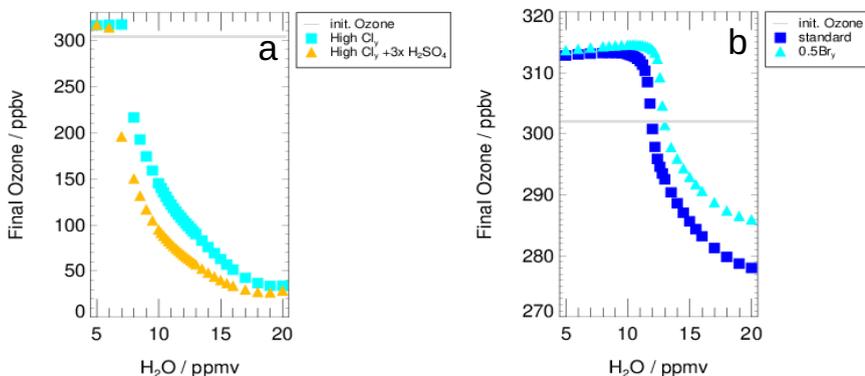
Figure 4.12: The water dependent final ozone value is shown for (a) the "Case of high Cl_y" (see Tab. 4.1 for NO_y and Cl_y initialisation) assuming background aerosol (light blue) and tripled H_2SO_4 (yellow) and (b) reduced Br_y (light blue, "Reduced Br_y case"). In panel (b) also final ozone of the standard case is shown (blue). Initial ozone is marked with a grey line. Note that the scales of the y-axes differ.

based on $ClO+HO_2$) can be observed, resulting in a reduction of ozone.

Using initial conditions, the trajectory corresponding to the SEAC[4]RS observations shows ozone loss with sulfate enhanced by a factor of 3. However, this is an unusually cold trajectory. A more common case with higher mean temperatures would require a higher sulfate content to enhance the heterogeneous reactivity that chlorine activation can occur. Under current chemical conditions in the lowermost stratosphere, it is most unlikely to get significant ozone loss by convectively injected water vapour in mid-latitudes.

4.4.2   Case of high Cl_y

Anderson et al. (2012) first proposed this ozone loss mechanism to potentially occur in the mid-latitude lowermost stratosphere. For conditions of substantially higher initial Cl_y and NO_y mixing ratios (see Tab. 4.1) than in the standard case, which are used in Anderson et al. (2012), a larger ozone loss up to 265 ppbv during the 7-day simulation is simulated (Fig. 4.12a). Since these high Cl_y conditions have been criticised in other studies (e.g. Schwartz et al., 2013; Homeyer et al., 2014) as being unrealistically high,

they are assumed here as a worst case scenario.

At high chlorine conditions, and for a high water vapour content (more than $\approx$18 ppmv), an almost complete ozone destruction with a final ozone value of less than 50 ppbv is simulated (Fig. 4.12a), which corresponds to parcel ozone loss of 85%. During the 3.5-day simulation in the study of Anderson et al. (2012), an ozone loss of 20% with respect to initial ozone occurs for 18 ppmv H_2O. This difference in relative ozone loss for similar conditions here and in the study of Anderson et al. (2012) is caused by a longer assumed ozone destruction period in the chemical simulation here. Since the Cl_y-mixing ratio is much higher than in the standard case, the catalytic ozone loss cycles are dominated by the ClO-Dimer cycle (C4). Assuming the measured water vapour content of 10.6 ppmv for high chlorine conditions would lead to an ozone depletion of 57% during the 7-day simulation. In comparison, in the standard case an ozone loss of 8% is reached when a high water vapour mixing ratio of 20 ppmv is assumed. However, even for the standard trajectory and a high chlorine content, a water vapour amount of 8 ppmv has to be exceeded to lead to any ozone reduction. This threshold shifts from 8 ppmv to 7 ppmv if stratospheric sulfate is tripled (Fig. 4.12a, yellow triangles).

4.4.3   Reduced Br_y Case

The mixing ratio of inorganic bromine (Br_y) has a high uncertainty in the lowermost stratosphere due to the influence of very short lived bromine containing substances. For example, during the CONTRAST field campaign (Jan.–Feb. 2014, in the western Pacific region), Koenig et al. (2017) observed a Br_y mixing ratio in the lower stratosphere of 5.6–7.3 pptv and the contribution of Br_y, which crosses the tropopause, was estimated to be 2.1±2.1 pptv (Wales et al., 2018). Navarro et al. (2017) found somewhat different bromine partitioning depending on the ozone, NO_2 and Cl_y concentrations, using very short lived bromine species observations in the eastern and western Pacific ocean. Because here the Br_y values are not based on measurements for this specific case modelled, the sensitivity is tested to a value that is half of the standard case. The impact of this Br_y reduction is illustrated in Fig. 4.12b.

Comparing the final ozone value for the 0.5 Br_y simulations (Fig. 4.12b, light blue

triangles) with those of the standard case (blue squares), a higher water vapour threshold and a reduced ozone loss of about 30% at high water vapour mixing ratios is simulated. The shift of the water vapour threshold is due to the impact of Br_y on the NO_2/NO-ratio. Due to the reaction

$$BrO + NO \ \rightarrow \ Br + NO_2, \tag{R 38}$$

 a reduced Br_y mixing ratio results in a smaller NO_2/NO-ratio and hence less $ClONO_2$ formation in R 30 ($ClO+NO_2$). Since $ClONO_2$ formation is essential for chlorine activation in R 21 ($ClONO_2+HCl$), reduced Br_y yields a lower chlorine activation rate (von Hobe et al., 2011) and thus a shift of the water vapour threshold to higher water vapour mixing ratios.

In the case of reduced Br_y, less ozone is destroyed comparing to the standard case. The ozone destruction in the ClO-BrO-cycle (C5) is reduced, while the rates of R 13 ($ClO+ClO$, determining cycle C4) and R 19 ($ClO+HO_2$, causing cycles C6, C7 and C8) are similar to those of the standard case (Fig. 4.5,e). This results in the reduced ozone destruction in the $0.5 \, Br_y$ case.

4.4.4   Extended time period

Since the occurrence of the ozone loss process analysed in this study is strongly dependent on a variety of parameters, the time period over which the ozone loss might occur is very uncertain. The impact of this time period on ozone loss is tested by extending the 7-day trajectory used in the sections above to span the entire period with temperatures low enough to maintain chlorine activation at 15 ppmv H_2O.

  The temperature, liquid surface area density as well as mixing ratios and reaction rates relevant for the analysed ozone loss mechanism are shown for the simulation with an extended time period (15 ppmv H_2O) in Fig. 4.13. The grey shaded area marks the section the standard trajectory accounts for. On 27 July 2013, the 19-day simulation starts at a temperature of 208 K, decreasing until 29 July 2013 to less than 200 K. The temperatures remain lower than 201 K until 11 August and increase to over 205 K on 14 August 2013.
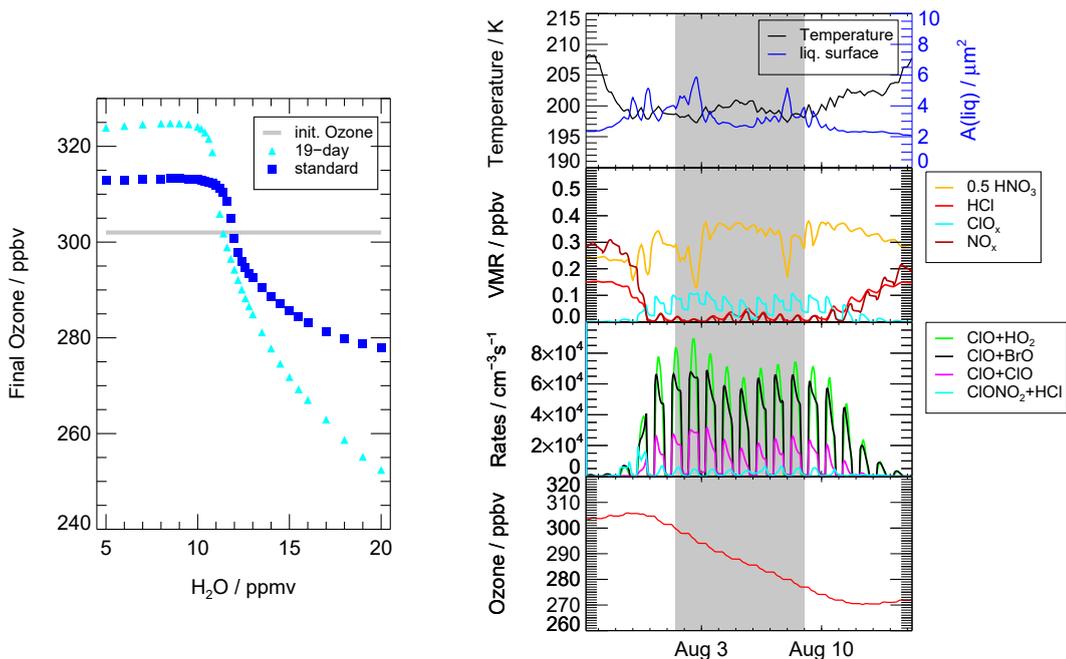
Figure 4.13: For the case with an extended time period (19-day simulation), the water dependent final ozone is shown (cyan, left). Further, the final ozone of the standard case is shown (blue). Initial ozone is marked with a grey line. The right panel shows the temperature, liquid surface area, the mixing ratio of ozone, HNO_3 (scaled by 0.5), HCl, ClO_x and NO_x and reaction rates of reactions essential for chlorine activation ($ClONO_2 + HCl$) and catalytic ozone loss cycles ($ClO+BrO$, $ClO+ClO$ and $ClO + HO_2$) for the 19-day simulation assuming 15 ppmv H_2O. The standard trajectory refers to the grey shaded section of the shown simulation. The x-axis ticks refer to 00:00 local time (06:00 UCT) of that day.

Assuming a water vapour mixing ratio of 15 ppmv, chlorine activation occurs on 30 July 2013, after the temperatures fall below 200 K (Fig. 4.13, right). The mixing ratio of NO_x remains low and ClO_x remains high until 11 August, when the heterogeneous reaction rate of R 21 ($ClONO_2 + HCl$) decreases due to higher temperatures. For this reason chlorine activation is not longer maintained. Thus, the time span holding a ClO_x mixing ratio high enough for the occurrence of catalytic ozone loss cycles comprises 14 days and ozone destruction stops on 12 August.

Because of the extended time period, the final ozone values assuming the enhanced water vapour mixing ratios for the longer trajectory (cyan triangles Fig. 4.13, left) are much lower than those of the standard 7-day simulation (blue squares). Additionally, more ozone is formed when using low water vapour concentrations. Comparing the water vapour threshold of the 7-day trajectory ($\sim$10.6 ppmv) and the 19-day simulation (10.2 ppmv), a shift to lower water vapour mixing ratios occurs in the 19-day trajectory. This shift is likely due to an extended time period with a temperature well below 200 K at the begin of this trajectory, which allows a chlorine activation to occur even for slightly lower water vapour amounts. Simulations along a trajectory starting on the same day as the 7-day trajectory, but finishing on 15 August, yield the same water vapour threshold as the 7-day simulation, indicating that the shift in the threshold shown in Fig. 4.13 is associated with the very cold conditions at the start of the 19-day simulation. Hence, the length of the chosen trajectory has no impact on the water vapour threshold, but does effect the final ozone.

4.5 Discussion of the results

Many uncertainties affect the assessment of the extent of ozone loss that occurs in the lowermost stratosphere at mid-latitudes under enhanced water vapour conditions. The number and depth of convective overshooting events as well as the area and duration affected by enhanced water vapour mixing ratios is a subject of recent research (e.g. Homeyer et al., 2014; Smith et al., 2017). The mixing ratios of important trace gases (O_3, Cl_y, Br_y, NO_y) in overshooting plumes and the probability that water vapour

mixing ratios high enough for chlorine activation to meet temperatures low enough is a matter of debate (e.g. Schwartz et al., 2013; Homeyer et al., 2014).

The ozone loss mechanism investigated here requires the occurrence of the heterogeneous reaction R 21 ($ClONO_2 + HCl$), which leads to enhanced ClO_x and reduced NO_x mixing ratios and thus maintains effective catalytic ozone loss cycles. Clapp and Anderson (2019) found the rate of reaction R 21 to increase for a water vapour mixing ratio of 7–15 ppmv for conditions in the mid-latitude lowermost stratosphere and a temperature of 200.3 K. This finding is similar to the result of this thesis, where the reaction rate of R 21 is found to mainly increase between 8 and 18 ppmv H_2O for standard conditions. Enhanced ClO and reduced NO concentrations were observed by Keim et al. (1996) and Thornton et al. (2007) close to the mid-latitude tropopause under conditions with both enhanced water vapour and enhanced concentrations of condensation nuclei, such as sulfate particles. These observations were attributed to the occurrence of the heterogeneous reactions R 21 ($ClONO_2+HCl$) and R 23 ($ClONO_2 + H_2O$) (Thornton et al., 2007; Keim et al., 1996). For the temperature and the water vapour range observed in the studies of Keim et al. (1996) (15 ppmv H_2O, ∼207 K) and Thornton et al. (2007) (15–22 ppmv H_2O, ∼213–215 K), a heterogeneous chlorine activation would not occur in the box-model simulation conducted here, not even in a sensitivity simulation assuming a high sulfate gas phase equivalent of 7.5 ppbv H_2SO_4 (not shown).

At low temperatures ($\lesssim$196 K), heterogeneous chlorine activation may occur in the tropical stratosphere (e.g. Solomon et al., 2016b). Von Hobe et al. (2011) observed enhanced ClO mixing ratios during aircraft campaigns over Australia (SCOUT-O_3, 2005) and Brazil (TROCCINOX, 2005) in combination with low temperatures and the occurrence of cirrus clouds. They further found a threshold in the ozone mixing ratio, which has to be exceeded for chlorine activation to occur. Hence, the water vapour threshold discussed here is expected to depend on the ozone mixing ratio, as well. Moreover a potential occurrence of ice particles in the lowermost mid-latitude stratosphere (Spang et al., 2015) might affect the water vapour threshold due to a different heterogeneous reactivity on ice than on liquid particles (Solomon, 1999).

Analysing the balance between chlorine activation and deactivation von Hobe et al.

(2011) showed an increase of the chlorine activation rate (R 21) with a higher ClO, BrO and O_3 mixing ratio. Thus, once started, reaction R 21 accelerates due to higher ClO-mixing ratios subsequently yielding a fast conversion of NO_x into HNO_3 (von Hobe et al., 2011), comparable to the NO_y repartitioning found in the study of this thesis. Such a repartitioning was likewise found in the box-model study of Clapp and Anderson (2019) investigating the impact of convective overshooting events transporting water vapour to the mid-latitude lowermost stratosphere on ozone chemistry and the HNO_3 abundance. Clapp and Anderson (2019) further considered the potential of denitrification in the mid-latitude lowermost stratosphere to promote heterogeneous chlorine activation.

An enhanced sulfate content increases the heterogeneous reaction rate caused by an enlarged liquid surface. Due to this relation, an impact of stratospheric albedo modification (by applying sulfate geoengineering) on the ozone loss process proposed by Anderson et al. (2012) was discussed (Dykema et al., 2014). Applying sulfate geoengineering would also affect the temperature in the lowermost stratosphere and would change the lower stratospheric dynamics (Visioni et al., 2017b). It would also affect large scale latitudinal mixing of atmospheric tracers in the lower branch of the Brewer-Dobson-Circulation and would result in a different chemical composition of the lower mid-latitude stratosphere (Visioni et al., 2017b). Varying the sulfate content here showed that for temperatures and water vapour conditions of the case based on observations, a moderate enhancement of $3 \times H_2SO_4$ is sufficient to yield ozone depletion. Considering the temperature and water vapour dependence of the chlorine activation threshold (Fig. 4.10, white line), a tenfold enhancement of stratospheric sulfate yields a shift of chlorine activation to slightly lower water vapour mixing ratios and higher temperatures. However, even for enhanced sulfate and a water vapour mixing ratio of 20 ppmv, the temperature has to fall below 205 K for chlorine activation (and hence ozone depletion) to occur at the assumed Cl_y and NO_y conditions of the standard case.

After the chlorine activation step, catalytic ozone loss cycles can occur: the ClO-Dimer cycle C4, the ClO-BrO-cycle C5 and cycles subsequent to R 19 (ClO + HO_2, C6–C8). Cycle C6 was reported to have an impact on stratospheric ozone in mid-latitudes in

previous studies (e.g. Johnson et al., 1995; Kovalenko et al., 2007; Ward and Rowley, 2016). Here, C6 is found to be the dominate cycle based on R 19 under standard conditions. Nevertheless, simulating the "0.5 Br$_y$" and "high Cl$_y$" case has shown that the relevance of the ClO-Dimer-cycle C4 and the ClO-BrO-cycle C5 depends on the assumed initial values of Cl$_y$ and Br$_y$. Lowermost stratospheric Br$_y$ mixing ratios are strongly influenced by the abundance of very short living bromine compounds penetrating into the stratosphere. However, the impact very short living bromine compounds have on stratospheric ozone was found to be correlated with the overall stratospheric Cl$_y$ and Br$_y$ abundance, which results from anthropogenic long living chlorine and bromine compounds in the stratosphere (Barrera et al., 2020).

Anderson and Clapp (2018) discussed the occurrence of the ClO-Dimer cycle C4 and the ClO-BrO-cycle C5 dependent on the water vapour mixing ratio, the Cl$_y$ mixing ratio and temperature. They illustrated a significant increase in the rate of R 13 (ClO+ClO) and R 17 (ClO+BrO) if the combination of enhanced water vapour and low temperatures is sufficient for chlorine activation to occur. If chlorine activation occurs in their model study, a higher Cl$_y$ mixing ratio yields higher catalytic ozone loss rates (R 13, R 17). Their finding regarding the effect of temperature, water vapour and chlorine on the ozone loss process is consistent with the results found here. The occurrence of net chlorine activation is determined by temperature and water vapour mixing ratio, while the Cl$_y$ mixing ratio controls how much ozone is destroyed.

A measure for the effect of temperature and water vapour on stratospheric chlorine activation and ozone chemistry is the temperature and water vapour dependent chlorine activation threshold (Fig. 4.10, white line). Anderson et al. (2012) reported that lower temperatures than 205 K are necessary for chlorine activation to occur at a water vapour mixing ratio of 20 ppmv and a climatological non enhanced sulfate content. In comparison, assuming standard conditions for Cl$_y$ and NO$_y$ but a constant temperature here, temperatures lower than 203 K are required for ozone loss to occur at similar H$_2$O and sulfate concentrations.

The standard trajectory is chosen here to hold conditions most likely for chlorine activation based on SEAC[4]RS measurements. For the temperature range of this trajectory

and the measured water vapour mixing ratio (10.6 ppmv) no significant ozone depletion occurs. Hence, for all SEAC[4]RS and MACPEX trajectories calculated (not only the shown examples), no trajectory produced ozone loss. A further requirement for the occurrence of chlorine activation is the maintenance of the conditions, which yield chlorine activation, during the entire time of chlorine activation. Assuming standard conditions and a water vapour mixing ratio of 20 ppmv, chlorine activation takes 5 hours. However for a water vapour content close to the water vapour threshold, low temperatures and enhanced water vapour mixing ratios have to be maintained 24–36 hours for chlorine activation to have an impact on stratospheric ozone chemistry. For the occurrence of ozone depletion, temperatures have also to remain low and water vapour mixing ratios high after the chlorine activation step.

The maximum ozone depletion at standard conditions occurs here for a water vapour mixing ratio of 20 ppmv. At 20 ppmv H_2O, 8% of initial ozone are destroyed in the 7-day simulation, which is 11% lower than the final ozone reached under atmospheric background conditions assuming 5 ppmv H_2O. For similar conditions (200.3 K, 112.4 hPa, 20 ppmv H_2O), Clapp and Anderson (2019) simulated an ozone loss of 6.5% in a 5-day box-model simulation. For the 19-day simulation here, assuming 20 ppmv H_2O, the final ozone is 22% reduced compared to the 19-day simulation assuming 5 ppmv H_2O. Anderson and Clapp (2018) calculated a similar ozone reduction of 17% in a 14-day simulation and the same potential temperature range of 380 K assuming 20 ppmv H_2O and somewhat higer Cl_y ($\sim$0.2 ppbv) than as used here in the realistic case. In contrast, assuming the high Cl_y and NO_y mixing ratios employed by Anderson et al. (2012) in the case of high Cl_y would lead to an ozone loss of 85% (265 ppbv) during the 7-day simulation. This ozone loss calculated here would occur in the lower stratosphere.

Borrmann et al. (1996, 1997) and Solomon et al. (1997) conducted a study about the impact of cirrus clouds on chlorine activation and ozone chemistry in the mid-latitudes lowermost stratosphere. They found a significant impact of heterogeneous processes occurring on cirrus clouds for ozone chemistry of the lowermost stratosphere but a minor effect for column ozone. Schoeberl et al. (2020) found a correlation between elevated lowermost stratospheric water vapour mixing ratios and a reduced column

ozone in the region of the NAM. However, this correlation was shown to be related to the elevation of the monsoonal tropopause and no evidence for significant heterogeneous chlorine activation causing ozone loss was found. As a result from heterogeneous chlorine activation over North America, Anderson and Clapp (2018) calculated a fractional loss in the total ozone column of 0.24–0.27% assuming a full Cl_y profile in the altitude range of 12–18 km with a constant water vapour mixing ratio of 20 ppmv and the mixing ratio of Cl_y somewhat higher (~ 0.2 ppbv at a potential temperature of 380 K) than in the standard case here. However, the simulations here and of Anderson and Clapp (2018) assume a constant high water vapour mixing ratio and neglect mixing with the stratospheric background, which is characterized by much lower water vapour mixing ratios and subsequent dilution of convective uplifted air masses. Ozone loss would only occur in the specific volume of stratospheric air, that is directly affected by the convectively injected additional water. Hence, the ozone loss presented here corresponds to the maximal possible ozone loss for rather realistic convective overshooting conditions.

4.6   Summary

In this chapter of the thesis, an ozone loss mechanism at mid-latitudes in the lower stratosphere occurring under enhanced water vapour conditions is investigated as well as the sensitivity of this ozone loss mechanism to a variety of conditions. A CLaMS box-model study is conducted including a standard assumption and a variety of sensitivity cases regarding the chemical initialisation, temperatures and the duration of the simulated period. The assumed standard conditions (155.7 pptv Cl_y, 728.8 pptv NO_y, 197–202 K and an H_2SO_4 gas phase equivalent of 0.20 ppbv) are determined based on measurements in an H_2O environment showing strongly enhanced H_2O values compared to the stratospheric background during the SEAC[4]RS aircraft campaign in Texas 2013. The analysed ozone loss mechanism consists of two phases: The first step is chlorine activation due to the heterogeneous reaction $ClONO_2 + HCl$ (R 21), which leads to both an increase of ClO_x and a decrease of NO_x. In the second phase, when chlorine is

activated, enhanced ClO_x mixing ratios result in catalytic ozone loss cycles. Besides the ClO-Dimer-cycle C4 and the ClO-BrO-cycle C5, three ozone loss cycles (C6–C8) based on the reaction $ClO+HO_2$ (R 19) have to be taken into account. The relevance of the different ozone loss cycles for ozone destruction depends on water vapour, Cl_y and Br_y mixing ratios. Reduced NO_x mixing ratios yield a decreasing chemical net ozone formation in the "ozone smog cycle" C3. This reduced ozone formation at high water vapour mixing ratios in the box-model simulation contributes around 20% of the ozone reduction at high water vapour mixing ratios dominated by catalytic ozone loss cycles. Furthermore a detailed analysis of chemical processes revealed the occurrence of pathways, which maintain high ClO_x and low NO_x mixing ratios after the chlorine activation step but do not destroy ozone, similar to HCl-null-cycles in the lower stratosphere in Antarctic early spring (Müller et al., 2018).

Focussing on the dependence of chlorine activation on temperature and the water vapour mixing ratio, it is found that the temperature has to fall below 203 K for chlorine activation to occur at a water vapour mixing ratio of 20 ppmv and Cl_y and NO_y for the standard case here. Testing the water vapour dependence of ozone loss along a realistic trajectory that experienced very low temperatures between 197 and 202 K, a water vapour threshold of 10.6 ppmv H_2O is observed, which has to be exceeded for chlorine activation to occur. Ozone loss occurs in these simulations for at least 12 ppmv H_2O. For the assumed standard conditions, a maximum ozone loss of 9% (27 ppbv) is calculated for a water vapour mixing ratio of 20 ppmv. In contrast, a simulation assuming the observed conditions (10.6 ppmv H_2O) yielded ozone formation; but a tripling of background sulfate gas phase equivalent (as it can be reached under sulfate geoengineering conditions or volcanic eruptions) is sufficient for a slight ozone loss to occur under these unusually cold conditions. Simulating a high Cl_y case assuming initial Cl_y and NO_y based on the study of Anderson et al. (2012) results in both a lower water vapour threshold of $\sim$8 ppmv and a larger parcel ozone depletion of 85% (265 ppbv) at high water vapour mixing ratios. The model runs described here assume an air parcel moving along the trajectory, which does not mix with neighbouring air masses. In the case of water, mixing would likely reduce the concentration. Because

mixing is neglected, the runs discussed here are likely an extreme case, and the ozone loss simulated provides an upper bound.

Considering the duration for which low temperatures and high water vapour mixing ratios have to be maintained to activate chlorine and deplete stratospheric ozone, a chlorine activation time of 24 to 36 hours is calculated when the water vapour abundance is close to the water vapour threshold and of 5 h assuming 20 ppmv H_2O. The water vapour threshold depends strongly on a change in temperature and sulfate content as well as on Cl_y, NO_y and Br_y mixing ratios. The dependence of the water vapour threshold is explained here by focussing on the water dependence of the heterogeneous reactivity (R 21) and the balance between heterogeneous chlorine activation (R 21, $ClONO_2 + HCl$) and gas phase chlorine deactivation (R 24, $Cl + CH_4$).

The ozone loss mechanism is investigated here by conducting box-model simulations along a trajectory, which is calculated based on aircraft measurements of enhanced water vapour. Sensitivity and case studies, which cover a range of uncertainties, illustrate the impact of the Cl_y, NO_y, Br_y and H_2O mixing ratios, the temperature, the sulfate gas equivalent and the duration of the simulated period on the ozone loss process. While the conditions for chlorine activation to occur are mainly determined by the temperature, water vapour mixing ratio and sulfate content, the intensity of ozone loss depends on Cl_y, NO_y, Br_y and the duration of the time period, for which a chlorine activation can be maintained. The comprehensive sensitivity studies are a basis to assess the impact of enhanced water vapour mixing ratios in the lower mid-latitude stratosphere on ozone under sulfate geoengineering conditions and in a changing climate. However, for the conditions observed in today's atmosphere during SEAC[4]RS (in particularly H_2O=10.6 ppmv), not any ozone depletion is simulated leading to the conclusion that the occurrence of heterogeneous chlorine activation causing catalytic ozone destruction is unlikely for the conditions in the mid-latitude lowermost stratosphere during summertime in our days. How relevant this process will be for future conditions considering climate change as well as the application of sulfate geoengineering is investigated in the next chapter.

Chapter 5

Potential for future mid-latitude ozone loss in the lowermost stratosphere

The analysis of the ozone loss mechanism in the mid-latitude lower stratosphere (Chapter 4) showed that heterogeneous chlorine activation as the key step of ozone destruction is favoured by high water vapour mixing ratios, low temperatures and an enhanced sulfate abundance. However, from the results in Chapter 4 it can be concluded that chlorine activation occurs very unlikely today in the mid-latitude lowermost stratosphere during summertime. In this chapter, the focus is on the question whether heterogeneous chlorine activation and thus ozone loss similar to that known from polar regions likely occurs in future in the mid-latitude lowermost stratosphere.

Two future scenarios are considered: a climate change future scenario and a future scenario, where sulfate geoengineering is applied. Therefore, the GLENS model results (Sec. 3.3) are compared with chlorine activation thresholds calculated based on CLaMS box-model simulations (Sec. 3.2). These chlorine activation thresholds mark the boundary in water vapour and temperature between conditions which do and do not lead to heterogeneous chlorine activation (see Section 4.3.3). In addition to the likelihood, the impact of the ozone loss mechanism analysed before (Chapter 4) on mid-latitude ozone today and in future is estimated.

In this chapter, first the selection of GLENS results for the mid-latitude lowermost stratosphere is described as well as the setup of CLaMS box-model simulations, which are initialized based on these selected GLENS results (Sec. 5.1). Furthermore, the temperatures and the chemical composition of the lowermost stratosphere in GLENS today and in future are discussed and compared to airborne measurements (Sec. 5.2). The likelihood for the occurrence of chlorine activation is determined in Sec. 5.3, comparing the conditions present in the GLENS results with calculated chlorine activation thresholds using CLaMS. An upper boundary for the impact of this ozone loss process on mid-latitude ozone is deduced, additionally investigating the assumption of $2\,\mathrm{K}$ lower temperatures in the lowermost stratosphere.

The content of this chapter is in review at the Journal Atmospheric Chemistry and Physics and this chapter follows closely this publication:

Robrecht, S., Vogel, B., Tilmes, S., and Müller, R.: Potential of future stratospheric ozone loss in the mid-latitudes under global warming and sulfate geoengineering, Atmos. Chem. Phys., https://doi.org/10.5194/acp-21-2427-2021, 2021.

5.1   Setup of Simulations

The GLENS results are used here as a data set representing the conditions in the early (2010–2020), mid (2040–2050) and late (2090–2100) 21st century. GLENS is introduced in Section 3.3 while the focus here is on the selection of GLENS data in the mixing layer between tropospheric and stratospheric air in the lowermost stratosphere above central North America (see Sec. 2.2.1). Air masses within the mixing layer are characterised by relatively high H_2O mixing ratios from the troposphere compared to typically low stratospheric water vapour amounts and by O_3 and Cl_y higher than usually found in the upper troposphere from mixing with stratospheric air. Furthermore, the temperatures are low due to the location close to the thermal troposphere. Hence, the conditions prevailing in the lowermost stratospheric mixing layer are most likely for heterogeneous chlorine activation to occur and thus is in the focus of this study.

GLENS results in the selected mixing layer are used for initializing CLaMS box-model simulations. Further, the ozone change and the chlorine activation thresholds calculated from CLaMS simulations are compared with the conditions prevailing in the GLENS mixing layer. In this way, the sensitivity of chlorine activation thresholds to a variety of conditions can be demonstrated and the amount of ozone loss caused by chlorine activation can be calculated. This would not be possible, if only GLENS results were used, because of the complexity and the low time resolution of the global climate simulation (see Chapter 3).

5.1.1 GLENS data selection

GLENS (Sec. 3.3) provides a comprehensive global data set assuming two different future scenarios (climate change and application of geoengineering) covering the years 2010–2100. The GLENS study comprises three ensemble members from the year 2010 to the end of the 21st century following the RCP8.5 climate change scenario. Since only the first of these simulations completed until 2099, the first of these ensemble members is used here to investigate the likelihood for lowermost stratospheric ozone destruction. Furthermore, the first of twenty ensemble members of the geoengineering scenario comprising the years 2020–2099 is chosen. In this ensemble member, the geoengineering feedback mechanism starts stratospheric sulfate injections based on the setup of conditions in the year 2020 of the selected climate change run. Here, only specific decades and a specific region – namely air masses in the lowermost stratosphere above central North America in the early, mid and late 21st century – are considered using the 10 day instantaneous GLENS output.

For conditions of the early 21st century, the control-run for the years 2010–2020 is used. For a future with climate change following the RCP8.5 scenario, the years 2040–2050 (mid of this century) and 2090-2099 (end of this century) of the same model-run are used. The same years are considered for the geoengineering scenario (GLENS Feedback simulations). This in total five considered cases are referred to as C2010 for today's conditions (2010–2020) and C2040 (2040–2050) as well as C2090 (2090–2100) for the climate change scenario. The geoengineering cases are named F2040 and F2090 for the

Table 5.1: Denotation of considered cases.

Case	future scenario	Years
C2010	N/A	2010–2020
C2040	Climate Change following the RCP8.5 emission pathway	2040–2050
C2090	Climate Change following the RCP8.5 emission pathway	2090–2100
F2040	sulfate geoengineering	2040–2050
F2090	sulfate geoengineering	2090–2100

mid and the end of the 21st century, respectively. An overview on the considered cases
is given in Tab. 5.1.

GLENS results are selected for a latitude range of $30.6 - 49.5°$N and a longitude
range of $72.25 - 124.75°$W (grey marked in Fig. 5.1, left). Since the ozone loss process
focused on in this study is expected to occur most likely in summer, only the months
June, July and August are considered. As shown in Fig 5.1 (right), the tropopause
altitude varies depending on latitude and the considered case. Since the tropopause
altitude varies significantly above central North America, the latitude range is divided
into four bins (30–35°N, 35–40°N, 40–44°N and 44–49°N), but here the focus is on
southernmost latitude band (30–35°) with a more likely subtropical character of the
chemical composition and on the northernmost latitude band (44–49°N) representing
the chemical composition of the extra-tropics around the tropopause.

This study focuses on the mixing layer between tropospheric and stratospheric air
located in the lowermost stratosphere above central North America (blue illustrated
in Fig. 5.1, left), because it shows conditions most likely for heterogeneous chlorine
activation to occur. Since the tropopause altitude and thus the altitude range of the
mixing layer varies for different latitudes and future scenarios, the selected altitude
range for air masses in the lowermost stratospheric mixing layer is determined in a way
that it may vary in all considered cases. The lower boundary of the data selected is
chosen to be the thermal tropopause calculated by the WMO definition (see Sec. 2.1)
within GLENS. The upper boundary is determined based on the decrease of tropospheric
trace gas mixing ratios above the tropopause (Sec. 2.2.1). Here, air parcels are assumed
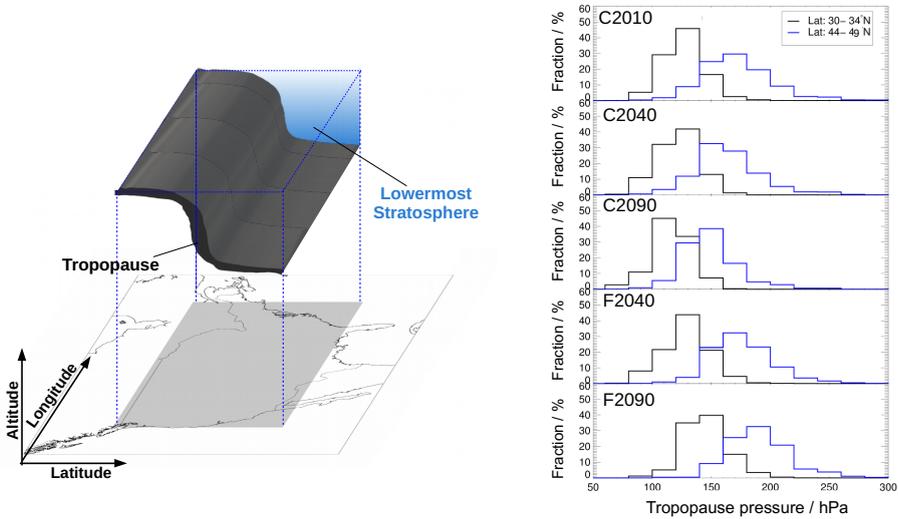
Figure 5.1: Schematic overview on the selected data region over North America (left). The position of the tropopause over central North America in summer is illustrated in black and the mixing layer is directly located above the tropopause in the lowermost stratosphere (blue). The right panel presents the tropopause pressure deduced from GLENS in this region depending on the latitude range and all considered cases (see Tab. 5.1).

to correspond to the mixing layer if they are located above the thermal tropopause (to separate tropospheric air masses) and show more than 35 ppbv of the artificial tropospheric trace gas E90 (to separate the mixing layer from the stratospheric air masses).

The artificial passive tracer E90 is released in GLENS globally with a lifetime of 90 days, a mixing ratio of ∼90 ppbv at the tropopause and a strong decrease in the lowermost stratosphere (Abalos et al., 2017). Since the E90-tracer is emitted continuously throughout the GLENS simulations, it is independent of possible changes in the emission rates of other tropospheric trace gases and therefore a good marker for the amount of tropospheric air in the considered air mass.

5.1.2   CLaMS simulations

Based on the selected GLENS data in the mixing layer, box-model simulations with the
CLaMS model (see Sec. 3.2) are performed to calculate chlorine activation thresholds,
which discriminate water vapour and temperature conditions causing heterogeneous
chlorine activation from those not causing chlorine activation. Comparing these chlorine
activation thresholds and the frequency distribution of GLENS data in water vapour
and temperature, the likelihood for heterogeneous chlorine activation to occur in the
mid-latitude mixing layer will be determined later in this thesis (see Sec. 5.3.2).

Before calculating activation thresholds with the CLaMS model, considered GLENS
results are divided in different latitude regions, pressure levels and ozone mixing ratios
as shown in Tab. 5.2. Any combination of latitude, pressure and ozone range is referred
to as a data group. The pressure levels are chosen based on the vertical levels used in
GLENS. In addition, ozone represents whether the considered air masses have a more
tropospheric (low ozone) or a more stratospheric character (high ozone).

Stratospheric chemistry is simulated for each data group along artificial 10-day trajec-
tories. The trajectories are located at a specific point in the stratosphere determined
as 102.5°W (middle longitude over the considered longitude range) and the middle
pressure and latitude of the specific data group (e.g. 32.5°N for the latitude range
30–35°N and 80 hPa for the pressure range of 70–90 hPa). As chemical initialization
for the CLaMS box-model, the median mixing ratio in a data group is taken of each
trace gas from GLENS. Heterogeneous chemistry is only considered here to take place
on liquid particles to ensure a comparability to the study of Anderson et al. (2012).
Further, only a very low fraction of GLENS data points shows conditions cold enough
for the formation of ice particles. As initialization for liquid particles, the particle
number density and the gas phase equivalent of H_2SO_4 is needed, taken from monthly
GLENS data as the median of a data group.

Since the chlorine activation threshold is determined by the water vapour mixing ratio
and the temperature, for calculating the chlorine activation threshold multiple simula-
tions are conducted for a data group scanning a variety of water vapour mixing ratios
and temperatures. Thus, for each of the five cases (see Tab. 5.1) and each data group

Table 5.2: Overview on the latitude, pressure, ozone, water vapour and temperature ranges, for which CLaMS simulations are conducted. Each combination of latitude, pressure and ozone range is summarized in a data group resulting in 100 different data groups. For a better overview in this paper, the pressure ranges are allocated to a pressure level.

Latitude / °N	30–35	35–40	40–44	44–49	
	subtropical lat. range			extra-tropical lat. range	
Pressure range / hPa	70–90	90–110	110–130	130–150	150–300
Pressure level	80 hPa	100 hPa	120 hPa	140 hPa	160 hPa
O_3 / ppbv	150–250	250–350	350–450	450–550	550–650
H_2O / ppmv	4–30	in steps of 1 ppmv			
Temperature / K	195–230	in steps of 1 K			

(Tab. 5.2), chemical simulations are conducted assuming constant water vapour varying from 4–30 ppmv in steps of 1 ppmv and a constant temperature varying from 195–230 K in 1 K steps resulting in a total of 455,000 box-model simulations.

Hereafter, instead of pressure ranges the allocated pressure level as given in Tab. 5.2 is used in the text. Further, the latitude region of 30–35°N is referred to as the subtropical latitude region and the latitude range of 44–49°N to as the extra-tropical latitude range.

Calculation of chlorine activation thresholds

Chlorine activation thresholds are calculated for each data group. Therefore, the water vapour and temperature conditions causing chlorine activation within a simulation are identified. Chlorine activation is assumed to have occurred, if ClO_x contributes 10% of Cl_y within the first 5 days of a CLaMS simulation. For each water vapour value, the maximum temperature at which chlorine activation occurs is determined to be the temperature threshold for heterogeneous chlorine activation. The array of this temperature thresholds depending each on an allocated water vapour mixing ratio, defines the chlorine activation threshold for the considered latitude, pressure and ozone range.

5.2   Analysing the GLENS mixing layer above central North America

The selected GLENS results are used as a data set representing the conditions and chemical composition in the mixing layer in the North American lowermost stratosphere in summer for all considered cases for future and today's conditions. In this section the reliability of the GLENS mixing layer selection is analysed as well as the change of specific trace gas mixing ratios in the considered future scenarios.

5.2.1   Comparing the GLENS mixing layer today with measurements

The reliability of selecting the mixing layer in the GLENS data set for the C2010 case is analysed by comparing the GLENS mixing layer for the latitude range 30–35°N with the mixing layer derived from SEAC^{4}RS ER2-aircraft measurements in August and September 2013 (see Sec. 4.1.1). Since one aim of SEAC^{4}RS was to investigate the impact of deep convective clouds on the water vapour content in the lowermost stratosphere (Toon et al., 2016), the SEAC^{4}RS measurements represent moist and cold conditions especially likely for heterogeneous chlorine activation to occur. Here, SEAC^{4}RS trace gas measurements are used for CO (Harvard University Picarro Cavity Ring down Spectrometer (HUPCRS,) Werner et al., 2017), O_3 (National Oceanic and Atmospheric Administration (NOAA) UAS O_3 instrument, Gao et al., 2012) and water vapour (Harvard Lyman-α photo fragment fluorescence hygrometer (HWV), Weinstock et al., 2009). Since GLENS is performed with a global model, the GLENS data comprise a broader range in space (regarding altitude and area) than SEAC^{4}RS aircraft measurements, which were locally taken up to an altitude of 20 km. Hence, GLENS and SEAC^{4}RS air masses have a different spatial distribution in the lowermost stratosphere above North America, potentially causing a difference between SEAC^{4}RS
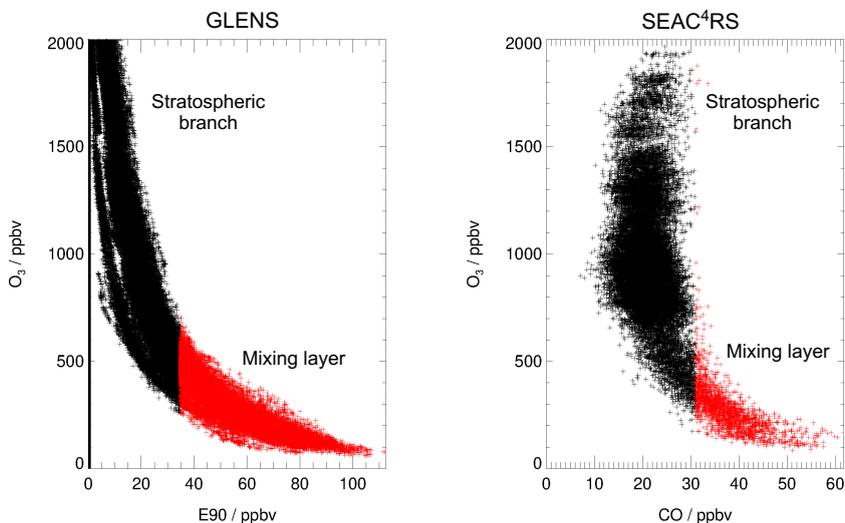
Figure 5.2: Tracer-tracer correlations for GLENS results in a latitude range from
30–35°N (left) and SEAC[4]RS measurements (right) consist of a stratospheric branch
(black) and of the mixing layer between stratospheric and tropospheric air masses (red).
The mixing layer is determined to be located above the tropopause and holding more
than 35 ppbv E90 in GLENS and more than 31 ppbv CO in SEAC[4]RS measurements.

and GLENS data distributions.

The mixing layer between stratospheric and tropospheric air masses in the SEAC[4]RS
measurements is assumed to be formed out of measurements above the tropopause with
a CO mixing ratio of more than 31 ppbv. This CO-boundary is selected to allow an
O_3-range similar to that of the GLENS mixing layer (up to $\sim$750 ppbv) and agrees
with observations in the study of Pan et al. (2004), where mixed air masses between
troposphere and stratosphere were described to hold usually more than $\sim$30 ppbv CO.
In Fig. 5.2, the trace gas correlation between a tropospheric and a stratospheric tracer
(as introduced in Sec. 2.2.1) in shown for GLENS (left) and SEAC[4]RS (right) data. The
mixing layer is marked in red while the stratospheric branch is shown in black. Air in
the GLENS mixing layer is separated from tropospheric air by being located above the
tropopause and from stratospheric air by holding more than 35 ppbv of the E90 tracer.
In the mixing layer deduced from SEAC[4]RS measurements, considered air masses lay
above the tropopause as well and are separated here from the stratospheric branch by
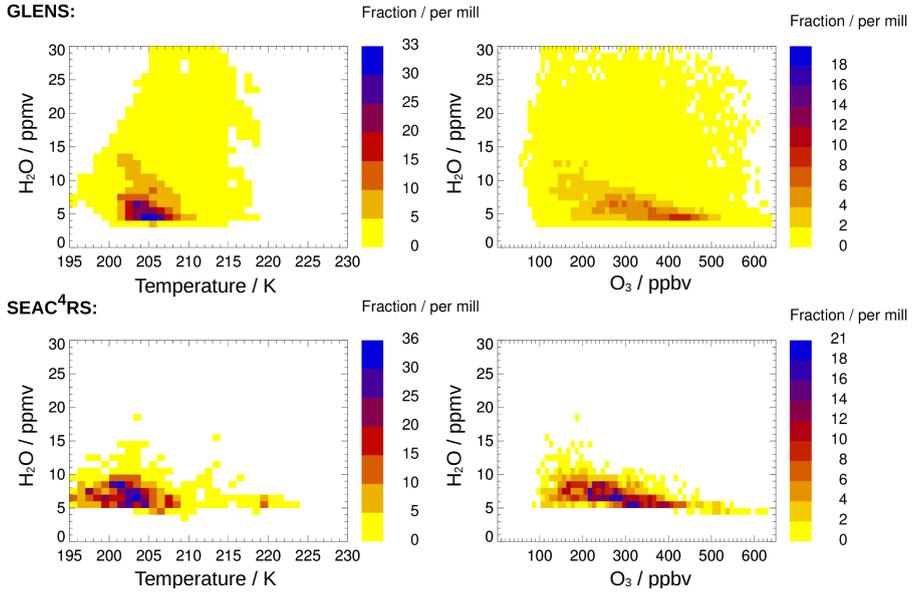
Figure 5.3: Comparison of the relative distribution of occurrence frequency of data points in the GLENS mixing layer (C2010) between stratospheric and tropospheric air masses (top) with measurements of the SEAC^{4}RS aircraft campaign (bottom). Left panels show the relative frequency distribution regarding water vapour and temperature conditions and right panels regarding water vapour and ozone mixing ratios. The relative frequency distribution is derived by calculating the number of data points found in a specific temperature and water vapour bin (1 K × 1 ppmv H_2O, left) or ozone and water vapour bin (10 ppbv O_3× 1 ppmv H_2O, right) considering all water vapour and temperature (ozone) ranges given in Tab. 5.2. The number of data points of each temperature-H_2O (O_3-H_2O) bin is normalized by the total number of data points. The colour scheme marks these fractions.

holding a CO mixing ratio of more than 31 ppbv. Both mixing layers comprise a main ozone range of ∼100–600 ppbv and only few data points with more than 650 ppbv O_3.

Fig. 5.3 (top) shows the relative frequency distribution of data points in the GLENS mixing layer (C2010) in the temperature-water vapour (left) and ozone-water vapour (right) correlation. The relative frequency distribution is determined as described in Sec. 4.1.2 considering all temperature and water vapour (ozone and water vapour) bins of the size of 1 K×1 ppmv H_2O (10 ppbv O_3× 1 ppmv H_2O) in all water vapour and temperature (ozone) ranges given in Tab. 5.2. The number of data points of each temperature-H_2O (O_3-H_2O) bin is normalized by the total number of data points found

in the GLENS mixing layer. These fractions are colour-coded in Fig. 5.3. Further,
Fig. 5.3 (bottom) shows the relative frequency distribution of data points in the mixing
layer derived from SEAC^{4}RS measurements in the same way.

Comparing the SEAC^{4}RS and GLENS mixing layers yields a similar relative frequency
distribution regarding temperature and H_2O conditions. Above 5 ppmv H_2O, the
maximal fractions of GLENS and SEAC^{4}RS data lay in the same water vapour and
temperature range of 201–207 K and 5–8 ppmv H_2O (Fig. 5.3, left). However, SEAC^{4}RS
data show a higher fraction at lower temperatures of 197–200 K. In the GLENS data,
a higher fraction shows lower water vapour mixing ratios than 5 ppmv. Furthermore,
GLENS data spread over a broader water vapour range.

The SEAC^{4}RS and GLENS mixing layers show a similar distribution regarding the
H_2O-O_3-correlation (Fig. 5.3, right). A significant fraction of all data corresponds to an
ozone range of 200–350 ppbv, but in the GLENS data a higher fraction shows low water
vapour mixing ratios with an ozone mixing ratio of 400–450 ppbv. The higher fraction
of air masses with more ozone than 450 ppbv in the selected GLENS mixing layer than
in the mixing layer deduced from SEAC^{4}RS measurements indicates a higher fraction
of stratospheric air in the mixing layer. This may be caused by more air parcels in the
GLENS mixing layer corresponding to a higher altitude than in the SEAC^{4}RS mixing
layer, because SEAC^{4}RS data depend on the flight height during the measurement.

In addition to SEAC^{4}RS measurements, data in the GLENS mixing layer are compared
with measurements sampled during the Stratosphere-Troposphere Analyses of Regional
Transport (START08) campaign (Pan et al., 2010), which covers a larger latitude range
over central North America than the SEAC^{4}RS measurements. The START08 campaign
was designed to characterize the transport pathways in the extra-tropical tropopause
region using the U.S. National Science Foundation (NSF) Gulfstream V (GV) research
aircraft. START08 measurements show a good overall agreement with GLENS results,
in spite of the fact that a higher fraction of air masses sampled during START08 has
temperatures higher than 215 K caused by the maximum flight height of the GV of
~14.5 km (for more information see Appendix E).

The data points from GLENS representing the mixing layer show a good overall

agreement with data points in the mixing layer deduced from aircraft measurements above central North America. Measurements during SEAC^{4}RS sampled convective injections penetrating water vapour into the stratosphere (Toon et al., 2016) and thus provide unusual cold and moist conditions for the lowermost stratosphere. Therefore, the higher fraction of air masses describing temperatures of 197–200 K in the SEAC^{4}RS measurements is considered as a case study in Sec. 5.3.5.

5.2.2 Change in the chemical composition of the mixing layer

The chemical composition of the mixing layer changes in the GLENS future scenarios. In Fig. 5.4, the E90-O_3-correlation is shown for all considered cases (see Tab. 5.1). In the climate change scenario (C2040, C2090), the O_3 mixing ratio increases during the 21st century, but the ozone mixing ratio in the geoengineering scenario (F2040, F2090) remains in a similar range of ~200–600 ppbv as in case C2010. The correlation between ozone and the artificial tropospheric tracer E90 for case C2010 (grey), shown in Fig. 5.4, agrees well with the F2040 case (red) and the the F2090 case (blue). For the cases with climate change, the ozone mixing ratio is significantly higher in case C2040 (yellow) and C2090 (green) especially for low E90 concentrations. The enhancement of ozone in the mixing layer could be related to a higher ozone smog production because of a higher atmospheric CH_4 burden with increasing CH_4 emissions in the RCP8.5 scenario. Furthermore, climate change is expected to increase upper stratospheric ozone and accelerate the BDC transporting more ozone from high altitudes downwards in the lowermost stratosphere (Iglesias-Suarez et al., 2016).

  Besides changes in transport, ozone in the mid-latitude mixing layer could be affected by changes in chemistry (e.g. through chlorine activation). The conditions causing heterogeneous chlorine activation are determined first of all by temperature and water vapour mixing ratios. Furthermore, Cl_y- and NO_y-mixing ratios affect the threshold between conditions, which may or may not lead to chlorine activation (as previously described in Sec. 4.3). The distribution of temperatures and several trace gas mixing ratios within the GLENS mixing layer is shown in Fig. 5.5 for the subtropical (Lat. 30–35°N) and the extra-tropical (Lat. 44–49°N) latitude band over central North America.
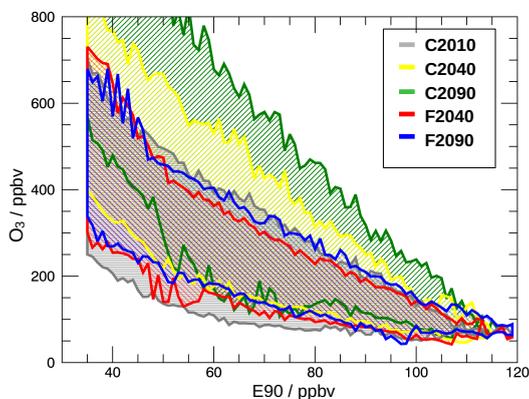
Figure 5.4: O_3-E90-correlation in the GLENS mixing layer for today (C2010) and
the future scenarios considering both a climate change (C2040, C2090) and additional
geoengineering (F2040, F2090). An overview on the presented cases is given in Tab. 5.1.

In all future scenarios, temperatures and water vapour mixing ratios increase (Fig. 5.5).
In the subtropical latitude band, the median temperature increases from today to the
end of the 21st century by $\sim3\,\mathrm{K}$ assuming a climate change scenario and by $\sim5.5\,\mathrm{K}$
when applying geoengineering. In the extra-tropical latitude band, the temperature
is higher and shows a similar increasing tendency. Temperatures increase more in
the geoengineering scenario due to additional absorption of longwave radiation by the
injected sulfate particles. Water vapour mixing ratios are higher in the extra-tropical
latitude band than in the subtropical band and spread over a broader range. In both
latitude ranges and future scenarios the water vapour content increases until the end
of the 21st century driven by increasing temperatures of the tropical tropopause layer.
An increase in water vapour enhances HO_x-mixing ratios (Fig. 5.5) and thus likely
accelerates ozone destruction in the HO_x-cycle (C2).

The HCl and ClO_x mixing ratios decrease in the GLENS simulations for future scenarios
due to the implementation of boundary conditions in the WACCM according to the
Montreal Protocol and its amendments and adjustments. However, the median ClO_x
mixing ratio is higher by $\sim8\,(30\text{--}34°N)\text{--}22\%\,(44\text{--}49°N)$ in the F2040 case than in the
C2040 case. This could be due to a reduced NO_x mixing ratio in the F2040 case. In
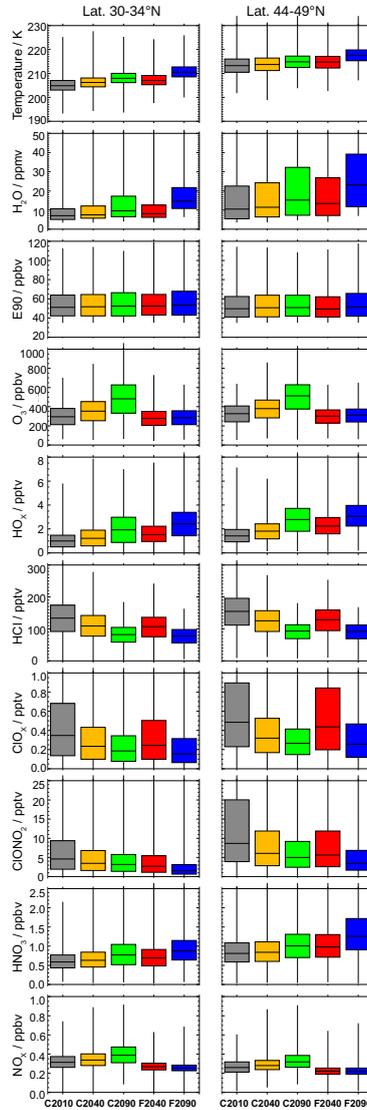
Figure 5.5: Distribution of temperatures and several trace gas mixing ratios in the GLENS mixing layer for case C2010 and future scenarios considering both climate change (C2040, C2090) and in addition sulfate geoengineering (F2040, F2090) (see Tab. 5.1). The frequency distribution is illustrated as box-plots, where the upper and lower quartile (75% and 25%) of the data set is marked by the upper and lower end of the box. The median of the temperature or mixing ratio values within the mixing layer is illustrated through the horizontal line in the box. Ends of vertical lines mark the minimum and the maximum value of the considered data.

both future scenarios, the HNO_3 mixing ratio increases until the year 2100 (Fig. 5.5).
For climate change, the NO_x mixing ratio increases as well. It decreases in the geo-
engineering scenario, because HNO_3 formation through heterogeneous reactions (e.g.
R 29, $N_2O_5+H_2O$) is accelerated by a higher aerosol abundance. Less NO_x causes less
ClO_x to be bound in $ClONO_2$ resulting in more gas phase ClO_x in the geoengineering
scenario. Additionally, the occurrence of heterogeneous chlorine activation could yield
an enhancement of ClO_x in the geoengineering scenario caused by an enhanced aerosol
abundance.

The changes in chemistry may affect the future ozone abundance in the lowermost
stratosphere. The median ozone mixing ratio increases by 60–67% until the year 2100 in
the climate change scenario but remains at today's level in the geoengineering scenario
(Fig. 5.5). The partitioning between active radicals (ClO_x , NO_x) and reservoir species
(HCl, HNO_3) differs between the climate change (C2040, C2090) and the geoengineering
(F2040, F2090) cases resulting in a different chemical impact on ozone. The likelihood
for the occurrence of ozone loss caused by heterogeneous chlorine activation may differ
as well in the future scenarios, because the heterogeneous chlorine activation is stronger
for low temperatures and enhanced water vapour mixing values. The likelihood of
heterogeneous chlorine activation to occur and its impact on the ozone chemistry is
analysed below in the subsequent section.

5.3   Comparison of GLENS results with chlorine activation thresholds

The water vapour and temperature range, in which heterogeneous chlorine activation occurs, is determined by calculating chlorine activation thresholds for the specific chemical composition of each data group using the CLaMS model. The chlorine activation threshold is determined based on the composition of air masses in the mixing layer between tropospheric and stratospheric air deduced from GLENS results (see Sec. 5.1.1). The fraction of all air masses in the GLENS mixing layer between the troposphere and the stratosphere with conditions leading to chlorine activation accounts for the likelihood that chlorine activation occurs in the considered cases.

Chlorine activation thresholds are calculated for all cases (see Tab. 5.1) with CLaMS (see Sec. 5.1.2) for 4 latitude ranges from 30–49°N, 5 pressure ranges between 70 and 300 hPa and 5 different ozone ranges from 150–650 ppbv (see Tab. 5.2). Ozone values lower than 150 ppbv are not considered here, because only a minor fraction of air parcels shows less than 150 ppbv ozone. Furthermore, a critical ozone amount has to be exceeded for chlorine activation to occur (von Hobe et al., 2011), because a higher ozone mixing ratio causes a higher ClO/Cl-ratio and thus more $ClONO_2$ formed. This is important for heterogeneous chlorine activation in reaction R 21 to occur.

5.3.1   Analysis of chlorine activation thresholds

Both the chlorine activation threshold and the H_2O-temperature relative frequency distribution vary depending on the assumed pressure and ozone level and thus for different data groups. An example for the impact of the pressure and the ozone range on the H_2O-temperature relative frequency distribution and the chlorine activation threshold is shown in Fig. 5.6 for the GLENS mixing layer in the latitude range of 30–35°N of the C2010 case.

The H_2O-temperature relative frequency distribution is shown (Fig.5.6, top) for an ozone range of 350–450 ppbv. The water vapour and temperature dependent chlorine activation thresholds are marked as a line for different pressure levels. In Fig. 5.6 a,
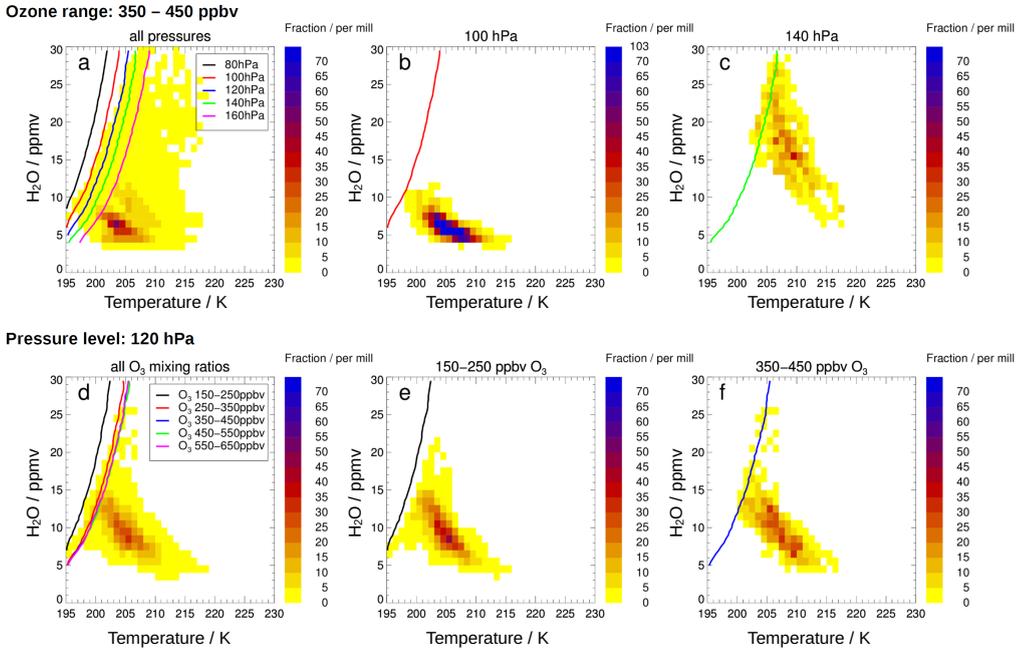
Figure 5.6: H_2O-temperature relative frequency distributions and chlorine activation thresholds of different data groups (see Tab. 5.2) for the GLENS C2010 case and a latitude range of 30–35°N. The H_2O-temperature relative frequency distribution is illustrated as a colour scheme. The colour marks the fraction of the considered data corresponding to a water vapour and temperature bin ($1 \, \text{ppmv} \, H_2O \times 1 \, \text{K}$). The water vapour and temperature dependent chlorine activation thresholds are marked as a line. Top panels are related to data groups with an ozone mixing ratios of 350–450 ppbv: all data in the considered latitude and ozone range (30–35°N, 350–450 ppbv O_3) (a); the data group defined by a latitude of 30–35°N, an ozone mixing ratio of 350–450 ppbv O_3 and the 100 hPa pressure level (b); and the data group defined by a pressure level of 140 hPa and the same latitude and ozone range (c). Bottom panels are related to data groups with a pressure level of 120 hPa: all data in the considered latitude and pressure level (30–35°N, 120 hPa) (d); the data group defined by a latitude of 30–35°N, a pressure level of 120 hPa and an ozone mixing ratio of 150–250 ppbv O_3 (e); and the data group defined by an ozone mixing ratio of 350–450 ppbv and the same latitude and pressure level (f).

chlorine activation thresholds are plotted for all pressure levels in the considered lati-
tude and ozone range (30–35°N, 350–450 ppbv O_3). At higher pressure levels (lower
altitudes), the chlorine activation threshold is shifted allowing chlorine activation to
occur at higher temperatures (Fig. 5.6 a). This shift is due to an increasing liquid
particle formation as well as more $ClONO_2$ absorbed by an aerosol particle at higher
pressures. The heterogeneous chlorine activation rate of reaction R 21 is determined
by the $ClONO_2$ uptake into the aerosol particle (Shi et al., 2001). Air masses lying
on the left side of the chlorine activation threshold promote chlorine activation. The
relative frequency distribution shown in Fig. 5.6 a, is related to all air masses with
350–450 ppbv ozone in a latitude range of 30–35°N. Some data points cross various
activation thresholds.

However, only data points crossing the chlorine activation threshold and in addition
corresponding to the pressure level of the activation threshold will yield activated
chlorine. As an example, the chlorine activation thresholds at the 100 hPa and 140 hPa
level are plotted together with the GLENS relative frequency distribution corresponding
to the same data group (Fig. 5.6 b, c). Air masses in the 100 hPa level (Fig. 5.6 b) are
colder and dryer than those at 140 hPa (Fig. 5.6 c). Hence, at the 100 hPa level no
chlorine will be activated (there are no data corresponding to a H_2O-temperature bin
on the left side of the threshold line) and chlorine activation occurs for the 140 hPa
level only for data points with a high water vapour mixing ratio.

In Fig. 5.6 (bottom), the H_2O-temperature relative frequency distribution and the chlo-
rine activation thresholds are presented for a pressure level of 120 hPa. The impact
of the ozone mixing ratios on the chlorine activation threshold is illustrated. Fig 5.6 d
shows the GLENS H_2O-temperature relative frequency distribution and the chlorine
activation thresholds for all data groups corresponding to the selected latitude range and
pressure level (30–35°N, 120 hPa). Higher ozone mixing ratios are related to higher Cl_y
amounts. Hence, an increase in ozone shifts the chlorine activation threshold to higher
temperatures (Fig. 5.6 d). However, considering the relative frequency distribution of
specific data groups with different ozone levels, data points with more ozone are warmer
than those with less ozone (Fig. 5.6 e, f).

In the future scenarios, the H_2O-temperature relative frequency distribution as well as the chlorine activation thresholds vary. In Fig. 5.7, the H_2O-temperature relative frequency distribution is shown for the cases C2010, C2090 and F2090. The relative frequency distributions are shown for the subtropical latitude band (30–35°N, Fig. 5.7a–c) and for the extra-tropical latitude band from (44–49°N, Fig. 5.7d–f). For each case analysed, additionally a selection of chlorine activation thresholds is shown. These are related to different ozone and pressure levels and give a range of uncertainty for the water vapour and temperature ranges causing chlorine activation.

In agreement with the changes of the conditions in the mixing layer described in Sec. 5.2, the future H_2O-temperature relative frequency distributions (C2090 in Fig. 5.7 b, F2090 in Fig. 5.7 c) are both moister and warmer than the conditions today (C2010, Fig. 5.7 a). However, the geoengineering case F2090 exhibits data significantly warmer and moister than reached in the climate change case C2090. In the extra-tropic latitude band (Fig. 5.7 d–f), GLENS results are generally warmer than in the subtropical latitude range.

Considering the chlorine activation thresholds in Fig. 5.7, the largest fraction of air masses corresponds to temperatures greater than the chlorine activation thresholds. The chlorine activation thresholds for the C2090 case are shifted to lower temperatures compared to case C2010, because of the lower chlorine abundance (a higher Cl_y mixing ratio promotes heterogeneous chlorine activation, see Sec. 4.3). In contrast, in the geoengineering scenario F2090 chlorine activation can occur at higher temperatures than today in spite of the lower chlorine amount. This is caused by the higher aerosol loading when sulfate geoengineering is applied.

In each case, the water vapour and temperature bins marked by the chlorine activation thresholds to potentially cause heterogeneous chlorine activation are in good agreement for both latitude ranges presented. Since the temperatures of the mixing layer are higher in the extra-tropical latitude band, the fraction of air masses crossing the chlorine activation threshold and thus causing chlorine activation is lower in that latitude range (44–49°N) than in the subtropical latitude band (30–35°N).

The chlorine activation threshold calculated for the standard case in Chapter 4 corre-
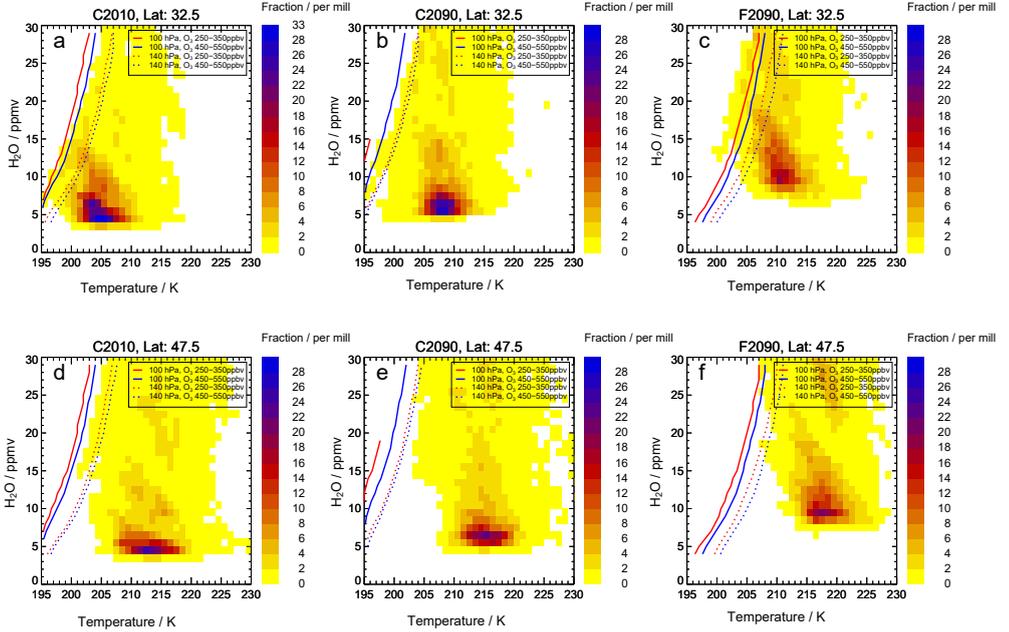
Figure 5.7: H_2O-temperature relative frequency distributions and examples for chlorine activation thresholds for the cases C2010 (a, d) and the future scenarios at the end of the 21st century assuming climate change (C2090, b, e) and additional geoengineering (F2090, c, f) for the subtropical latitude band (30–35°N, top) and the extra-tropical (44–49°N, bottom). The colour marks the fraction of the considered data corresponding to a water vapour and temperature bin (1 ppmv $H_2O \times 1$ K). The water vapour and temperature dependent chlorine activation threshold is marked as a line for exemplarily chosen data groups specified in the legend of each panel.

sponds here to the data bin with a pressure level of 100 hPa, the subtropical latitude band (30–35°N) and an ozone range of 250–350 ppbv for the C2010 case (Fig. 5.7a, red continuous line). In comparison, the activation threshold calculated for the standard case in Chapter 4 (Fig. 4.10) is shifted to higher temperatures than the chlorine activation threshold determined based on GLENS results. In case C2010, temperatures are required to fall below 201 K for chlorine activation to occur at 20 ppmv H_2O. In the standard case in Chapter 4, temperatures must be lower than 203 K for the same water vapour mixing ratio. This shift likely occurs, because for the analysis of the mechanism in Chapter 4 more Cl_y was assumed than deduced here from GLENS data (156 pptv instead of 143 pptv).

There are some chlorine activation thresholds that cannot be reported when the water vapour mixing ratio exceeds a certain value (e.g. Fig. 5.7 e, 100 hPa, 250–350 ppbv O_3). At such high water vapour mixing ratios, HCl is absorbed strongly into the aerosol particles, reducing gas phase Cl_y and thus less $ClONO_2$ may be formed. Since chlorine is activated in R 21 (HCl+$ClONO_2$), less $ClONO_2$ leads to a lower chlorine activation rate. This effect is negligible if the Cl_y mixing ratio is high enough. But if the Cl_y mixing ratio is low (e.g. in a low ozone range in the years 2090–2099), reducing gas phase Cl_y by absorbing HCl into the aerosol results in no activation of chlorine. Hence, there is no chlorine activation for these conditions.

Summarizing, the water vapour and temperature dependent chlorine activation threshold marks an upper boundary of temperatures causing heterogeneous chlorine activation for air masses with a specific water vapour mixing ratio. Thus for a given water vapour mixing ratio, the maximum temperature at which chlorine activation may occur is determined by the chlorine activation threshold. In this section was shown, that the chlorine activation thresholds and the H_2O-temperature relative frequency distribution of the GLENS mixing layer vary depending on the aerosol abundance, pressure and the Cl_y mixing ratio related to the ozone levels. Moist and very cold air masses, which in general are expected to promote heterogeneous chlorine activation, usually correspond to low pressures and low ozone mixing ratios. Hence, the pressure and ozone dependence of chlorine activation results in only few air masses with conditions suitable to activate chlorine. Thus, chlorine activation thresholds have to be compared with air masses in GLENS corresponding to the same data group regarding pressure, ozone and latitude range as the calculated chlorine activation threshold to deduce the likelihood that chlorine activation occurs.

5.3.2 Likelihood for ozone destruction today and in future

The likelihood for chlorine activation to occur is quantified here as the fraction of air masses in the GLENS mixing layer between tropospheric and stratospheric air, which are cold and moist enough to cause heterogeneous chlorine activation. Comparing GLENS air masses with chlorine activation thresholds, the number of air masses is counted

showing lower temperatures than determined as the threshold temperature for chlorine activation. The fraction of this amount in all air masses within the GLENS mixing layer yields the likelihood for heterogeneous chlorine activation to occur. Assuming that chlorine activation always yields ozone destruction processes known from polar late winter and early spring (e.g. Molina et al., 1985; McElroy et al., 1986; Crutzen et al., 1992; Solomon, 1999), the likelihood for chlorine activation to occur is the same as the likelihood for chlorine catalysed ozone destruction.

In Fig. 5.8 (top), the likelihood for chlorine activation to occur is presented considering air masses in the entire latitude range (30–49°N) of the GLENS mixing layer. Each panel corresponds to a considered case (C2010, C2040, C2090, F2040 and F2090, see Tab. 5.1). The likelihood for chlorine activation to occur is marked by the height of a bar: for single pressure levels and named 'all' for all air masses within the mixing layer. In the C2010 case, the overall likelihood for chlorine activation to occur is 1.0% in the entire latitude range and for all pressure levels (Fig. 5.8, top, left panel, left bar). However, chlorine activation occurs most likely in the pressure level of 140 hPa. A fraction of 3.5% of all air masses in the 140 hPa level causes heterogeneous chlorine activation in the C2010 case (Fig. 5.8, top, left). As described in Sec. 5.3.1, higher pressures increase the aerosol formation and the uptake of $ClONO_2$ into the liquid aerosol particles, which determines if chlorine activation through reaction R 21 (Shi et al., 2001) occurs. Thus, the chlorine activation threshold is shifted to higher temperatures at higher pressures. However, the likelihood for chlorine activation deduced from the comparison between chlorine activation thresholds and air masses in the GLENS mixing layer is lower at 160 hPa than at 140 hPa (Fig. 5.8), because air masses corresponding to higher pressure levels are warmer than those with a lower pressure (exemplary shown in Fig. 5.6 b, c). Air masses in the 160 hPa level are significantly warmer than air masses in the 140 hPa level. Hence, although the chlorine activation threshold is shifted to higher temperatures for the 160 hPa pressure level, most air masses corresponding to this high pressure are to warm for heterogeneous chlorine activation and chlorine activation occurs most likely in the 140 hPa pressure level.

The contribution of different ozone levels in the air masses, which cause chlorine
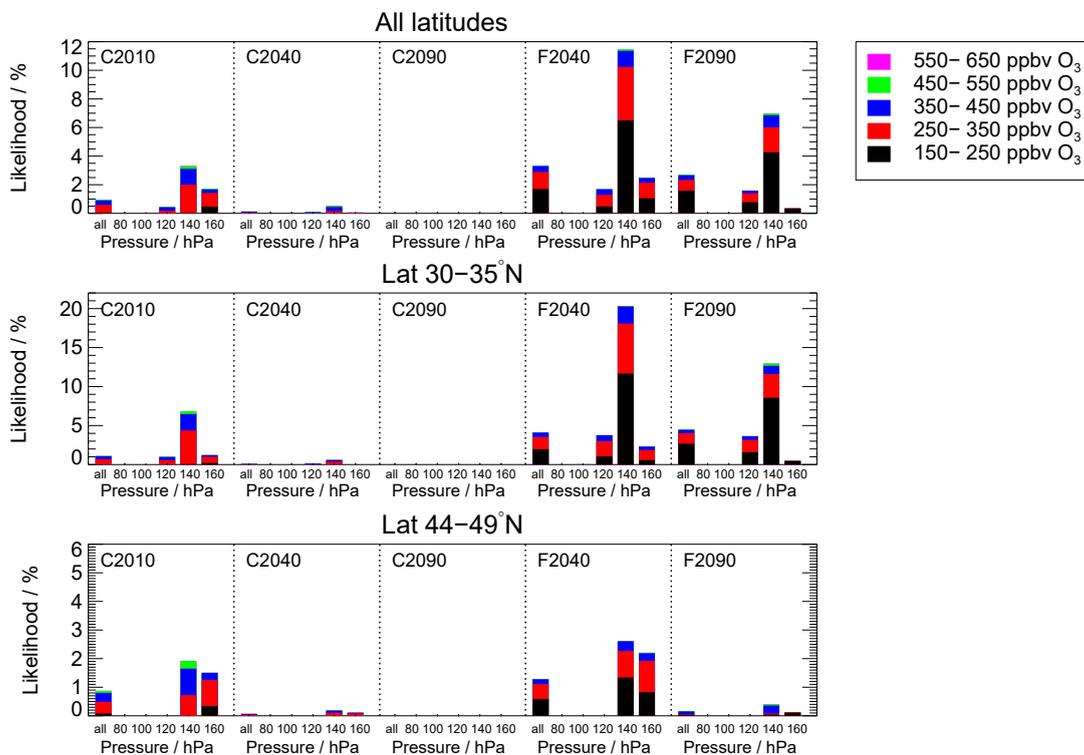
Figure 5.8: Likelihood for heterogeneous chlorine activation to occur in different latitude regions in the GLENS mixing layer for all considered cases of today and the future scenarios (see Tab. 5.1). The entire latitude range above central North America (30–49°N) is considered (top), only the subtropical latitude band (30–35°N) (middle) and only the extra-tropical latitude band (44–49°N) (bottom). Different panels correspond to different cases given at the top of each panel. The height of the bars marks the likelihood for a specific pressure level given under that bar. The pressure range corresponding to a given pressure level is given in Tab. 5.2. The denotation *all* refers to the whole pressure range of the mixing layer. Colours indicate the likelihood for chlorine activation to occur for air masses with different ozone ranges. Note the changes scale of the y-axis in different rows.

activation, is additionally marked by the colour scheme in Fig. 5.8. In case C2010, chlorine activation mainly occurs in air masses with an ozone mixing ratio of 250–350 ppbv (Fig. 5.8 top).

Focussing on the future scenarios, the likelihood for chlorine activation to occur is very low in the climate change cases C2040 and C2090 (Fig. 5.8 top). In contrast, the likelihood in the geoengineering cases F2040 and F2090 is higher than for today (case C2010). Chlorine activation occurs most likely at the mid of the 21st century in case F2040, where 3.3% of all air masses in the GLENS mixing layer would cause chlorine activation. 11.5% of the air masses in the 140 hPa pressure level cause chlorine activation in case F2040. The likelihood for chlorine activation to occur is slightly lower at the end of the 21st century due to the decrease of Cl_y implemented in GLENS. In case F2090, 2.7% of all air masses in the GLENS mixing layer cause chlorine activation. The likelihood for chlorine activation in different latitude ranges is illustrated in Fig. 5.8 in the middle (latitude range of 30–35°N) and bottom panels (latitude range of 44–49°N). In general, chlorine activation occurs more likely in the subtropical latitude band than in the extra-tropic latitudes, because of the different temperature range and chemical composition around the tropopause in the subtropics and extra-tropics (also described in Sec. 5.2 and 5.3.1). In case C2010, 1.1% of all GLENS air masses in the subtropical latitude band (30–35°N) causes chlorine activation and 0.9% in the extra-tropic latitude band (44–49°N; note the different y-scales for different latitude ranges in Fig. 5.8). In both latitude ranges, the likelihood for chlorine activation is negligible in the future cases C2040 and C2090. In contrast, the likelihood increases in the geoengineering scenario. In case F2040, 4.1% of all air masses in the subtropical latitude band of the considered GLENS mixing layer cause chlorine activation. In the same latitude range, the likelihood for chlorine activation to occur is higher in case F2090 (4.5%), in spite of the implemented decrease in stratospheric Cl_y. The likelihood increases between case F2040 and F2090, because in case F2090 a higher fraction of air masses has a pressure corresponding to the 120 hPa and the 140 hPa level than in case F2040 (not shown). In contrast, in the extra-tropical latitudes (44–49°N), the likelihood for chlorine activation to occur is higher in case F2040 (1.3%) than in case F2090 (0.2%)

caused by the decrease in stratospheric Cl_y and the warming of the mixing layer. In this latitude range, the likelihood for chlorine activation to occur is generally lower than in the subtropical latitude band, because the temperatures in the GLENS mixing layer are higher (see Fig. 5.5).

Focussing on the ozone mixing ratio of air masses causing chlorine activation in the GLENS mixing layer, the colour scheme in Fig. 5.8 indicates that chlorine activation occurs more likely in air masses with low ozone mixing ratios than with high ozone mixing ratios. This is in agreement with the dependence of the H_2O-temperature relative frequency distribution in the GLENS mixing layer on the ozone mixing ratio discussed in Sec. 5.3.1 (exemplary shown in Fig. 5.6). Air masses with higher ozone mixing ratios are warmer than those with less ozone and thus cause less likely heterogeneous chlorine activation.

In summary, the occurrence of chlorine activation and the resulting catalytic ozone loss processes similar to those known from polar regions is unlikely based on the comparison of GLENS results with chlorine activation thresholds. However, chlorine activation occurs more likely in the future scenario assuming geoengineering than in today's case C2010. In the future scenario assuming climate change, the likelihood for chlorine activation to occur is negligible. Furthermore, chlorine activation is more likely in lower latitudes than in higher latitudes. Since in air masses causing chlorine activation usually low ozone mixing ratios prevail, the ozone amount affected by chlorine catalysed ozone destruction is expected to be low. How relevant the activation of chlorine is for the ozone chemistry in the mid-latitude lowermost stratosphere is analysed in the next section.

5.3.3 Impact of heterogeneous chlorine activation on ozone in the lowermost stratosphere

How much ozone in the mixing layer above central North America is affected by the heterogeneous chlorine activation process is analysed here by considering the ozone changes in the CLaMS simulations together with the relative frequency distribution in GLENS.

CLaMS simulations are conducted for all data groups and any combination of temperature and water vapour bins. The difference between initial and final ozone within each 10 day simulation yields for each data group (determined by a latitude, pressure and ozone range, see Tab. 5.2) the chemical ozone change corresponding to a particular water vapour and temperature bin ($1\,\mathrm{K} \times 1\,\mathrm{ppmv}\ H_2O$ in a range of 195–230 K and 4–30 ppmv H_2O). Since no mixing is allowed in the box-model runs, in this way conditions, which lead to chlorine activation, are not disturbed within 10 days. In the lowermost stratosphere, the duration of maintenance for conditions causing chlorine activation is not yet known. However, mixing of cold and moist air from the troposphere uplifted to above the tropopause (e.g. through convective overshooting) with dry and warmer stratospheric air will reduce the water vapour content of the moist air parcel. Since the occurrence of chlorine activation depends on both the temperature and the water vapour mixing ratio of the air parcel, a decrease in water vapour can stop chemical chlorine activation. Hence, assuming the maintenance of chlorine activation for 10 days without a perturbation by mixing here, accounts for an upper boundary for the impact of heterogeneous chlorine activation on ozone in the mid-latitude lowermost stratosphere.

The chemical ozone change between the initial and final ozone of a 10 day box-model simulation is multiplied with the number of GLENS air masses corresponding to the same data group and water vapour and temperature bin. In this way, the total chemical ozone change in the mid-latitude mixing layer is estimated. The total initial ozone is calculated by multiplying the median ozone amount of each data group with the number of GLENS air masses corresponding to that data group. The ratio of the total ozone change from the start to the end of the 10 day CLaMS simulation and the total initial ozone yields the relative ozone change.

The relative ozone change in the GLENS mixing layer determined from the difference between final and initial ozone in the 10 day CLaMS box-model simulations for each considered case is illustrated as black bars in Fig. 5.9 (top). In case C2010, chemical ozone formation dominates the ozone chemistry in the mixing layer and causes an increase in ozone of 2.3%. In the future climate change scenario, ozone would increase

by around 2.5% within 10 days of unperturbed chemistry in case C2040 and by 3% in case C2090. This increasing ozone in the future may be related to the reduction of ODS implemented in GLENS. In the geoengineering scenario, the relative chemical ozone formation is lower than following a climate change. However, the ozone change increases from +2.3% in the F2040 case to +2.6% in the F2090 case. The lower chemical ozone increase in the mixing layer for the geoengineering scenario is based on an increase of ozone destruction processes. Ozone destruction catalysed by HO_x-radicals is more likely in the geoengineering scenario because of the higher HO_x mixing ratio (Fig. 5.5). Furthermore heterogeneous chlorine activation could yield ozone destruction.

The relative ozone change caused by heterogeneous chlorine activation is shown in Fig. 5.9 (bottom). For calculating the relative ozone change caused by heterogeneous chlorine activation, ozone changes corresponding to air masses which cause chlorine activation are multiplied with the number of these air masses in the GLENS mixing layer. This ozone change from air masses in which chlorine activation can occur is normalized with the total initial ozone of all air masses in the GLENS mixing layer. Black bars correspond to air masses in the entire latitude region above central North America. In case C2010, 0.1% of ozone in the mixing layer would be destroyed within 10 days caused by heterogeneous chlorine activation. In the climate change scenarios, chlorine activation causes less ozone destruction in the mixing layer. Heterogeneous chlorine activation has the strongest impact on ozone in the GLENS mixing layer of the F2040 case. In this case, 0.3% of ozone in the mixing layer would be destroyed, if the chemical conditions yielding chlorine activation are maintained for 10 days. In comparison, for the conditions in case F2090 0.1% of ozone in the mixing layer would be destroyed.

In Fig. 5.9, additionally the relative ozone change calculated based on 10 day CLaMS box-model simulations is illustrated with respect to the latitude ranges 30–35°N (red bars) and 44–49°N (blue bars). Comparing the relative ozone change in different latitude regions, in the subtropical latitude band more ozone is formed (Fig. 5.9 top). For example in case C2010, ozone increases by 3.4% in the subtropical latitude band (30–35°N) and by 1.2% at 44–49°N. However, in the subtropical latitude band het-
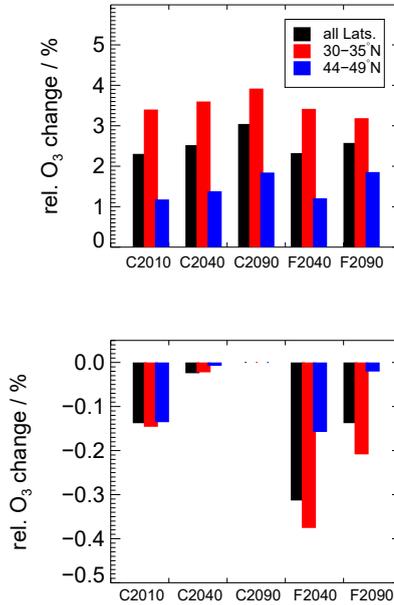
Figure 5.9: Relative chemical ozone change in the mixing layer determined from the difference between initial and final ozone in 10 day CLaMS box-model simulations (no mixing between air masses) in all considered cases (see Tab. 5.1). The relative ozone change is shown (top) considering the entire latitude region above central North America (black bars) as well as only considering the subtropical (30–35°N, red bars) or extra-tropical (44-49°N, blue bars) latitude region. Further, the ozone change from air masses in which chlorine activation can occur normalized by the total initial ozone from all air masses in the GLENS mixing layer is shown (bottom).

erogeneous chlorine activation affects ozone more (Fig. 5.9 bottom). Heterogeneous chlorine activation causes the strongest ozone destruction in the mixing layer for the geoengineering case F2040 with an ozone destruction of 0.4% in 10 days at 30–35°N. In contrast, in case C2040 less than 0.1% would be destroyed in the same latitude range.

Since in the subtropical latitude range (30–35°N) the effect of heterogeneous chlorine activation on ozone in the highest, the relative ozone change in that latitude range is shown more detailed with respect to single pressure levels in Fig. 5.10. In general, ozone formation processes dominate at low pressures, causing a net chemical ozone
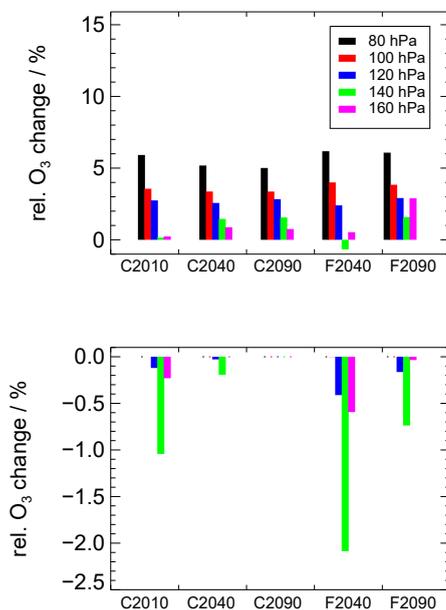
Figure 5.10: Relative chemical ozone change in the subtropical latitude band (30–35°N) in the mixing layer determined from the difference between initial and final ozone in 10 day CLaMS box-model simulations in the considered cases (see Tab. 5.1). The overall ozone change (top) within single pressure levels between 70 and 300 hPa (see Tab. 5.2) is shown as well as the ozone change from air masses in which chlorine activation can occur normalized by the total initial ozone from all air masses in the GLENS mixing layer (bottom).

increase (Fig. 5.10 top). In higher pressure levels, the net ozone formation is lower. Furthermore, the occurrence of heterogeneous chlorine activation is more likely at higher pressure levels. In the F2040 case where heterogeneous chlorine activation has the strongest impact on ozone chemistry in the mixing layer, up to 2.1% of total initial ozone in the pressure level of 140 hPa are destroyed in air masses with conditions allowing heterogeneous chlorine activation (Fig. 5.10 bottom). This results in a net ozone change in this pressure level of -0.7% (Fig. 5.10 top), when both the ozone destruction in air masses allowing chlorine activation and ozone formation in all the other air masses in the 140 hPa level are considered.

The likelihood for chlorine activation to occur in the mid-latitude mixing layer just above the tropopause, the relative ozone change caused by heterogeneous chlorine activation and the net chemical ozone change in the GLENS mixing layer determined from 10 day CLaMS box-model simulations are summarized in Tab. 5.3 considering the entire latitude range (30–49°N) as well as for the subtropical (30–35°N) and the extra-tropical (44–49°N) latitude band. The results calculated here are referred to as 'reference'.

Summarizing, the impact of heterogeneous chlorine activation causing chlorine catalysed ozone destruction on ozone in the mid-latitude lowermost stratosphere is low. Combining the occurrence of conditions in GLENS with the chemical ozone change determined through CLaMS box-model simulations, in all cases a net chemical ozone formation will occur above central North America. However, chlorine activation may affect ozone in the mixing layer. In the geoengineering scenario in case F2040 chlorine activation has the highest impact on ozone in comparison to the other cases and can cause an ozone reduction of up to 0.38%. However, the ozone changes determined in this study give an upper limit for ozone change caused by heterogeneous chlorine activation, because mixing between air masses is neglected in the box-model simulations used to calculate the chemical ozone change.

5.3.4 Relevance of heterogeneous chlorine activation in the mixing layer for the mid-latitude ozone column

In the previous section, an upper limit for ozone reduction caused by heterogeneous chlorine activation in the mid-latitude mixing layer between tropospheric and stratospheric air was determined. Based on this relative ozone change in the mixing layer, the impact of heterogeneous chlorine activation in the mid-latitude lowermost stratosphere on column ozone is deduced.

For all of the GLENS cases today and in future (see Tab. 5.1), first the ozone profile is determined by averaging over the ozone mixing ratio within each GLENS vertical level. Both the entire latitude region above central North America and specific latitude regions (30–35°N and 44–49°N) are considered. Subsequently, the column ozone is

Table 5.3: Overview on the likelihood for chlorine activation to occur in the mid-latitude mixing layer above the tropopause, its impact on ozone in the mixing layer and the relevance for column ozone. Further the net chemical ozone change in the mixing layer is specified. Three latitude ranges are considered here: 30–49°N, only the subtropical latitude band in 30–35°N and only the extra-tropical latitude band in 44–49°N. The considered cases today (C2010) and in the future scenarios assuming a climate change (C2040, C2090) and additional geoengineering (F2040, F2090) are further described in Tab. 5.1. The reference refers to results deduced from the GLENS mixing layer. In the assumption with 2 K lower temperatures, temperatures of GLENS air masses are reduced of 2 K to infer uncertainties in GLENS temperatures. The chemical ozone changes here mark an upper limit for the impact of heterogeneous chlorine activation in the mixing layer on ozone, because ozone changes are determined based on 10 day box-model simulations neglecting mixing between neighbouring air masses. Thus conditions causing chlorine activation are assumed here to be maintained for 10 days without perturbations.

	O_3-Column / DU	O_3-Column in the mixing layer / DU	Reference				2 K lower temperatures			
			Likelihood for chlorine activation	net ozone change	rel. O_3-loss	O_3-loss / DU	Likelihood for chlorine activation	net ozone change	rel. O_3-loss	O_3-loss / DU
C2010										
all Lats.	295.8	15.7	1.0%	2.3%	0.1%	0.02	3.7%	1.8%	0.5%	0.08
30–35°N	289.9	14.2	1.1%	3.4%	0.2%	0.02	4.4%	2.8%	0.5%	0.07
44–49°N	307.8	20.3	0.9%	1.2%	0.1%	0.03	2.4%	0.9%	0.4%	0.08
C2040										
all Lats.	307.2	16.9	0.1%	2.5%	<0.1%	<0.01	1.4%	2.4%	0.1%	0.02
30–35°N	299.0	13.9	0.1%	3.6%	<0.1%	<0.01	2.1%	3.3%	0.2%	0.03
44–49°N	319.2	21.4	0.1%	1.4%	<0.1%	<0.01	0.5%	1.3%	0.1%	0.01
C2090										
all Lats.	321.7	18.8	0.0%	3.0%	0.0%	0.00	0.2%	3.0%	<0.1%	<0.01
30–35°N	309.6	15.5	0.0%	3.9%	0.0%	0.00	0.3%	3.9%	<0.1%	<0.01
44–49°N	336.9	23.8	0.0%	1.8%	0.0%	0.00	<0.1%	1.9%	0.0%	0.00
F2040										
all Lats.	302.7	15.2	3.3%	2.3%	0.3%	0.05	6.7%	1.8%	0.8%	0.11
30–35°N	296.0	12.8	4.1%	3.4%	0.4%	0.05	8.9%	2.7%	0.9%	0.11
44–49°N	313.6	19.1	1.3%	1.2%	0.2%	0.03	3.8%	0.8%	0.5%	0.10
F2090										
all Lats.	321.1	17.0	2.7%	2.6%	0.1%	0.02	7.3%	2.1%	0.4%	0.07
30–35°N	310.0	14.7	4.5%	3.2%	0.2%	0.03	11.6%	2.5%	0.6%	0.09
44–49°N	334.3	21.5	0.2%	1.9%	<0.1%	<0.01	0.8%	1.8%	0.1%	0.02

calculated from the ozone profile. In Tab. 5.3 the total column ozone is shown as well as the ozone column in the mixing layer.

The ozone column in the mixing layer is assumed to correspond to the ozone column in a pressure range from 70–300 hPa. Despite the mixing layer comprises pressures between 70 and 300 hPa, not all air masses within this pressure range are necessarily part of the mixing layer, because only air parcels above the thermal tropopause and with more than 31 ppbv CO are assumed to form the stratospheric mixing layer between tropospheric and stratospheric air. Hence, for determining the ozone column in the mixing layer, not only air masses in the mixing layer but also all further air masses between 70 and 300 hPa are considered. Since the composition of air parcels in the mixing layer consists of lowermost stratospheric air mixed with tropospheric air, the ozone mixing ratio in these air parcels is somewhat smaller than the mixing ratio in air masses with the same pressure range and stratospheric character. Hence, the ozone column deduced from all air parcels in a pressure range from 70–300 hPa is expected to be somewhat larger than it would be considering only air parcels in the mixing layer. Thus in Tab. 5.3, the ozone column in the mixing layer might be overestimated.

In Sec. 5.3.3 the relative ozone destruction in the mixing layer caused by heterogeneous chlorine activation was determined and is given in Tab. 5.3. From the relative ozone loss and the ozone column in the mixing layer, the ozone loss caused by heterogeneous chlorine activation in Dobson Units (DU) can be calculated.

The relative ozone loss in the mixing layer caused by heterogeneous chlorine activation is low. Thus, the maximum total ozone loss given in Tab. 5.3 is negligible compared with the total ozone column. Even in case F2040, where the chlorine activation causes most ozone destruction in the mixing layer, the total ozone loss accounts not to more than 0.05 DU. This are less than 0.1% of the total ozone column.

5.3.5   Likelihood of heterogeneous chlorine activation and its impact on ozone for low temperatures

As discussed in Sec. 5.2.1, the temperatures in GLENS may be higher than in the real stratospheric mixing-layer. Therefore, a case study is performed assuming a shift in

GLENS temperatures of –2 K to explore the impact of uncertainties in the simulated GLENS temperatures. The likelihood for the occurrence of heterogeneous chlorine activation assuming lower temperatures and its impact on ozone in the lowermost stratosphere is presented in Fig. 5.11.

The likelihood that chlorine activation occurs would increase significantly assuming lower temperatures (Fig. 5.11, top). Chlorine activation would occur with a likelihood of 3.7% for case C2010 instead of 1% assuming the temperatures from GLENS. Furthermore the likelihood would increase in the C2040 case. A fraction of 1.4% of all data in that case would cause chlorine activation (0.1% assuming GLENS temperatures). Applying geoengineering would cause the highest likelihood for chlorine activation to occur. In the case F2040 6.7% and in F2090 7.4% of the air masses would yield chlorine activation.

Despite of the higher likelihood of chlorine activation in the F2090 case, ozone is more affected in the F2040 case, because the ozone values in the range where ozone destruction would occur in the years 2040–2050 are higher than in the years 2090–2100 (not shown). Activated chlorine would destroy up to ∼0.8% of ozone in the lowermost stratosphere in the F2040 case, but only up to 0.4% in case F2090 (Fig. 5.11 bottom, black). Today and in the climate change scenario, more ozone would be likewise destroyed due to heterogeneous chlorine activation. This higher ozone destruction results in a reduced net ozone formation comparing with the GLENS conditions. Except of the years 2090–2100 in the climate change scenario, the relative net ozone change (Fig. 5.11, middle) is significantly reduced for all cases considered. Comparing the behaviour in different latitude regions, the impact of heterogeneous chlorine activation on ozone is higher in lower latitudes.
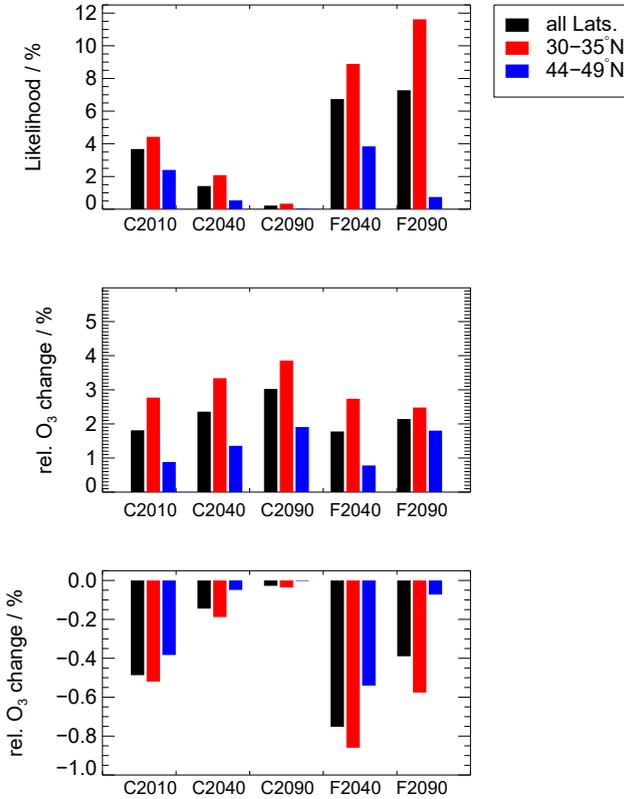
Figure 5.11: Likelihood (top) for the occurrence of chlorine activation as well as its impact on ozone in the lowermost stratosphere assuming 2 K lower temperatures than generated by GLENS. Further, the chemical ozone change in the mixing layer assuming 10 days without mixing of air parcels (middle) and the relative ozone change in the mixing layer caused by heterogeneous chlorine activation (bottom) is shown for the assumption with 2 K less temperatures. (See Tab. 5.1 for case descriptions.)

The likelihood for heterogeneous chlorine activation to occur and its impact on ozone in the mixing layer determined in this section is summarized in Tab. 5.3 referred to as '2 K' lower temperatures. Assuming a reduction of 2 K of the GLENS temperatures increases the likelihood for heterogeneous chlorine activation to occur as well as its impact on lowermost stratospheric ozone. In all cases, the relative ozone loss in the mixing layer is two to three times higher assuming 2 K lower GLENS temperatures

than in the reference. However, even for this upper limit, less than 0.8% of ozone in the mixing layer would be destroyed in the F2040 case, which shows the highest impact of activated chlorine on ozone. In all cases considered, an upper limit of 0.11 DU from a total ozone column of ∼303 DU in this region (which is less than 0.1%) has been estimated as the total ozone reduction caused by heterogeneous chlorine activation. Despite occurrence of heterogeneous chlorine activation, the net ozone change in the mixing layer during a 10 day period is found to be positive (hence, in all cases a net chemical ozone formation occurs in the mixing layer).

5.4 Discussion

The relevance of heterogeneous chlorine activation for the ozone changes in the lower-most stratosphere is analysed here for conditions today and in future assuming both climate change and the additional application of sulfate geoengineering.

Focussing on the GLENS mixing layer in mid extra-tropical latitudes, median ozone increases by 60% (30–35°N) to 67% (44–49°N) by the end of the 21st century assuming climate change. In contrast, Ball et al. (2018) reported evidence for a decrease in mid-latitude lower stratospheric ozone between the years 1998 and 2016. This ozone decrease was attributed to be dynamically driven (Chipperfield et al., 2018; Ball et al., 2019) by non-linear effects not yet completely understood and usually not implemented in climate models (Ball et al., 2019). However, this ozone decrease was found to be small with respect to the inter annual variability of ozone. This decrease results in a total ozone reduction of 1.9 DU between the years 1998 and 2018 in the lower stratosphere at 30–50°N. In comparison, ozone loss caused by heterogeneous chlorine activation analysed here and potentially occurring in the mid-latitude lower stratosphere in summer is found to cause an ozone loss of less than 0.1 DU for present day conditions (case C2010) in the same latitude range.

This reduction of column ozone is determined based on the contribution of ozone in the mixing layer to total column ozone. In case C2010, GLENS air masses in a pressure range between 70 and 300 hPa contribute 4.9% to the ozone column in a latitude range

of 30–35°N and 6.6% in 44–49°N. In comparison, Logan (1999) found a contribution of ozone between the thermal tropopause and 100 hPa on the total ozone column in summer of ∼6% in a latitude of 38°N and of ∼17% in 53°N. Thus in GLENS, the mixing layer contributes less to the ozone column than in the study of Logan (1999) deduced from satellite measurements between the years 1980 and 1993. However, if ozone in the GLENS mixing layer would contribute as much to column ozone as in the study of Logan (1999), only 0.03 DU of ozone would be destroyed for today's conditions at 30–35°N and 0.05 DU at 44–49°N.

In all cases investigated here, a net chemical ozone formation occurs in the lowermost stratosphere. Ozone is formed there due to high CO and CH_4 mixing ratios which result from transport from the troposphere to the lowermost stratosphere. Hence, the oxidation of CO and CH_4, which usually forms ozone in the upper troposphere, causes ozone formation in the lowermost stratosphere as well (Lelieveld et al., 1997; Johnston and Kinnison, 1998). However, a potential ozone destruction in the mid-latitude lowermost stratosphere due to heterogeneous chlorine activation was discussed in previous studies (e.g. Keim et al., 1996; Anderson et al., 2012, 2017; Anderson and Clapp, 2018; Schwartz et al., 2013; Berthet et al., 2017; Clapp and Anderson, 2019; Schoeberl et al., 2020, see also Chapter 4).

This chlorine driven ozone loss process could occur today above central North America in relation to stratospheric moistening through convective overshooting events during the North American Monsoon (NAM). Anderson et al. (2012) proposed a strong impact of heterogeneous chlorine activation on ozone and Anderson and Clapp (2018) simulated a maximal fractional ozone loss ranging between −2.5 and −67% (depending on the HCl mixing ratio) for the lower stratosphere between 12 km and 18 km assuming that conditions yielding heterogeneous chlorine activation such as low temperatures and a high water vapour mixing ratio of 20 ppmv are maintained for 14 days. In contrast, Schwartz et al. (2013) argue that conditions cold and moist enough for chlorine activation are very rare and are usually associated with low HCl and ozone amounts. Schoeberl et al. (2020) found that lowermost stratospheric water vapour is increased during the NAM caused by enhanced convection followed by advection in the monsoon

circulation. Simultaneously, the tropopause is uplifted reducing column ozone. However, this correlation between enhanced water vapour in the lowermost stratosphere and reduced column ozone is found to be dynamically driven with no evidence of substantial chemical ozone loss caused by chlorine activation. In comparison in the study of this thesis, chlorine activation would reduce ozone in the mixing layer by 0.1% (0.5% assuming 2 K lower temperatures). Nevertheless, ozone formation processes dominate ozone chemistry resulting in a net ozone formation simulated.

An enhancement of the stratospheric sulfate abundance, which causes ozone destruction in relation to heterogeneous chlorine activation, was mentioned in previous studies with respect to volcanic eruptions. Keim et al. (1996) combined laboratory measurements and observations and reported a removal layer for ozone caused by heterogeneous chlorine activation in the mid-latitudes around the tropopause subsequent to the Mt. Pinatubo eruption. Solomon et al. (1998) accentuated the relevance of heterogeneous chlorine chemistry by calculating a column ozone loss of ∼4% after the eruption of El Chicon and of ∼10% after the eruption of Mt. Pinatubo in 40-50°N not considering fluctuations of dynamical forcing between different years. However, Solomon et al. (1998) considered the entire ozone column, not only ozone loss in the lowermost stratosphere.

In this thesis, only air masses are considered that are close to the tropopause. Nevertheless, it is very unlikely that ozone loss caused by heterogeneous chlorine activation occurs at higher altitudes. As shown in Sec. 5.3.2 the likelihood is highest for a pressure level around 140 hPa, because chlorine activation is favoured at high pressures. Furthermore, temperatures increase with altitude reducing the likelihood for chlorine activation to occur. Since the stratospheric Cl_y concentration decreases because of the Montreal protocol, the impact of heterogeneous chlorine chemistry on ozone in the future is expected to be lower than for volcanic eruptions in the past (Klobas et al., 2017).

Comparing lowermost stratospheric ozone in the climate change and the geoengineering scenario, the overall ozone mixing ratio at the end of the 21st century is higher in the climate change scenario. There are other processes than heterogeneous chlorine activation, which are not investigated here and which would affect stratospheric ozone by applying sulfate geoengineering. For example, an increase in water vapour would

increase HO_x catalysed ozone destruction (Heckendorn et al., 2009), changes in radiation could affect oxygen and ozone photolysis. Furthermore, increased heterogeneous chemistry could enhance the NO_x concentration and gas phase chemistry could change due to higher stratospheric temperatures (Pitari et al., 2014). Since both chemistry and dynamics can affect stratospheric ozone at geoengineering conditions in multiple ways (e.g. Heckendorn et al., 2009; Pitari et al., 2014; Tilmes et al., 2009, 2014; Visioni et al., 2017b), further studies are necessary to assess the impact of geoengineering on stratospheric ozone (e.g. quantifying changes in HO_x induced ozone destruction or investigating the dynamical contribution to the difference in the ozone mixing ratio between the climate change and the geoengineering scenario).

5.5   Summary

In this chapter, the focus was on the potential occurrence of heterogeneous chlorine activation in the mixing layer between stratospheric and tropospheric air above central North America ($30.6-49.5°N$, $72.25-124.75°W$), which leads to catalytic ozone destruction known from the stratosphere during polar late winter and early spring (see Sec. 2.3.2). The likelihood for chlorine activation to occur and its impact on ozone in the mixing layer today and in future is determined by comparing chlorine activation thresholds calculated based on CLaMS box-model simulations with temperature and water vapour conditions in GLENS.

The GLENS mixing layer will warm and moisten in both future scenarios with a larger change in the geoengineering scenario (the median temperature is $\sim 2.5\,K$ higher in the years 2090–2100 with geoengineering than with climate change and the median water vapour mixing ratio is $\sim 6.5\,ppmv$ higher). The ozone mixing ratio increases in the mid-latitude mixing layer in GLENS assuming the climate change scenario, but is found to remain at today's level when sulfate geoengineering is applied. These differences may be due to changes in both atmospheric dynamics and chemistry in the lowermost stratosphere. For example, potential chemical effects are an increasing HO_x-mixing ratio, because of a higher water vapour mixing ratio, or differences in the NO_x/HNO_3-

or the ClO_x/HCl partitioning driven by changes in the heterogeneous and gas phase chemistry.

GLENS results in the mixing layer are analysed in comparison with SEAC[4]RS aircraft measurements. Most GLENS results and SEAC[4]RS measurements in the mixing layer range between 201–207 K and 5–8 ppmv H_2O. Thus, the water vapour and temperature conditions in GLENS have a good overall agreement with current observations. However, in the SEAC[4]RS measurements a higher fraction of air parcels with very low temperatures of 197–200 K compared to GLENS results are found. Based on this difference catalytic ozone loss is additionally investigated for 2 K lower temperatures than in the GLENS results.

A temperature and water vapour dependent threshold allows conditions to be defined which lead to and which do not lead to heterogeneous chlorine activation. The chlorine activation threshold analysed in this study, determines an upper temperature limit for chlorine activation to occur at a given water vapour mixing ratio. The chlorine activation thresholds depend on a variety of conditions. Increasing pressure, sulfate aerosol loading and ozone mixing ratio allow higher temperatures to cause chlorine activation. However, air parcels with higher pressures, sulfate aerosol loadings or ozone mixing ratios are usually warmer. Hence, shifting chlorine activation thresholds to higher temperatures (and thus leading to a broader range of conditions allowing chlorine activation) does not necessarily increase the likelihood for chlorine activation to occur, because the temperatures of air masses with the pressure and composition leading to these chlorine activation thresholds increase as well.

The likelihood for heterogeneous chlorine activation to occur and its impact on ozone in the mixing layer between tropospheric and stratospheric air masses is determined for several cases, which differ in the future scenario and in the considered years as further described in Tab. 5.1. The comparison of chlorine activation thresholds with GLENS results yields a likelihood for chlorine activation to occur of 1.0% for case C2010 and, assuming geoengineering, of 3.3% in case F2040 and 2.7% in case F2090. In contrast, the likelihood is negligible in the climate change scenario (0.1% in case C2040 and 0.0% in C2090). Assuming 2 K lower temperatures, the likelihood increases accounting for

3.7% in case C2010, 6.7% and 7.3% in the cases F2040 and F2090, respectively, and 1.4% and 0.2% in the cases C2040 and C2090, respectively. The likelihood of occurrence is higher at lower latitudes and at higher pressure levels (lower altitudes). However, in air masses in which chlorine activation may occur, usually a low ozone mixing ratio prevails. This fact contributes to the low impact of chlorine activation on ozone in the mixing layer.

The net chemical ozone change in the mixing layer is calculated here by combining the change in the ozone mixing ratio from 10 day CLaMS box-model simulations (final ozone−initial ozone) assuming specific water vapour and temperature conditions with the GLENS frequency distribution in the water vapour and temperature correlation. Normalizing this net chemical ozone change with the total initial ozone in the mixing layer yields the net relative ozone change, which occurs if chemical processes proceed for 10 days without being perturbed by mixing between air parcels. Thus, for conditions today (C2010 case) the net relative ozone change in the mixing layer accounts for +2.3%. Also in the future scenarios, a net chemical ozone formation occurs. In the climate change future scenario, ozone increases within 10 days by ∼2.5% in case C2040 and by ∼3.0% in case C2090. In the sulfate geoengineering scenario, the increase is somewhat less with 2.3% in case F2040 and 2.6% in case F2090.

However, only little ozone is destroyed caused by heterogeneous chlorine activation. The upper limit of ozone destruction in the stratospheric mixing layer caused by heterogeneous chlorine activation is 0.3% in the F2040 case, which is the case with the largest ozone destruction. Ozone destruction is larger in the subtropical latitude range (30–35°N). In that latitude range, 0.4% of ozone would be destroyed in the F2040 case and 0.2% in 44–49°N. Assuming 2 K lower temperatures, less ozone would be formed during 10 days without mixing. Additionally the upper boundary for the relative ozone destruction caused by heterogeneous chlorine activation in the mixing layer above central North America would increase to 0.8% in the F2040 case.

Finally, the impact of heterogeneous chlorine activation in the mixing layer on column ozone is estimated. Based on the conditions in GLENS, in all cases less than 0.1 DU of ozone (less than 0.1% of the ozone column) is destroyed caused by heterogeneous

chlorine activation in the mixing layer. Assuming 2 K lower temperatures, not more than 0.11 DU of ozone are destroyed for all latitude regions and all cases today and in the future scenarios with climate change as well as with additional sulfate geoengineering. In comparison in the Arctic polar winter in the year 2000, a volcanically clean year, 77±10 DU were destroyed between 110–30 hPa (Vogel et al., 2003) and Tilmes et al. (2008) have shown significantly larger ozone depletion in high polar latitudes with geoengineering.

In summary in this chapter is demonstrated, that heterogeneous chlorine activation affects ozone in the lowermost stratosphere in mid-latitudes, but that the impacts are very small. Sulfate geoengineering leads to a 2–3 times higher likelihood for the occurrence of chlorine activation. However, in the geoengineering case, which most likely yields chlorine activation, chlorine is activated with a probability of 3.3% (6.7% assuming 2 K lower temperatures) in the entire latitude region considered here. In all cases today and in future, less than 0.4% (0.9% assuming 2 K lower temperatures) of ozone in the mixing layer are destroyed caused by heterogeneous chlorine activation. An upper limit for total ozone column reduction of 0.11DU (less than 0.1% of column ozone) is deduced here. Thus according to the results of this chapter, the relevance of ozone destruction caused by heterogeneous chlorine activation in the mid-latitude mixing layer between stratospheric and tropospheric air is negligible with respect to the ozone column and small in the mixing layer even if sulfate geoengineering would be applied.

Chapter 6

Conclusions

This thesis assesses the risk of chlorine activation causing ozone destruction in the mid-latitude lowermost stratosphere in summer as a side effect of sulfate geoengineering. Chlorine driven ozone loss was first proposed to potentially occur in that region by Anderson et al. (2012) in combination with convective overshooting events or with the application of sulfate geoengineering. Both convective overshooting events leading to lowermost stratospheric moistening and the application of sulfate geoengineering causing an increase in the aerosol surface density are expected to promote heterogeneous chlorine activation and thus catalytic ozone destruction in mid-latitudes.

The large variety of sensitivity studies performed in this thesis yields a good understanding of the ozone loss mechanism potentially occurring in the mid-latitude lowermost stratosphere (Section 4.2). Besides pointing out the heterogeneous reaction

$$\text{ClONO}_2 + \text{HCl} \xrightarrow{\text{het.}} \text{Cl}_2 + \text{HNO}_3 \qquad\qquad (\text{R}\,21)$$

as the key step for chlorine catalysed ozone destruction, different reaction cycles are accentuated in this thesis to dominate catalytic ozone destruction in the mid-latitudes. Ozone loss in the polar early spring is mainly driven by the ClO-dimer cycle (C4) and the ClO-BrO cycle (C5). In comparison, in mid-latitudes ozone loss cycles (C6–C8) based on reaction R 19 ($\text{ClO} + \text{HO}_2 \rightarrow \text{HOCl} + \text{O}_2$) are likewise important. If heterogeneous chlorine activation and thus catalytic ozone loss occurs, is not only determined by the

temperatures, the water vapour mixing ratio and the sulfate aerosol abundance but depends also on the trace gas composition, in particular the Cl_y and the NO_y mixing ratio (Section 4.3).

From this understanding of the chemical ozone loss process, the threshold temperatures and water vapour mixing ratios, which promote heterogeneous chlorine activation in the lowermost stratosphere, are identified by calculating chlorine activation thresholds with CLaMS (Chemical Lagrangian Model of the Stratosphere). Comparing these chlorine activation thresholds with conditions prevailing in the lowermost stratosphere above North America in results of climate simulations (GLENS, Geoengineering Large Ensemble Simulations), the relevance of heterogeneous chlorine activation for ozone in the lowermost stratosphere for today and in future is determined for the first time. Therefore, lowermost stratospheric conditions are analysed at the beginning (2010-2020), the mid (2040–2050) and the end (2090–2100) of the 21st century considering a climate change scenario and a future scenario with the additional application of sulfate geoengineering (Chapter 5).

The likelihood for heterogeneous chlorine activation to occur is found to be 2–3 times higher in the sulfate geoengineering future scenario than for conditions today, while it is negligible in the climate change future scenario (Sec. 5.3.2). However even if geoengineering is applied, the likelihood for chlorine activation to occur above North America does not exceed 4.5% resulting in less than 0.4% of ozone in the lowermost stratosphere to be destroyed. Assuming an extreme case with 2 K lower temperatures than in the GLENS simulations, an upper limit for total ozone column reduction of 0.1 DU (<0.1%) is inferred (Sec. 5.3.5).

Subsequently, from the detailed sensitivity studies performed, a detailed understanding of the ozone loss process caused by heterogeneous chlorine activation potentially occurring in the mid-latitude lowermost stratosphere in summer is gained. This understanding allows the relevance of the considered ozone loss process for ozone in the mid-latitudes to be determined and hence the risk to be assessed, that this ozone loss process occurs as a side effect of geoengineering. The likelihood for heterogeneous chlorine activation and the resulting ozone loss in the mid-latitude lowermost stratosphere is found to

be low even if sulfate geoengineering is applied. Hence, this thesis demonstrates, that the risk of ozone loss in mid-latitudes caused by heterogeneous chlorine activation is negligible and thus not as high as it was estimated to be in the study of Anderson et al. (2012). These results can contribute to future assessments on the risks of sulfate geoengineering (e.g. by the World Meteorological Organization (WMO)).

However, sulfate geoengineering may have other side effects, which should be investigated before applying sulfate geoengineering. For example, an increase in the HO_x mixing ratio due to increasing stratospheric water vapour may affect ozone more than the process analysed in this thesis. Sulfate geoengineering may affect the Brewer-Dobson-circulation (BDC) and thus change atmospheric dynamics (e.g. Pitari et al., 2014; Visioni et al., 2017b). Furthermore, the distribution of precipitation is expected to be affected by sulfate geoengineering (e.g. Visioni et al., 2020) and legal aspects as well as the potential of moral conflicts should be considered before applying sulfate geoengineering. Although heterogeneous chlorine activation causing ozone destruction in mid-latitudes is a minor risk of sulfate geoengineering, further side effects have to be investigated to reduce the unknown risks of applying sulfate geoengineering.

Bibliography

Abalos, M., Randel, W. J., Kinnison, D. E., and Garcia, R. R.: Using the artificial tracer E90 to examine present and future UTLS tracer transport in WACCM, J. Atmos. Sci., 74, 3383–3403, doi:10.1175/JAS-D-17-0135.1, 2017.

Anderson, J. G. and Clapp, C. E.: Coupling free radical catalysis, climate change, and human health, Phys. Chem. Chem. Phys., 20, 10 569–10 587, doi:10.1039/C7CP08331A, 2018.

Anderson, J. G., Wilmouth, D. M., Smith, J. B., and Sayres, D. S.: UV dosage levels in summer: Increased risk of ozone loss from convectively injected water vapor, Science, 337, 835–839, doi:10.1126/science.1222978, 2012.

Anderson, J. G., Weisenstein, D. K., Bowman, K. P., Homeyer, C. R., Smith, J. B., Wilmouth, D. M., Sayres, D. S., Klobas, J. E., Leroy, S. S., Dykema, J. A., and Wofsy, S. C.: Stratospheric ozone over the United States in summer linked to observations of convection and temperature via chlorine and bromine catalysis, Proc. Natl. Acad. Sci., 114, E4905–E4913, doi:10.1073/pnas.1619318114, 2017.

Andersson, S. M., Martinsson, B. G., Friberg, J., Brenninkmeijer, C. A. M., Rauthe-Schoech, A., Hermann, M., van Velthoven, P. F. J., and Zahn, A.: Composition and evolution of volcanic aerosol from eruptions of Kasatochi, Sarychev and Eyjafjallajokull in 2008-2010 based on CARIBIC observations, Atmos. Chem. Phys., 13, 1781–1796, doi:10.5194/acp-13-1781-2013, 2013.

Ball, W. T., Alsing, J., Mortlock, D. J., Staehelin, J., Haigh, J. D., Peter, T., Tummon, F., Stübi, R., Stenke, A., Anderson, J., Bourassa, A., Davis, S. M., Degenstein,

D., Frith, S., Froidevaux, L., Roth, C., Sofieva, V., Wang, R., Wild, J., Yu, P., Ziemke, J. R., and Rozanov, E. V.: Evidence for a continuous decline in lower stratospheric ozone offsetting ozone layer recovery, Atmos. Chem. Phys., 18, 1379–1394, doi:10.5194/acp-18-1379-2018, 2018.

Ball, W. T., Alsing, J., Staehelin, J., Davis, S. M., Froidevaux, L., and Peter, T.: Stratospheric ozone trends for 1985–2018: sensitivity to recent large variability, Atmos. Chem. Phys., 19, 12 731–12 748, doi:10.5194/acp-19-12731-2019, 2019.

Barrera, A. J., Pedro Fernandez, R., Iglesias-Suarez, F., Alberto Cuevas, C., Lamarque, J.-F., and Saiz-Lopez, A.: Seasonal impact of biogenic very short-lived bromocarbons on lowermost stratospheric ozone between 60 degrees N and 60 degrees S during the 21st century, Atmos. Chem. Phys., 20, 8083–8102, doi:10.5194/acp-20-8083-2020, 2020.

Bates, D. R. and Nicolet, M.: The photochemistry of atmospheric water vapor, J. Geophys. Res., 55, 301–327, 1950.

Becker, G., Grooß, J.-U., McKenna, D. S., and Müller, R.: Stratospheric photolysis frequencies: Impact of an improved numerical solution of the radiative transfer equation, J. Atmos. Chem., 37, 217–229, doi:10.1023/A:1006468926530, 2000.

Berthet, G., Esler, J. G., and Haynes, P. H.: A Lagrangian perspective of the tropopause and the ventilation of the lowermost stratosphere, J. Geophys. Res., 112, D18102, 2007.

Berthet, G., Jégou, F., Catoire, V., Krysztofiak, G., Renard, J.-B., Bourassa, A. E., Degenstein, D. A., Brogniez, C., Dorf, M., Kreycy, S., Pfeilsticker, K., Werner, B., Lefèvre, F., Roberts, T. J., Lurton, T., Vignelles, D., Begue, N., Bourgeois, Q., Daugeron, D., Cartiert, M., Robert, C., Gaubicher, B., and Guimbaud, C.: Impact of a moderate volcanic eruption on chemistry in the lower stratosphere: balloon-borne observations and model calculations, Atmos. Chem. Phys., 17, 2229–2253, doi:10.5194/acp-17-2229-2017, 2017.

Birner, T. and Bönisch, H.: Residual circulation trajectories and transit times into the extratropical lowermost stratosphere, Atmos. Chem. Phys., 11, 817–827, doi:10.5194/acp-11-817-2011, 2011.

Bönisch, H., Engel, A., Birner, T., Hoor, P., Tarasick, D. W., and Ray, E. A.: On the structural changes in the Brewer-Dobson circulation after 2000, Atmos. Chem. Phys., 11, 3937–3948, doi:10.5194/acp-11-3937-2011, 2011.

Borrmann, S., Solomon, S., Dye, J. E., and Luo, B.: The potential of cirrus clouds for heterogeneous chlorine activation, Geophys. Res. Lett., 23, 2133–2136, doi:10.1029/96GL01957, 1996.

Borrmann, S., Solomon, S., Avallone, L., Toohey, D., and Baumgardner, D.: On the occurrence of ClO in cirrus clouds and volcanic aerosol in the tropopause region, Geophys. Res. Lett., 24, 2011–2014, doi:10.1029/97GL02053, 1997.

Bregman, A., Krol, M. C., Teyssèdre, H., Norton, W. A., Iwi, A., Chipperfield, M., Pitari, G., Sundet, J. K., and Lelieveld, J.: Chemistry-transport model comparison with ozone observations in the midlatitude lowermost stratosphere, J. Geophys. Res. A, 106, 17 479–17 496, doi:10.1029/2000JD900752, 2001.

Brewer, A. W.: Evidence for a world circulation provided by the measurements of helium and water vapour distribution in the stratosphere, Q. J. R. Meteorol. Soc., 75, 351–363, doi:10.1002/qj.49707532603, 1949.

Brown, P. N., Byrne, G. D., and Hindmarsh, A. C.: VODE: A variable coefficient ODE solver, SIAM J. Sci. Stat. Comput., 10, 1038–1051, doi:10.1137/0910062, 1989.

Butchart, N.: The Brewer-Dobson circulation, Rev. Geophys., 52, 157–184, doi:10.1002/2013RG000448, 2014.

Carver, G. D., Brown, P. D., and Wild, O.: The ASAD atmospheric chemistry integration package and chemical reaction database, Comput. Phys. Commun., 105, 197–215, doi:10.1016/S0010-4655(97)00056-8, 1997.

Chapman, S.: A theory of upper atmospheric ozone, Mem. Roy. Soc., 3, 103–109, 1930.

Chipperfield, M. P., Dhomse, S., Hossaini, R., Feng, W., Santee, M. L., Weber, M., Burrows, J. P., Wild, J. D., Loyola, D., and Coldewey-Egbers, M.: On the cause of recent variations in lower stratospheric ozone, Geophys. Res. Lett., 45, 5718–5726, doi:10.1029/2018GL078071, 2018.

Clapp, C. E. and Anderson, J. G.: Modeling the effect of potential nitric acid removal during convective injection of water vapor over the central united states on the chemical composition of the lower stratosphere, J. Geophys. Res. A, 124, 9743–9770, doi:10.1029/2018JD029703, 2019.

Crutzen, P. J.: The influence of nitrogen oxides on the atmospheric ozone content, Q. J. R. Meteorol. Soc., 96, 320–325, 1970.

Crutzen, P. J.: Albedo enhancements by stratospheric sulfur injections: a contribution to resolve a policy dilemma? An Editorial Essay, Clim. Change, 77, 211–219, 2006.

Crutzen, P. J., Müller, R., Brühl, C., and Peter, T.: On the potential importance of the gas phase reaction $CH_3O_2 + ClO \rightarrow ClOO + CH_3O$ and the heterogeneous reaction $HOCl + HCl \rightarrow H_2O + Cl_2$ in "ozone hole" chemistry, Geophys. Res. Lett., 19, 1113–1116, doi:10.1029/92GL01172, 1992.

Dameris, M., Loyola, D. G., Nützel, M., Coldewey-Egbers, M., Lerot, C., Romahn, F., and van Roozendael, M.: First description and classification of the ozone hole over the Arctic in boreal spring 2020, Atmos. Chem. Phys. Discuss., pp. 1–26, doi:10.5194/acp-2020-746, 2020.

Daniel, J. S., Solomon, S., Portmann, R. W., and Garcia, R. R.: Stratospheric ozone destruction: The importance of bromine relative to chlorine, J. Geophys. Res., 104, 23 871–23 880, doi:10.1029/1999JD900381, 1999.

Dee, D. P., Uppala, S. M., Simmons, A. J., Berrisford, P., Poli, P., Kobayashi, S., Andrae, U., Balmaseda, M. A., Balsamo, G., Bauer, P., Bechtold, P., Beljaars, A. C. M., van de Berg, L., Bidlot, J., Bormann, N., Delsol, C., Dragani, R., Fuentes, M., Geer, A. J., Haimberger, L., Healy, S. B., Hersbach, H., Hólm, E. V., Isaksen,

L., Kållberg, P., Köhler, M., Matricardi, M., McNally, A. P., Monge-Sanz, B. M., Morcrette, J.-J., Park, B.-K., Peubey, C., de Rosnay, P., Tavolato, C., Thépaut, J.-N., and Vitart, F.: The ERA-Interim reanalysis: configuration and performance of the data assimilation system, Q. J. R. Meteorol. Soc., 137, 553–597, doi:10.1002/qj.828, 2011.

Dessler, A., Schoeberl, M., Wang, T., Davis, S., and Rosenlof, K.: Stratospheric water vapor feedback, Proc. Natl. Acad. Sci., 110, 18 087–18 091, doi:10.1073/pnas. 1310344110, 2013.

Dessler, A. E. and Sherwood, S. C.: A matter of humidity, Science, 323, 1020–1021, doi:10.1126/science.1171264, 2009.

Dessler, A. E., Hintsa, E. J., Weinstock, E. M., Anderson, J. G., and Chan, K. R.: Mechanisms controlling water vapor in the lower stratosphere: "A tale of two stratospheres", J. Geophys. Res., 100, 23 167–23 172, doi:10.1029/95JD02455, 1995.

Drdla, K. and Müller, R.: Temperature thresholds for chlorine activation and ozone loss in the polar stratosphere, Ann. Geophys., 30, 1055–1073, doi:10.5194/ angeo-30-1055-2012, 2012.

Dutton, E. G. and Christy, J. R.: Solar radiative forcing at selected locations and evidence for global lower tropospheric cooling following the eruptions of El Chichón and Pinatubo, Geophys. Res. Lett., 19, 2313–2316, doi:10.1029/92GL02495, 1992.

Dykema, J. A., Keith, D. W., Anderson, J. G., and Weisenstein, D.: Stratospheric controlled pertubation experiment: a small-scale experiment to improve understanding of the risks of solar geoengineering, Phil. Trans. R. Soc. A, 372, 1–22, doi:10.1098/ rsta.2014.0059, 2014.

Elrod, M. J., Koch, R. E., Kim, J. E., and Molina, M.: HCl vapour pressures and reaction probabilities for $ClONO_2$+HCl on liquid H_2SO_4-HNO_3-HCl-H_2O solutions, Faraday Discuss., 100, 269–278, doi:10.1039/fd9950000269, 1995.

Evans, S. J., Toumi, R., Harries, J. E., Chipperfield, M. R., and Russell, J. M.: Trends in stratospheric humidity and the sensitivity of ozone to these trends, J. Geophys. Res. A, 103, 8715–8725, doi:10.1029/98JD00265, 1998.

Farman, J. C., Gardiner, B. G., and Shanklin, J. D.: Large losses of total ozone in Antarctica reveal seasonal ClO_x/NO_x interaction, Nature, 315, 207–210, doi: 10.1038/315207a0, 1985.

Fels, S. B., Mahlman, J. D., Schwarzkopf, M. D., and Sinclair, R. W.: Stratospheric Sensitivity to Perturbations in Ozone and Carbon Dioxide: Radiative and Dynamical Response, J. Aerosol Sci., 37, 2265–2297, doi:10.1175/1520-0469(1980)037⟨2265: SSTPIO⟩2.0.CO;2, 1980.

Fu, Q., Solomon, S., Pahlavan, H. A., and Lin, P.: Observed changes in Brewer–Dobson circulation for 1980–2018, Environ. Res. Lett., 14, 114 026, doi:10.1088/1748-9326/ ab4de7, 2019.

Gao, R. S., Ballard, J., Watts, L. A., Thornberry, T. D., Ciciora, S. J., McLaughlin, R. J., and Fahey, D. W.: A compact, fast UV photometer for measurement of ozone from research aircraft, Atmos. Meas. Tech., 5, 2201–2210, doi:10.5194/amt-5-2201-2012, 2012.

GHG Bulletin, ed.: WMO Greenhouse Gas Bulletin, GHG Bulletin No.10, WMO, `https://library.wmo.int/doc_num.php?explnum_id=7236`, last access: 19.09.2020, 2014.

Grant, W. B., Fishman, J., Browell, E. V., Brackett, V. G., Nganga, D., Minga, A., Cros, B., Veiga, R. E., Butler, C. F., Fenn, M. A., and Nowicki, G. D.: Observations of reduced ozone concentrations in the tropical stratosphere after the eruption of Mt. Pinatubo, Geophys. Res. Lett., 19, 1109–1112, doi:10.1029/92GL01153, 1992.

Grenfell, J. L., Lehmann, R., Mieth, P., Langematz, U., and Steil, B.: Chemical reaction pathways affecting stratospheric and mesospheric ozone, J. Geophys. Res. A, 111, doi:10.1029/2004JD005713, 2006.

Grooß, J.-U. and Müller, R.: Simulation of the record Arctic stratospheric ozone
  depletion in 2020, J. Geophys. Res. A, submitted, 2020.

Grooß, J.-U., Günther, G., Konopka, P., Müller, R., McKenna, D. S., Stroh, F.,
  Vogel, B., Engel, A., Müller, M., Hoppel, K., Bevilacqua, R., Richard, E., Webster,
  C. R., Elkins, J. W., Hurst, D. F., Romashkin, P. A., and Baumgardner, D. G.:
  Simulation of ozone depletion in spring 2000 with the Chemical Lagrangian Model of
  the Stratosphere (CLaMS), J. Geophys. Res., 107, 8295, doi:10.1029/2001JD000456,
  2002.

Grooß, J.-U., Brautzsch, K., Pommrich, R., Solomon, S., and Müller, R.: Stratospheric
  ozone chemistry in the Antarctic: What controls the lowest values that can be
  reached and their recovery?, Atmos. Chem. Phys., 11, 12 217–12 226, doi:10.5194/
  acp-11-12217-2011, 2011.

Grooß, J.-U., Engel, I., Borrmann, S., Frey, W., Günther, G., Hoyle, C. R., Kivi,
  R., Luo, B. P., Molleker, S., Peter, T., Pitts, M. C., Schlager, H., Stiller, G.,
  Vömel, H., Walker, K. A., and Müller, R.: Nitric acid trihydrate nucleation and
  denitrification in the Arctic stratosphere, Atmos. Chem. Phys., 14, 1055–1073, doi:
  10.5194/acp-14-1055-2014, 2014.

Grooß, J.-U., Müller, R., Spang, R., Tritscher, I., Wegner, T., Chipperfield, M. P., Feng,
  W., Kinnison, D. E., and Madronich, S.: On the discrepancy of HCl processing in
  the core of the wintertime polar vortices, Atmos. Chem. Phys., 18, 8647–8666, 2018.

Haagen-Smit, A. H.: Chemistry and physiology of the Los Angeles photochemical smog,
  Ind. Eng. Chem., 44, 1342–1346, doi:10.1021/ie50510a045, 1952.

Hanisco, T. F., Moyer, E. J., Weinstock, E. M., Clair, J. M. S., Sayres, D. S., Smith,
  J. B., Lockwood, R., Anderson, J. G., Dessler, A. E., Keutsch, F. N., Spackman,
  J. R., Read, W. G., and Bui, T. P.: Observations of deep convective influence on
  stratospheric water vapor and its isotopic composition, Geophys. Res. Lett., 34,
  L04814, doi:10.1029/2006GL027899, 2007.

Hanson, D. R.: Reaction of $ClONO_2$ with H_2O and HCl in sulfuric acid and $HNO_3/H_2SO_4/H_2O$ mixtures, J. Phys. Chem. A, 102, 4794–4807, doi:10.1021/jp972767s, 1998.

Hanson, D. R. and Ravishankara, A. R.: Reactive Uptake of $ClONO_2$ onto Sulfuric Acid Due to Reaction with HCl and H_2O, J. Phys. Chem., 98, 5728–5735, 1994.

Heckendorn, P., Weisenstein, D., Fueglistaler, S., Luo, B. P., Rozanov, E., Schraner, M., Thomason, L. W., and Peter, T.: The impact of geoengineering aerosols on stratospheric temperature and ozone, Environ. Res. Lett., 4, 045 108, doi:10.1088/1748-9326/4/4/045108, 2009.

Herman, R. L., Ray, E. A., Rosenlof, K. H., Bedka, K. M., Schwartz, M. J., Read, W. G., Troy, R. F., Chin, K., Christensen, L. E., Fu, D., Stachnik, R. A., Bui, T. P., and Dean-Day, J. M.: Enhanced stratospheric water vapor over the summertime continental United States and the role of overshooting convection, Atmos. Chem. Phys., 17, 6113, doi:10.5194/acp-17-6113-2017, 2017.

Hoinka, K. P.: The tropopause: discovery, definition and demarcation, Meteorol. Z., 6, 281–303, doi:10.1127/metz/6/1997/281, 1997.

Holton, J. R., Haynes, P., McIntyre, M. E., Douglass, A. R., Rood, R. B., and Pfister, L.: Stratosphere-troposphere exchange, Rev. Geophys., 33, 403–439, doi:10.1029/95RG02097, 1995.

Homeyer, C. R., Pan, L. L., Dorsi, S. W., Avallone, L. M., Weinheimer, A. J., O'Brien, A. S., DiGangi, J. P., Zondlo, M. A., Ryerson, T. B., Diskin, G. S., and Campos, T. L.: Convective transport of water vapor into the lower stratosphere observed during double-tropopause events, J. Geophys. Res., 119, 10 941–10 958, doi:10.1002/2014JD021485, 2014.

Hurrell, J. W., Holland, M. M., Gent, P. R., Ghan, S., Kay, J. E., Kushner, P. J., Lamarque, J.-F., Large, W. G., Lawrence, D., Lindsay, K., et al.: The community earth system model: a framework for collaborative research, Bull. Am. Meteorol. Soc., 94, 1339–1360, doi:10.1175/BAMS-D-12-00121.1, 2013.

Iglesias-Suarez, F., Young, P. J., and Wild, O.: Stratospheric ozone change and related climate impacts over 1850–2100 as modelled by the ACCMIP ensemble, Atmos. Chem. Phys., 16, 343–363, doi:10.5194/acp-16-343-2016, 2016.

Jing, F., Chauhan, A., Singh, R. P., and Dash, P.: Changes in Atmospheric, Meteorological, and Ocean Parameters Associated with the 12 January 2020 Taal Volcanic Eruption, Remote Sensing, 12, doi:10.3390/rs12061026, 2020.

Johnson, D. G., Traub, W. A., Chance, K. V., Jucks, K. W., and Stachnik, R. A.: Estimating the abundance of ClO from simultaneous remote sensing measurements of HO2, OH, and HOCl, Geophys. Res. Lett., 22, 1869–1871, doi:10.1029/95GL01249, 1995.

Johnston, H. and Kinnison, D.: Methane photooxidation in the atmosphere: Contrast between two methods of analysis, J. Geophys. Res., 103, 21 967–21 984, doi:10.1029/98JD01213, 1998.

Jones, A. E. and Shanklin, J. D.: Continued decline of total ozone over Halley, Antarctica, since 1985, Nature, 376, 409–411, doi:10.1038/376409a0, 1995.

Keim, E. R., Fahey, D. W., Negro, L. A. D., Woodbridge, E. L., Gao, R., Wennberg, P. O., Cohen, R. C., Stimpfle, R. M., Kelly, K. K., Hintsa, E. J., Wilson, J. C., Jonsson, H. H., Dye, J. E., Baumgardner, D. G., Kawa, S. R., Salawitch, R. J., Proffitt, M. H., Loewenstein, M., Podolske, J. R., and Chan, K. R.: Observations of large reductions in the NO/NO_y ratio near the mid-latitude tropopause and the role of heterogeneous chemistry, Geophys. Res. Lett., 23, 3223–3226, doi:10.1029/96GL02593, 1996.

Klobas, J. E., Wilmouth, D. M., Weisenstein, D. K., Anderson, J. G., and Salawitch, R. J.: Ozone depletion following future volcanic eruptions, Geophys. Res. Lett., 44, 7490–7499, doi:10.1002/2017GL073972, 2017.

Koenig, T. K., Volkamer, R., Baidar, S., Dix, B., Wang, S., Anderson, D. C., Salawitch, R. J., Wales, P. A., Cuevas, C. A., Fernandez, R. P., Saiz-Lopez, A., Evans, M. J.,

Sherwen, T., Jacob, D. J., Schmidt, J., Kinnison, D., Lamarque, J.-F., Apel, E. C., Bresch, J. C., Campos, T., Flocke, F. M., Hall, S. R., Honomichl, S. B., Hornbrook, R., Jensen, J. B., Lueb, R., Montzka, D. D., Pan, L. L., Reeves, J. M., Schauffler, S. M., Ullmann, K., Weinheimer, A. J., Atlas, E. L., Donets, V., Navarro, M. A., Riemer, D., Blake, N. J., Chen, D., Huey, L. G., Tanner, D. J., Hanisco, T. F., and Wolfe, G. M.: BrO and inferred Br_y profiles over the western Pacific: relevance of inorganic bromine sources and a Br_y minimum in the aged tropical tropopause layer, Atmos. Chem. Phys., 17, 15 245–15 270, doi:10.5194/acp-17-15245-2017, 2017.

Konopka, P., Steinhorst, H.-M., Grooß, J.-U., Günther, G., Müller, R., Elkins, J. W., Jost, H.-J., Richard, E., Schmidt, U., Toon, G., and McKenna, D. S.: Mixing and Ozone Loss in the 1999-2000 Arctic Vortex: Simulations with the 3-dimensional Chemical Lagrangian Model of the Stratosphere (CLaMS), J. Geophys. Res., 109, D02315, doi:10.1029/2003JD003792, 2004.

Kovalenko, L. J., Jucks, K. W., Salawitch, R. J., Toon, G. C., Blavier, J.-F., Johnson, D. G., Kleinböhl, A., Livesey, N. J., Margitan, J. J., Pickett, H. M., Santee, M. L., Sen, B., Stachnik, R. A., and Waters, J. W.: Observed and modeled HOCl profiles in the midlatitude stratosphere: Implication for ozone loss, Geophys. Res. Lett., 34, doi:10.1029/2007GL031100, 2007.

Kravitz, B., MacMartin, D. G., Wang, H., and Rasch, P. J.: Geoengineering as a design problem, Earth Syst. Dynam., 7, 469–497, doi:10.5194/esd-7-469-2016, 2016.

Kravitz, B., MacMartin, D. G., Mills, M. J., Richter, J. H., Tilmes, S., Lamarque, J.-F., Tribbia, J. J., and Vitt, F.: First simulations of designing stratospheric sulfate aerosol geoengineering to meet multiple simultaneous climate objectives, J. Geophys. Res., 122, 12 616–12 634, doi:10.1002/2017JD026874, 2017.

Labitzke, K. and McCormick, M. P.: Stratospheric temperature increases due to Pinatubo aerosols, Geophys. Res. Lett., 19, 207–210, doi:10.1029/91GL02940, 1992.

Lacis, A., Hansen, J., and Sato, M.: Climate forcing by stratospheric aerosols, Geophys. Res. Lett., 19, 1607–1610, doi:10.1029/92GL01620, 1992.

Lacis, A., Schmidt, G., Rind, D., and Ruedy, R.: Atmospheric CO_2: Principal control knob governing Earth's temperature, Science, 330, 356–359, doi:10.1126/science.1190653, 2010.

Lee, K.-O., Dauhut, T., Chaboureau, J.-P., Khaykin, S., Krämer, M., and Rolf, C.: Convective hydration in the tropical tropopause layer during the StratoClim aircraft campaign: pathway of an observed hydration patch, Atmos. Chem. Phys., 19, 11 803–11 820, doi:10.5194/acp-19-11803-2019, 2019.

Lelieveld, J., Bregman, B., Arnold, F., Bürger, V., Crutzen, P. J., Fischer, H., Waibel, A., Siegmund, P., and van Velthoven, P. F. J.: Chemical perturbation of the lowermost stratosphere through exchange with the troposphere, Geophys. Res. Lett., 24, 603–606, doi:10.1029/97GL00255, 1997.

LeTexier, H., Solomon, S., and Garcia, R. R.: The role of molecular hydrogen and methane oxidation in the water vapour budget of the stratosphere, Q. J. R. Meteorol. Soc., 114, 281 – 295, doi:10.1002/qj.49711448002, 1988.

Llanillo, P., Jones, P. D., and Von Glasow, R.: The influence of stratospheric sulphate aerosol deployment on the surface air temperature and the risk of an abrupt global warming, Atmosphere, 1, 62–84, doi:10.3390/atmos1010062, 2010.

Logan, J. A.: An analysis of ozonesonde data for the lower stratosphere: Recommendations for testing models, J. Geophys. Res. A, 104, 16 151–16 170, doi:10.1029/1999JD900216, 1999.

Luo, B., Krieger, U. K., and Peter, T.: Densities and refractive indices of $H_2SO_4/HNO_3/H_2O$ solutions to stratospheric temperatures, Geophys. Res. Lett., 23, 3707–3710, doi:10.1029/96GL03581, 1996.

MacMartin, D. G., Kravitz, B., Keith, D. W., and Jarvis, A.: Dynamics of the coupled human-climate system resulting from closed-loop control of solar geoengineering, Clim. Dyn., 43, 243–258, doi:10.1007/s00382-013-1822-9, 2014.

MacMartin, D. G., Kravitz, B., Tilmes, S., Richter, J. H., Mills, M. J., Lamarque, J.-F., Tribbia, J. J., and Vitt, F.: The Climate Response to Stratospheric Aerosol Geoengineering can be Tailored Using Multiple Injection Locations, J. Geophys. Res., 122, 12 574–12 590, doi:10.1002/2017JD026868, 2017.

Manney, G. L., Livesey, N. J., Santee, M. L., Froidevaux, L., Lambert, A., Lawrence, Z. D., Millán, L. F., Neu, J. L., Read, W. G., Schwartz, M. J., and Fuller, R. A.: Record-low Arctic stratospheric ozone in 2020: MLS observations of chemical processes and comparisons with previous extreme winters, Geophys. Res. Lett., p. e2020GL089063, doi:10.1029/2020GL089063, 2020.

Marsh, D. R., Mills, M. J., Kinnison, D. E., Lamarque, J.-F., Calvo, N., and Polvani, L. M.: Climate change from 1850 to 2005 simulated in CESM1(WACCM), Journal of Climate, 26, 7372–7390, doi:10.1175/JCLI-D-12-00558.1, 2013.

McCormick, M. P., Thomason, L. W., and Trepte, C. R.: Atmospheric effects of the Mt Pinatubo eruption, Nature, 373, 399–404, doi:10.1038/373399a0, 1995.

McElroy, M. B., Salawitch, R. J., Wofsy, S. C., and Logan, J. A.: Reductions of antarctic ozone due to synergistic interactions of chlorine and bromine, Nature, 321, 759–762, doi:10.1038/321759a0, 1986.

McKenna, D. S., Grooß, J.-U., Günther, G., Konopka, P., Müller, R., Carver, G., and Sasano, Y.: A new Chemical Lagrangian Model of the Stratosphere (CLaMS): 2. Formulation of chemistry scheme and initialization, J. Geophys. Res., 107, 4256, doi:10.1029/2000JD000113, 2002a.

McKenna, D. S., Konopka, P., Grooß, J.-U., Günther, G., Müller, R., Spang, R., Offermann, D., and Orsolini, Y.: A new Chemical Lagrangian Model of the Stratosphere (CLaMS): 1. Formulation of advection and mixing, J. Geophys. Res., 107, 4309, doi:10.1029/2000JD000114, 2002b.

Meier, R. R., Anderson, D. E., J., and Nicolet, M.: Radiation field in the troposphere and stratosphere from 240-1000 nm -I: General analysis, Planet Space Sci, 30, 923–933, doi:10.1016/0032-0633(82)90134-9, 1982.

Meyer, J., Rolf, C., Schiller, C., Rohs, S., Spelten, N., Afchine, A., Zöger, M., Sitnikov, N., Thornberry, T. D., Rollins, A. W., Bozóki, Z., Tátrai, D., Ebert, V., Kühnreich, B., Mackrodt, P., Möhler, O., Saathoff, H., Rosenlof, K. H., and Krämer, M.: Two decades of water vapor measurements with the FISH fluorescence hygrometer: a review, Atmos. Chem. Phys., 15, 8521–8538, doi:10.5194/acp-15-8521-2015, 2015.

Mills, M. J., Schmidt, A., Easter, R., Solomon, S., Kinnison, D. E., Ghan, S. J., Neely III, R. R., Marsh, D. R., Conley, A., Bardeen, C. G., and Gettelman, A.: Global volcanic aerosol properties derived from emissions, 1990–2014, using CESM1(WACCM), J. Geophys. Res. A, 121, 2332–2348, doi:10.1002/2015JD024290, 2016.

Mills, M. J., Richter, J. H., Tilmes, S., Kravitz, B., MacMartin, D. G., Glanville, A. A., Tribbia, J. J., Lamarque, J.-F., Vitt, F., Schmidt, A., et al.: Radiative and chemical response to interactive stratospheric sulfate aerosols in fully coupled CESM1 (WACCM), J. Geophys. Res. A, 122, 13 061–13 078, doi:10.1002/2017JD027006, 2017.

Molina, L. T. and Molina, M. J.: Production of Cl_2O_2 from the self-reaction of the ClO radical, J. Phys. Chem., 91, 433–436, doi:10.1021/j100286a035, 1987.

Molina, L. T., Molina, M. J., Stachnik, R. A., and Tom, R. D.: An upper limit to the rate of the hydrogen chloride + $ClONO_2$ reaction, J. Phys. Chem., 89, 3779–3781, doi:10.1021/j100264a003, 1985.

Molina, M. J., Tso, T.-L., Molina, L. T., and Wang, F. C.-Y.: Antarctic stratospheric chemistry of chlorine nitrate, hydrogen chloride, and ice: Release of active chlorine, Science, 238, 1253–1257, doi:10.1126/science.238.4831.1253, 1987.

Müller, R., Grooß, J.-U., Lemmen, C., Heinze, D., Dameris, M., and Bodeker, G.: Simple measures of ozone depletion in the polar stratosphere, Atmos. Chem. Phys., 8, 251–264, doi:10.5194/acp-8-251-2008, 2008.

Müller, R., Grooß, J.-U., Zafar, A., Robrecht, S., and Lehmann, R.: The maintenance of elevated active chlorine levels in the Antarctic lower stratosphere through HCl null cycles, Atmos. Chem. Phys., 18, 2985–2997, doi:10.5194/acp-18-2985-2018, 2018.

Navarro, M. A., Saiz-Lopez, A., Cuevas, C. A., Fernandez, R. P., Atlas, E., Rodriguez-Lloveras, X., Kinnison, D., Lamarque, J.-F., Tilmes, S., Thornberry, T., Rollins, A., Elkins, J. W., Hintsa, E. J., and Moore, F. L.: Modeling the inorganic bromine partitioning in the tropical tropopause layer over the eastern and western Pacific Ocean, Atmos. Chem. Phys., 17, 9917–9930, doi:10.5194/acp-17-9917-2017, 2017.

Niemeier, U. and Timmreck, C.: What is the limit of climate engineering by stratospheric injection of SO_2?, Atmos. Chem. Phys., 15, 9129–9141, doi:10.5194/acp-15-9129-2015, 2015.

Noël, S., Weigel, K., Bramstedt, K., Rozanov, A., Weber, M., Bovensmann, H., and Burrows, J. P.: Water vapour and methane coupling in the stratosphere observed using SCIAMACHY solar occultation measurements, Atmos. Chem. Phys., 18, 4463–4476, doi:10.5194/acp-18-4463-2018, 2018.

Oman, L. D., Waugh, D. W., Kawa, S. R., Stolarski, R. S., Douglass, A. R., and Newman, P. A.: Mechanisms and feedback causing changes in upper stratospheric ozone in the 21st century, J. Geophys. Res. A, 115, doi:10.1029/2009JD012397, 2010.

Pachauri, R., Meyer, L., and IPCC core writing team, eds.: IPCC 2014: Climate Change 2014: Synthesis Report. Contribution of workinggGroups I, II and III to the fifth assessment report of the Intergovernmental Panel on Climate Change, Cambridge University Press, Geneva, Switzerland, 2014.

Pan, L. L., Solomon, S., Randel, W., Lamarque, J.-F., Hess, P., Gille, J., Chiou, E.-W., and McCormick, M. P.: Hemispheric asymmetries and seasonal variations of the lowermost stratospheric water vapor and ozone derived from SAGE II data, J. Geophys. Res., 102, doi:10.1029/97JD02778, 1997.

Pan, L. L., Randel, W. J., Gary, B. L., Mahoney, M. J., and Hintsa, E. J.: Definitions and sharpness of the extratropical tropopause: A trace gas perspective, J. Geophys. Res., 109, doi:10.1029/2004JD004982, 2004.

Pan, L. L., Bowman, K. P., Atlas, E. L., Wofsy, S. C., Zhang, F., Bresch, J. F., Ridley, B. A., Pittman, J. V., Homeyer, C. R., Romashkin, P., and Cooper, W. A.:

The Stratosphere-Troposphere Analyses of Regional Transport 2008 (START08) experiment, Bull. Am. Meteorol. Soc., 91, 327–342, doi:10.1175/2009BAMS2865.1, 2010.

Pitari, G., Rizi, V., Ricciardulli, L., and Visconti, G.: High-Speed civil transport impact: Role of sulfate, nitric acid trihydrate, and ice aerosols studied with a two-dimensional model including aerosol physics, J. Geophys. Res., 98, 23 141–23 164, doi:10.1029/93JD02600, 1993.

Pitari, G., Aquila, V., Kravitz, B., Robock, A., Watanabe, S., Luca, N. D., Genova, G. D., Mancini, E., Tilmes, S., and Cionni, I.: Stratospheric ozone response to sulfate geoengineering: Results from the Geoengineering Model Intercomparison Project (GeoMIP), J. Geophys. Res., 119, 2629–2653, doi:10.1002/2013JD020566, 2014.

Pitari, G., Visioni, D., Mancini, E., Cionni, I., Di Genova, G., and Gandolfi, I.: Sulfate aerosols from non-explosive volcanoes: chemical-radiative effects in the troposphere and lower stratosphere, Atmosphere, 7, 85, doi:10.3390/atmos7070085, 2016.

Ploeger, F., Konopka, P., Günther, G., Grooß, J.-U., and Müller, R.: Impact of the vertical velocity scheme on modeling transport across the tropical tropopause layer, J. Geophys. Res., 115, D03301, doi:10.1029/2009JD012023, 2010.

Ploeger, F., Abalos, M., Birner, T., P.Konopka, Legras, B., Müller, R., and Riese, M.: Quantifying the effects of mixing and residual circulation on trends of stratospheric mean age of air, Geophys. Res. Lett., 42, 2047–2054, doi:10.1002/2014GL062927, 2015a.

Ploeger, F., Riese, M., Haenel, F., P.Konopka, Müller, R., and Stiller, G.: Variability of stratospheric mean age of air and of the local effects of residual circulation and eddy mixing, J. Geophys. Res., 120, 716–733, doi:10.1002/2014JD022468, 2015b.

Plumb, R. A.: Stratospheric transport, J. Meteorol. Soc. Jpn., 80, 793–809, doi: 10.2151/jmsj.80.793, 2002.

Portmann, R. W., Daniel, J. S., and Ravishankara, A. R.: Stratospheric ozone depletion due to nitrous oxide: influences of other gases, Phil. Trans. R. Soc. B, 367, 1256–1264, doi:doi:10.1098/rstb.2011.0377, 2012.

Poshyvailo, L., Müller, R., Konopka, P., Günther, G., Riese, M., Podglajen, A., and Ploeger, F.: Sensitivities of modelled water vapour in the lower stratosphere: temperature uncertainty, effects of horizontal transport and small-scale mixing, Atmos. Chem. Phys., 18, 8505–8527, doi:10.5194/acp-18-8505-2018, 2018.

Prather, M. J.: More rapid ozone depletion through the reaction of HOCl with HCl on polar stratospheric clouds, Nature, 355, 534–537, doi:10.1038/355534a0, 1992.

Ramaswamy, V., Chanin, M. L., Angell, J., Barnett, J., Gaffen, D., Gelman, M., Keckhut, P., Koshelkov, Y., Labitzke, K., Lin, J., O'Neill, A., Nash, J., Randel, W., Rood, R., Shine, K., Shiotani, M., and Swinbank, R.: Stratospheric temperature trends: Observations and model simulations, Rev. Geophys., 39, 71–122, doi:10.1029/ 1999RG000065, 2001.

Randel, W. J., Wu, F., Gettelman, A., Russell, J., Zawodny, J., and Oltmans, S.: Seasonal variation of water vapor in the lower stratosphere observed in Halogen Occultation Experiment data, J. Geophys. Res., 106, D13, doi:10.1029/2001JD900048, 2001.

Randel, W. J., Wu, F., Oltmans, S. J., Rosenlof, K. H., and Nodoluha, G. E.: Interannual changes of stratospheric water vapor and correlations with tropical tropopause temperatures, J. Atmos. Sci., 61, 2133–2148, doi:10.1175/1520-0469(2004)061⟨2133: ICOSWV⟩2.0.CO;2, 2004.

Randeniya, L. K., Vohralik, P. F., and Plumb, I. C.: Stratospheric ozone depletion at northern midlatitudes in the 21st century: The importance of future concentrations of greenhouse gases nitrous oxide and methane, Geophys. Res. Lett., 29, 1051, doi:10.1029/2001GL014295, 2002.

Rasch, P. J., Crutzen, P. J., and Coleman, D. B.: Exploring the geoengineering of

climate using stratospheric sulfate aerosols: The role of particle size, Geophys. Res. Lett., 35, L02809, doi:10.1029/2007GL032179, 2008.

Ravishankara, A. R.: Water vapor in the lower stratosphere, Science, 337, 809–810, doi:10.1126/science.1227004, 2012.

Ravishankara, A. R., Daniel, J. S., and Portmann, R. W.: Nitrous oxide (N_2O): The dominant ozone-depleting substance emitted in the 21st century, Science, 326, 123–125, doi:10.1126/science.1176985, 2009.

Reader, M. C., Plummer, D. A., Scinocca, J. F., and Shepherd, T. G.: Contributions to twentieth century total column ozone change from halocarbons, tropospheric ozone precursors, and climate change, Geophys. Res. Lett., 40, 6276–6281, doi: 10.1002/2013GL057776, 2013.

Revell, L. E., Stenke, A., Rozanov, E., Ball, W., Lossow, S., and Peter, T.: The role of methane in projections of 21st century stratospheric water vapour, Atmos. Chem. Phys., 16, 13 067–13 080, doi:10.5194/acp-16-13067-2016, 2016.

Richter, J. H., Tilmes, S., Mills, M. J., Tribbia, J. J., Kravitz, B., MacMartin, D. G., Vitt, F., and Lamarque, J.-F.: Stratospheric dynamical response and ozone feedbacks in the presence of SO_2 injections, J. Geophys. Res. A, 122, 12 557–12 573, doi: 10.1002/2017JD026912, 2017.

Riese, M., Ploeger, F., Rap, A., Vogel, B., Konopka, P., Dameris, M., and Forster, P.: Impact of uncertainties in atmospheric mixing on simulated UTLS composition and related radiative effects, J. Geophys. Res., 117, D16305, doi:10.1029/2012JD017751, 2012.

Rind, D., Suozzo, R., Balachandran, N. K., and Prather, M. J.: Climate change and the middle atmosphere. Part I: The doubled CO_2 climate, J. Atmos. Sci., 47, 475 – 494, 1990.

Robock, A., Marquardt, A., Kravitz, B., and Stenchikov, G.: Benefits, risks, and costs

of stratospheric geoengineering, Geophys. Res. Lett., 36, doi:10.1029/2009GL039209, 2009.

Robrecht, S.: Chemische Prozesse in der antarktischen Stratosphäre bei extrem niedriger Ozonkonzentration, Master thesis, Bielefeld University, 2016.

Rohs, S., Schiller, C., Riese, M., Engel, A., Schmidt, U., Wetter, T., Levin, I., Nakazawa, T., and Aoki, S.: Long-term changes of methane and hydrogen in the stratosphere in the period 1978–2003 and their impact on the abundance of stratospheric water vapor, J. Geophys. Res., 111, D14315, doi:10.1029/2005JD006877, 2006.

Rollins, A. W., Thornberry, T. D., Gao, R. S., Smith, J. B., Sayres, D. S., Sargent, M. R., Schiller, C., Krämer, M., Spelten, N., Hurst, D. F., Jordan, A. F., Hall, E. G., Vomel, H., Diskin, G. S., Podolske, J. R., Christensen, L. E., Rosenlof, K. H., and Fahey, D. W.: Evaluation of UT/LS hygrometer accuracy by intercomparison during the NASA MACPEX mission, J. Geophys. Res. A, 119, 1915–1935, doi: 10.1002/2013JD020817, 2014.

Rosenlof, K. H., Tuck, A. F., Kelly, K. K., Russell III, J. M., and McCormick, M. P.: Hemispheric asymmetries in the water vapor and inferences about transport in the lower stratosphere, J. Geophys. Res., 102, 13 213–13 234, doi:10.1029/97JD00873, 1997.

Salawitch, R. J., Fahey, D. W., Hegglin, M. I., McBride, L. A., Tribett, W. R., and Doherty, S. J.: Twenty Questions and Answers About the Ozone Layer: 2018 Update, Scientific Assessment of Ozone Depletion: 2018, World Meterorological Orgaization, Geneva, Switzerland, 2019.

Sander, S. P., Friedl, R. R., Barker, J. R., Golden, D. M., Kurylo, M. J., Wine, P. H., Abbatt, J. P. D., Burkholder, J. B., Kolb, C. E., Moortgat, G. K., Huie, R. E., and Orkin, V. L.: Chemical kinetics and photochemical data for use in atmospheric studies, JPL Publication 10-6, 2011.

Schiller, C., Grooß, J.-U., Konopka, P., Plöger, F., Silva dos Santos, F. H., and Spelten,

N.: Hydration and dehydration at the tropical tropopause, Atmos. Chem. Phys., 9, 9647–9660, doi:10.5194/acp-9-9647-2009, 2009.

Schoeberl, M. R., Bhartia, P. K., Hilsenrath, E., and Torres, O.: Tropical ozone loss following the eruption of Mt. Pinatubo, Geophys. Res. Lett., 20, 29–32, doi: 10.1029/92GL02637, 1993.

Schoeberl, M. R., Pfister, L., Wang, T., Kummer, J., Dessler, A. E., and Yu, W.: Erythemal radiation, column ozone, and the north american monsoon, J. Geophys. Res. A, 125, e2019JD032 283, doi:10.1029/2019JD032283, 2020.

Schwartz, M. J., Read, W. G., Santee, M. L., Livesesy, N. J., Froidevaux, L., Lamert, A., and Manney, G. L.: Convectively injected water vapor in the North American summer lowermost stratosphere, Geophys. Res. Lett., 40, 2316–2321, doi:10.1002/grl.50421, 2013.

Seinfeld, J. H. and Pandis, S. N.: Atmospheric Chemistry and Physics : from air pollution to climate change, John Wiley and Sons, 2nd edn., 2006.

Shi, Q., Jayne, J. T., Kolb, C. E., Worsnop, D. R., and Davidovits, P.: Kinetic model for reaction of $ClONO_2$ with H_2O and HCl and HOCl with HCl in sulfuric acid solutions, J. Geophys. Res., 106, 24 259–24 274, doi:10.1029/2000JD000181, 2001.

Shindell, D. T.: Climate and ozone response to increased stratospheric water vapor, Geophys. Res. Lett., 28, 1551–1554, doi:10.1029/1999GL011197, 2001.

Smith, J. B., Wilmouth, D. M., Bedka, K. M., Bowman, K. P., Homeyer, C. R., Dykema, J. A., Sargent, M. R., Clapp, C. E., Leroy, S. S., Sayres, D. S., Dean-Day, J. M., Bui, T. P., and Anderson, J. G.: A case study of convectively sourced water vapor observed in the overworld stratosphere over the United States, J. Geophys. Res., 122, 9529–9554, doi:10.1002/2017JD026831, 2017.

Solomon, S.: Stratospheric ozone depletion: A review of concepts and history, Rev. Geophys., 37, 275–316, doi:10.1029/1999RG900008, 1999.

Solomon, S., Garcia, R. R., Rowland, F. S., and Wuebbles, D. J.: On the depletion of Antarctic ozone, Nature, 321, 755–758, doi:10.1038/321755a0, 1986.

Solomon, S., Borrmann, S., Garcia, R. R., Portmann, R., Thomason, L., Poole, L. R., Winker, D., and McCormick, M. P.: Heterogeneous chlorine chemistry in the tropopause region, J. Geophys. Res., 102, 21 411–21 429, doi:10.1029/97JD01525, 1997.

Solomon, S., Portmann, R. W., Garcia, R. R., Randel, W., Wu, F., Nagatani, R., Gleason, J., Thomason, L., and McCormick, L. R. P. P.: Ozone depletion at mid-altitudes: Coupling of volcanic aerosols and temperature variability to anthropogenic chlorine, Geophys. Res. Lett., 25, 1871–1874, doi:10.1029/98GL01293, 1998.

Solomon, S., Portmann, R. W., Sasaki, T., Hofmann, D. J., and Thompson, D. W. J.: Four decades of ozonesonde measurements over Antarctica, J. Geophys. Res., 110, D21311, doi:10.1029/2005JD005917, 2005.

Solomon, S., Plattner, G. K., Knutti, R., and Friedlingstein, P.: Irreversible climate change due to carbon dioxide emissions, Proc. Natl. Acad. Sci., 106, 1704–1709, doi:10.1073/pnas.0812721106, 2009.

Solomon, S., Rosenlof, K., Portmann, R., Daniel, J., Davis, S., Sanford, T., and Plattner, G.-K.: Contributions of stratospheric water vapor to decadal changes in the rate of global warming, Science, 327, 1219–1223, doi:10.1126/science.1182488, 2010.

Solomon, S., Ivy, D. J., Kinnison, D., Mills, M. J., Neely, R. R., and Schmidt, A.: Emergence of healing in the Antarctic ozone layer, Science, 353, 269–274, doi: 10.1126/science.aae0061, 2016a.

Solomon, S., Kinnison, D., Garcia, R. R., Bandoro, J., Mills, M., Wilka, C., Neely III, R. R., Schmidt, A., Barnes, J. E., Vernier, J.-P., and Hoepfner, M.: Monsoon circulations and tropical heterogeneous chlorine chemistry, Geophys. Res. Lett., 43, doi:10.1002/2016GL071778, 2016b.

Spang, R., Günther, G., Riese, M., Hoffmann, L., Müller, R., and Griessbach, S.: Satellite observations of cirrus clouds in the Northern Hemisphere lowermost stratosphere, Atmos. Chem. Phys., 15, 927–950, doi:10.5194/acp-15-927-2015, 2015.

SPP1689: Climate Engineering und unsere Klimaziele – eine überfällige Debatte, Schwerpunktprogramm 1689 der Deutschen Forschungs gemeinschaft "Climate Engineering: Risks, Challenges, Opportunities", `https://www.spp-climate-engineering.de`, last access: 19.09.2020, 2019.

Stenke, A. and Grewe, V.: Simulation of stratospheric water vapor trends: impact on stratospheric ozone chemistry, Atmos. Chem. Phys., 5, 1257–1272, doi:10.5194/acp-5-1257-2005, 2005.

Stocker, T. F., Qin, D., Plattner, G.-K., Tignor, M., Allen, S. K., Boschung, J., Nauels, A., Xia, Y., Bex, V., and Midgley, P. M., eds.: Climate Change 2013: The Physical Science Basis. Contribution of Working Group I to the Fifth Assessment Report of the Intergovernmental Panel on Climate Change, Cambridge University Press, Cambridge, UK and New York, NY, USA, 2013.

Stolarski, R. S., Krueger, A. J., Schoeberl, M. R., McPeters, R. D., Newman, P. A., and Alpert, J. C.: Nimbus 7 satellite measurements of the springtime Antarctic ozone decrease, Nature, 322, 808–811, doi:10.1038/322808a0, 1986.

Swinbank, R. and O'Neill, A.: A stratosphere-troposphere data assimilation system, Mon. Wea. Rev., 122, 686–702, doi:0.1175/1520-0493(1994)122⟨0686:ASTDAS⟩2.0. CO;2, 1994.

Telford, P., Braesicke, P., Morgenstern, O., and Pyle, J.: Reassessment of causes of ozone column variability following the eruption of Mount Pinatubo using a nudged CCM, Atmos. Chem. Phys., 9, 4251–4260, doi:10.5194/acp-9-4251-2009, 2009.

Thomason, L. W. and Peter, T., eds.: SPARC Report No. 4, SPARC Assessment of Stratospheric Aerosol Properties, WCRP-124,

WMO/TD-No.1295,   available   at: https://www.sparc-climate.org/wp-content/uploads/sites/5/2017/12/SPARC_Report_No4_Feb2006_ASAP.pdf   (last access: 21 May 2020), 2006.

Thomason, L. W., Poole, L. R., and Deshler, T.: A global climatoloy of stratospheric aerosol surface area density deduced from Stratospheric Aerosol and Gas Experiment II measurements: 1984-1994, J. Geophys. Res., 102, 8967–8976, doi:10.1029/96JD02962, 1997.

Thornton, B. F., Toohey, D. W., Tuck, A. F., Elkins, J. W., Kelly, K. K., Hovde, S. J., Richard, E. C., Rosenlof, K. H., Thompson, T. L., Mahoney, M. J., and Wilson, J. C.: Chlorine activation near the midlatitude tropopause, J. Geophys. Res., 112, D18 306, doi:10.1029/2006JD007640, 2007.

Tilmes, S., Müller, R., and Salawitch, R. J.: The sensitivity of polar ozone depletion to proposed geoengineering schemes, Science, 320, 1201–1204, doi:10.1126/science. 1153966, 2008.

Tilmes, S., Garcia, R. R., Kinnison, D. E., Gettelman, A., and Rasch, P. J.: Impact of geoengineered aerosols on the troposphere and stratosphere, J. Geophys. Res. A, 114, D12305, doi:10.1029/2008JD011420, 2009.

Tilmes, S., Kinnison, D. E., Garcia, R. R., Salawitch, R., Canty, T., Lee-Taylor, J., Madronich, S., and Chance, K.: Impact of very short-lived halogens on stratospheric ozone abundance and UV radiation in a geo-engineered atmosphere, Atmos. Chem. Phys., 12, 10 945–10 955, doi:10.5194/acp-12-10945-2012, 2012.

Tilmes, S., Jahn, A., Kay, J. E., Holland, M., and Lamarque, J.-F.: Can regional climate engineering save the summer Arctic sea ice?, Geophys. Res. Lett., 41, 880–885, doi:10.1002/2013GL058731, 2014.

Tilmes, S., Richter, J. H., Kravitz, B., MacMartin, D. G., Mills, M. J., Simpson, I. R., Glanville, A. S., Fasullo, J. T., Phillips, A. S., Lamarque, J.-F., et al.: CESM1 (WACCM) stratospheric aerosol geoengineering large ensemble project, Bull. Am. Meteorol. Soc., 99, 2361–2371, doi:10.1175/BAMS-D-17-0267.1, 2018.

Toon, O. B., Maring, H., Dibb, J., Ferrare, R., Jacob, D. J., Jensen, E. J., Luo, Z. J., Mace, G. G., Pan, L. L., Pfister, L., Rosenlof, K. H., Redemann, J., Reid, J. S., Singh, H. B., Thompson, A. M., Yokelson, R., Minnis, P., Chen, G., Jucks, K. W., and Pszenny, A.: Planning, implementation, and scientific goals of the Studies of Emissions and Atmospheric Composition, Clouds and Climate Coupling by Regional Surveys (SEAC4RS) field mission, J. Geophys. Res. A, 121, 4967–5009, doi:10.1002/2015JD024297, 2016.

Trapp, R. J., Diffenbaugh, N. S., and Gluhovsky, A.: Transient response of severe thunderstorm forcing to elevated greenhouse gas concentrations, Geophys. Res. Lett., 36, doi:10.1029/2008GL036203, 2009.

UNEP: Montreal Protocol on substances that deplete the ozone layer, United Nations Environmental Programme, Nairobi, Kenya, 1987.

Van Klooster, S. L. and Roebber, P. J.: Surface-Based Convective Potential in the Contiguous United States in a Business-as-Usual Future Climate, J. Climate, 22, 3317–3330, doi:10.1175/2009JCLI2697.1, 2009.

Visconti, G.: Fundamentals of physics and chemistry of the atmosphere, Springer, 2nd edn., doi:10.1007/978-3-319-29449-0, 2001.

Visioni, D., Pitari, G., and Aquila, V.: Sulfate geoengineering: a review of the factors controlling the needed injection of sulfur dioxide, Atmos. Chem. Phys., 17, 3879–3889, doi:10.5194/acp-17-3879-2017, 2017a.

Visioni, D., Pitari, G., Aquila, V., Tilmes, S., Cionni, I., Di Genova, G., and Mancini, E.: Sulfate geoengineering impact on methane transport and lifetime: results from the Geoengineering Model Intercomparison Project (GeoMIP), Atmos. Chem. Phys., 17, 11 209–11 226, doi:10.5194/acp-17-11209-2017, 2017b.

Visioni, D., MacMartin, D. G., Kravitz, B., Richter, J. H., Tilmes, S., and Mills, M. J.: Seasonally modulated stratospheric aerosol geoengineering alters the climate outcomes, Geophys. Res. Lett., 47, e2020GL088 337, doi:10.1029/2020GL088337, 2020.

Vogel, B., Müller, R., Deshler, T., Grooß, J.-U., Karhu, J., McKenna, D. S., Müller, M., Toohey, D., Toon, G. C., and Stroh, F.: Vertical profiles of activated ClO and ozone loss in the Arctic vortex in January and March 2000: In situ observations and model simulations, J. Geophys. Res., 108, 8334, doi:10.1029/2002JD002564, 2003.

Vogel, B., Pan, L. L., Konopka, P., Günther, G., Müller, R., Hall, W., Campos, T., Pollack, I., Weinheimer, A., Wei, J., Atlas, E. L., and Bowman, K. P.: Transport pathways and signatures of mixing in the extratropical tropopause region derived from Lagrangian model simulations, J. Geophys. Res., 116, D05306, doi:10.1029/2010JD014876, 2011.

Vogel, B., Günther, G., Müller, R., Grooß, J.-U., and Riese, M.: Impact of different Asian source regions on the composition of the Asian monsoon anticyclone and of the extratropical lowermost stratosphere, Atmos. Chem. Phys., 15, 13 699–13 716, doi:10.5194/acp-15-13699-2015, 2015.

Vogel, B., Günther, G., Müller, R., Grooß, J.-U., Afchine, A., Bozem, H., Hoor, P., Krämer, M., Müller, S., Riese, M., Rolf, C., Spelten, N., Stiller, G. P., Ungermann, J., and Zahn, A.: Long-range transport pathways of tropospheric source gases originating in Asia into the northern lower stratosphere during the Asian monsoon season 2012, Atmos. Chem. Phys., 16, 15 301–15 325, doi:10.5194/acp-16-15301-2016, 2016.

von Hobe, M., Grooß, J.-U., Günther, G., Konopka, P., Gensch, I., Krämer, M., Spelten, N., Afchine, A., Schiller, C., Ulanovsky, A., Sitnikov, N., Shur, G., Yushkov, V., Ravegnani, F., Cairo, F., Roiger, A., Voigt, C., Schlager, H., Weigel, R., Frey, W., Borrmann, S., Müller, R., and Stroh, F.: Evidence for heterogeneous chlorine activation in the tropical UTLS, Atmos. Chem. Phys., 11, 241–256, doi:10.5194/acp-11-241-2011, 2011.

Wales, P. A., Salawitch, R. J., Nicely, J. M., Anderson, D. C., Canty, T. P., Baidar, S., Dix, B., Koenig, T. K., Volkamer, R., Chen, D., Huey, L. G., Tanner, D. J., Cuevas, C. A., Fernandez, R. P., Kinnison, D. E., Lamarque, J.-F., Saiz-Lopez, A., Atlas, E. L., Hall, S. R., Navarro, M. A., Pan, L. L., Schauffler, S. M., Stell, M., Tilmes,

S., Ullmann, K., Weinheimer, A. J., Akiyoshi, H., Chipperfield, M. P., Deushi, M., Dhomse, S. S., Feng, W., Graf, P., Hossaini, R., Jöckel, P., Mancini, E., Michou, M., Morgenstern, O., Oman, L. D., Pitari, G., Plummer, D. A., Revell, L. E., Rozanov, E., Saint-Martin, D., Schofield, R., Stenke, A., Stone, K. A., Visioni, D., Yamashita, Y., and Zeng, G.: Stratospheric injection of brominated very short-lived substances: Aircraft observations in the western pacific and representation in global models, J. Geophys. Res. A, 123, 5690–5719, doi:10.1029/2017JD027978, 2018.

Wallace, J. M. and Hobbs, P. V.: Atmospheric Science: an Introductory Survey, vol. 92, Academic Press, 2nd edn., 2006.

Wang, P.-H., Cunnold, D. M., Zawodny, J. M., Pierce, R. B., Olson, J. R., Kent, G. S., and Skeens, K. M.: Seasonal ozone variations in the isentropic layer between 330 and 380 K as observed by SAGE II: Implications of extratropical cross-tropopause transport, J. Geophys. Res. A, 103, $28\,647$–$28\,659$, doi:10.1029/98JD02797, 1998.

Ward, M. K. M. and Rowley, D. M.: Kinetics of the $ClO + CH_3O_2$ reaction over the temperature range T=250–298 K, Phys. Chem. Chem. Phys., 18, $13\,646$–$13\,656$, doi:10.1039/c6cp00724d, 2016.

Webster, C. R., May, R. D., Trimble, C. A., Chave, R. G., and Kendall, J.: Aircraft laser infrared absorption spectrometer (ALIAS) for in situ atmospheric measurements of HCl, N_2O, CH_4, NO_2, and HNO_3, Appl. Opt., 33, 454–472, doi:10.1364/AO.33.000454, 1994.

Webster, C. R., May, R. D., Michelsen, H. A., Scott, D. C., Wilson, J. C., Jonsson, H. H., Brock, C. A., Dye, J. E., Baumgardner, D., Stimpfle, R. M., Koplow, J. P., Margitan, J. J., Proffitt, M. H., Jaeglé, L., Herman, R. L., Hu, H., Flesch, G. J., and Loewenstein, M.: Evolution of HCL concentrations in the lower stratosphere from 1991 to 1996 following the eruption of Mt. Pinatubo, Geophys. Res. Lett., 25, 995–998, doi:10.1029/98GL00548, 1998.

Weinstock, E. M., Smith, J. B., Sayres, D. S., Pittman, J. V., Spackman, J. R., Hintsa, E. J., Hanisco, T. F., Moyer, E. J., St Clair, J. M., Sargent, M. R., and

Anderson, J. G.: Validation of the Harvard Lyman-α in situ water vapor instrument: Implications for the mechanisms that control stratospheric water vapor, J. Geophys. Res. A, 114, doi:10.1029/2009JD012427, 2009.

Werner, B., Stutz, J., Spolaor, M., Scalone, L., Raecke, R., Festa, J., Colosimo, S. F., Cheung, R., Tsai, C., Hossaini, R., Chipperfield, M. P., Taverna, G. S., Feng, W., Elkins, J. W., Fahey, D. W., Gao, R.-S., Hintsa, E. J., D., T. T., Lee Moore, F., Navarro, M. A., Atlas, E., Daube, B. C., Pittman, J., Wofsy, S., and Pfeilsticker, K.: Probing the subtropical lowermost stratosphere and the tropical upper troposphere and tropopause layer for inorganic bromine, Atmos. Chem. Phys., 17, 1161–1186, doi:10.5194/acp-17-1161-2017, 2017.

Witze, A.: Rare ozone hole opens over Arctic – and it's big, Nature, 580, 18–19, doi:10.1038/d41586-020-00904-w, 2020.

WMO: Meteorology–A three?dimensional science, WMO Bull, pp. 134–138, 1957.

WMO: Scientific assessment of ozone depletion: 2014, Global Ozone Research and Monitoring Project–Report No. 55, Geneva, Switzerland, 2014.

WMO: Scientific assessment of ozone depletion: 2018, Global Ozone Research and Monitoring Project–Report No. 58, Geneva, Switzerland, 2018.

Yan, X., Konopka, P., Ploeger, F., Podglajen, A., Wright, J. S., Müller, R., and Riese, M.: The efficiency of transport into the stratosphere via the Asian and North American summer monsoon circulations, Atmos. Chem. Phys., 19, 15 629–15 649, doi:10.5194/acp-19-15629-2019, 2019.

Young, R. E., Houben, H., and Toon, O. B.: Radiatively forced dispersion of the Mt. Pinatubo volcanic cloud and induced temperature perturbations in the stratosphere during the first few months following the eruption, Geophys. Res. Lett., 21, 369–372, doi:10.1029/93GL03302, 1994.

Zafar, A. M., Müller, R., Grooß, J.-U., Robrecht, S., Vogel, B., and Lehmann, R.: The relevance of reactions of the methyl peroxy radical (CH_3O_2) and methylhypochlorite

(CH$_3$OCl) for Antarctic chlorine activation and ozone loss, Tellus B, 70, 1507 391, doi:10.1080/16000889.2018.1507391, 2018.

Zhang, R., Jayne, J. T., and Molina, M. J.: Heterogeneous interactions of ClONO$_2$ and HCl with sulfuric acid tetrahydrate: Implications for the stratosphere, J. Phys. Chem., 98, 867–874, 1994.

Appendix A

Chemical species and reactions in CLaMS

In the CLaMS setup used for this thesis, 42 chemical species and 131 reactions are considered. Besides N_2 and O_2 the species considered in CLaMS are given in Tab. A.1. The 131 considered reactions are allocated in 90 gas phase reactions, 30 photolysis reactions and 11 heterogeneous reactions listed below. The methyl group CH_3 is abbreviated as "Me" and in termolecular reactions 'M' stands for O_2 or N_2.

Table A.1: Overview on chemical species implemented in CLaMS besides N_2 and O_2. The methyl group CH_3 is abbreviated as "Me".

$O(^1D)$	NO	H	CH_4	Cl_2	Br_2
$O(^3P)$	NO_2	OH	CO	Cl	Br
O_3	NO_3	HO_2	CO_2	Cl_2O_2	BrCl
	N_2O_5	H_2O_2	HCHO	ClO	BrO
	HO_2NO_2	H_2	MeOO	OClO	HOBr
	HNO_3	H_2O	MeOOH	HOCl	HBr
	N_2O		MeOH	HCl	$BrONO_2$
			MeO_2NO_2	$ClONO_2$	
				$ClNO_2$	

- **Gas Phase reactions:**

$$O(^3P) + O_3 \ \rightarrow \ 2O_2$$

$$O(^1D) + O_2 \ \rightarrow \ O(^3P) + O_2$$

$$O(^1D) + N_2 \ \rightarrow \ O(^3P) + N_2$$

$$O(^1D) + H_2O \ \rightarrow \ 2OH$$

$$O(^1D) + H_2 \ \rightarrow \ OH + H$$

$$O(^1D) + CH_4 \ \rightarrow \ OH + MeOO$$

$$OH + O_3 \ \rightarrow \ HO_2 + O_2$$

$$OH + HO_2 \ \rightarrow \ H_2O + O_2$$

$$OH + H_2O_2 \ \rightarrow \ H_2O + HO_2$$

$$HO_2 + O_3 \ \rightarrow \ OH + O_2$$

$$2HO_2 \ \rightarrow \ H_2O_2 + O_2$$

$$O(^3P) + NO_2 \ \rightarrow \ NO + O_2$$

$$OH + NO_3 \ \rightarrow \ HO_2 + NO_2$$

$$OH + HNO_3 \ \rightarrow \ H_2O + NO_3$$

$$OH + HO_2NO_2 \ \rightarrow \ H_2O + NO_2$$

$$HO_2 + NO \ \rightarrow \ NO_2 + OH$$

$$HO_2 + NO_3 \ \rightarrow \ NO_2 + OH + O_2$$

$$NO + O_3 \ \rightarrow \ NO_2 + O_2$$

$$NO + NO_3 \ \rightarrow \ 2NO_2$$

$$NO_2 + O_3 \ \rightarrow \ NO_3 + O_2$$

$$OH + CH_4 \ \rightarrow \ MeOO + H_2O$$

$$OH + HCHO \ \rightarrow \ H_2O + CO$$

$$OH + MeOH \ \rightarrow \ H_2O + HCHO$$

$$OH + MeOOH \ \rightarrow \ MeOO + H_2O$$

$$\rightarrow \ HCHO + OH + H_2O$$

$$\begin{aligned}
HO_2 + MeOO &\rightarrow MeOOH + O_2 \\
MeOO + MeOO &\rightarrow MeOH + HCHO + O_2 \\
MeOO + NO &\rightarrow NO_2 + HCHO + H \\
MeOOH + Cl &\rightarrow HCl + HCHO + OH \\
O(^3P) + ClO &\rightarrow Cl + O_2 \\
OH + Cl_2 &\rightarrow HOCl + Cl \\
OH + ClO &\rightarrow HO_2 + Cl \\
&\rightarrow HCl + O_2 \\
OH + HCl &\rightarrow H_2O + Cl \\
OH + HOCl &\rightarrow H_2O + ClO \\
HO_2 + Cl &\rightarrow HCl + O_2 \\
&\rightarrow OH + ClO \\
HO_2 + ClO &\rightarrow HOCl + O_2 \\
&\rightarrow HCl + O_3 \\
Cl + O_3 &\rightarrow ClO + O_2 \\
Cl + H_2 &\rightarrow HCl + H \\
Cl + CH_4 &\rightarrow HCl + MeOO \\
Cl + HCHO &\rightarrow HCl + CO + HO_2 \\
Cl + MeOH &\rightarrow HCl + HCHO + H \\
Cl + OClO &\rightarrow 2ClO \\
Cl + HOCl &\rightarrow Cl_2 + OH \\
&\rightarrow ClO + HCl \\
Cl + ClONO_2 &\rightarrow Cl_2 + NO_3 \\
ClO + NO &\rightarrow NO_2 + Cl \\
ClO + MeOO &\rightarrow Cl + HCHO + HO_2 \\
O(^3P) + BrO &\rightarrow Br + O_2 \\
OH + HBr &\rightarrow H_2O + Br \\
HO_2 + Br &\rightarrow HBr + O_2
\end{aligned}$$

$$HO_2 + BrO \rightarrow HOBr + O_2$$

$$Br + O_3 \rightarrow BrO + O_2$$

$$Br + HCHO \rightarrow HBr + CO + HO_2$$

$$BrO + NO \rightarrow NO_2 + Br$$

$$BrO + ClO \rightarrow Br + OClO$$

$$\rightarrow Br + Cl + O_2$$

$$\rightarrow BrCl + O_2$$

$$2BrO \rightarrow 2Br + O_2$$

$$\rightarrow Br_2 + O_2$$

$$O(^3P) + HOBr \rightarrow OH + BrO$$

$$OH + Br_2 \rightarrow HOBr + Br$$

$$H + O_3 \rightarrow OH + O_2$$

$$H + HO_2 \rightarrow 2OH$$

$$\rightarrow H_2O + O(^3P)$$

$$\rightarrow H_2 + O_2$$

$$H_2 + OH \rightarrow H_2O + H$$

$$2OH \rightarrow H_2O + O(^3P)$$

$$OH + O(^3P) \rightarrow H + O_2$$

$$HO_2 + O(^3P) \rightarrow OH + O_2$$

$$H_2O_2 + O(^3P) \rightarrow OH + HO_2$$

$$HOCl + O(^3P) \rightarrow OH + ClO$$

$$N_2O + O(^1D) \rightarrow N_2 + O_2$$

$$\rightarrow 2NO$$

$$O(^3P) + O_2 + M \rightarrow O_3 + M$$

$$OH + NO_2 + M \rightarrow HONO_2 + M$$

$$HO_2 + NO_2 + M \rightarrow HO_2NO_2 + M$$

$$HO_2NO_2 + M \rightarrow HO_2 + NO_2 + M$$

$$NO_2 + NO_3 + M \rightarrow N_2O_5 + M$$

$$\begin{aligned}
\text{N}_2\text{O}_5 + \text{M} &\rightarrow \text{NO}_2 + \text{NO}_3 + \text{M} \\
\text{MeOO} + \text{NO}_2 + \text{M} &\rightarrow \text{MeO}_2\text{NO}_2 + \text{M} \\
\text{MeO}_2\text{NO}_2 + \text{M} &\rightarrow \text{MeOO} + \text{NO}_2 + \text{M} \\
\text{ClO} + \text{NO}_2 + \text{M} &\rightarrow \text{ClONO}_2 + \text{M} \\
\text{ClO} + \text{ClO} + \text{M} &\rightarrow \text{Cl}_2\text{O}_2 + \text{M} \\
\text{Cl}_2\text{O}_2 + \text{M} &\rightarrow 2\text{ClO} + \text{M} \\
\text{BrO} + \text{NO}_2 + \text{M} &\rightarrow \text{BrONO}_2 + \text{M} \\
\text{OH} + \text{CO} + \text{M} &\rightarrow \text{CO}_2 + \text{H} + \text{M} \\
\text{H} + \text{O}_2 + \text{M} &\rightarrow \text{HO}_2 + \text{M}
\end{aligned}$$

- **Photolyis:**

$$\begin{aligned}
\text{BrONO}_2 + \text{h}\nu &\rightarrow \text{BrO} + \text{NO}_2 \\
&\rightarrow \text{Br} + \text{NO}_3 \\
\text{BrCl} + \text{h}\nu &\rightarrow \text{Br} + \text{Cl} \\
\text{Cl}_2 + \text{h}\nu &\rightarrow 2\text{Cl} \\
\text{Cl}_2\text{O}_2 + \text{h}\nu &\rightarrow 2\text{Cl} + \text{O}_2 \\
\text{ClNO}_2 + \text{h}\nu &\rightarrow \text{Cl} + \text{NO}_2 \\
\text{ClONO}_2 + \text{h}\nu &\rightarrow \text{Cl} + \text{NO}_3 \\
&\rightarrow \text{ClO} + \text{NO}_2 \\
\text{H}_2\text{O}_2 + \text{h}\nu &\rightarrow 2\text{OH} \\
\text{HCHO} + \text{O}_2 + \text{h}\nu &\rightarrow \text{CO} + \text{HO}_2 + \text{H} \\
\text{HCHO} + \text{h}\nu &\rightarrow \text{H}_2 + \text{CO} \\
\text{HO}_2\text{NO}_2 + \text{h}\nu &\rightarrow \text{HO}_2 + \text{NO}_2 \\
&\rightarrow \text{OH} + \text{NO}_3
\end{aligned}$$

$$HOBr + h\nu \rightarrow OH + Br$$
$$HOCl + h\nu \rightarrow OH + Cl$$
$$HNO_3 + h\nu \rightarrow OH + NO_2$$
$$MeO_2NO_2 + h\nu \rightarrow MeOO + NO_2$$
$$MeOOH + O_2 + h\nu \rightarrow HCHO + OH + HO_2$$
$$N_2O_5 + h\nu \rightarrow NO_2 + NO_3$$
$$NO_2 + h\nu \rightarrow NO + O(^3P)$$
$$NO_3 + h\nu \rightarrow NO + O_2$$
$$\rightarrow NO_2 + O(^3P)$$
$$O_2 + h\nu \rightarrow 2O(^3P)$$
$$O_3 + h\nu \rightarrow O_2 + O(^3P)$$
$$\rightarrow O_2 + O(^1D)$$
$$OClO + h\nu \rightarrow O(^3P) + ClO$$
$$Br_2 + h\nu \rightarrow 2Br$$
$$HCl + h\nu \rightarrow H + Cl$$
$$H_2O + h\nu \rightarrow H + OH$$
$$N_2O + h\nu \rightarrow O(^1D) + N_2$$

- **Heterogeneous reactions:**

$$ClONO_2 + H_2O \xrightarrow{het.} HOCl + HNO_3$$
$$ClONO_2 + HCl \xrightarrow{het.} Cl_2 + HNO_3$$
$$HOCl + HCl \xrightarrow{het.} Cl_2 + H_2O$$
$$N_2O_5 + H_2O \xrightarrow{het.} 2HNO_3$$
$$N_2O_5 + HCl \xrightarrow{het.} ClNO_2 + HNO_3$$

$$\text{ClONO}_2 + \text{HBr} \xrightarrow{\text{het.}} \text{BrCl} + \text{HNO}_3$$

$$\text{BrONO}_2 + \text{HCl} \xrightarrow{\text{het.}} \text{BrCl} + \text{HNO}_3$$

$$\text{HOCl} + \text{HBr} \xrightarrow{\text{het.}} \text{BrCl} + \text{H}_2\text{O}$$

$$\text{HOBr} + \text{HCl} \xrightarrow{\text{het.}} \text{BrCl} + \text{H}_2\text{O}$$

$$\text{HOBr} + \text{HBr} \xrightarrow{\text{het.}} \text{Br}_2 + \text{H}_2\text{O}$$

$$\text{BrONO}_2 + \text{H}_2\text{O} \xrightarrow{\text{het.}} \text{HOBr} + \text{HNO}_3$$

Appendix B

Tracer-Tracer correlations

The mixing ratios of Cl_y and NO_y were initialized based on stratospheric tracer-tracer correlations taken from Grooß et al. (2014). Cl_y and NO_y were initialized based on a CH_4 measurement during the SEAC^{4}RS aircraft campaign. Initial Cl_y was calculated using the tracer-tracer correlation (Grooß et al., 2014)

$$\begin{aligned}[Cl_y] =& 2.510 + 3.517 \cdot [CH_4] - 3.741 \cdot [CH_4]^2 \\ &+ 0.4841 \cdot [CH_4]^3 + 0.03042 \cdot [CH_4]^4.\end{aligned} \tag{1}$$

The volume mixing ratio of Cl_y ($[Cl_y]$) is here in pptv and the mixing ratio of methane ($[CH_4]$) in ppmv.

To determine NO_y based on the CH_4 measurement, first N_2O was calculated through

$$\begin{aligned}[N_2O] =& -124.9 + 311.9 \cdot [CH_4] - 158.1 \cdot [CH_4]^2 \\ &+ 146.6 \cdot [CH_4]^3 - 43.92 \cdot [CH_4]^4\end{aligned} \tag{2}$$

assuming $[N_2O]$ in ppbv and $[CH_4]$ in ppmv (Grooß et al., 2002). Subsequently NO_y (in ppt) was calculated in a correlation with N_2O.

$$[\text{NO}_\text{y}] = 11.57 + 0.1235 \cdot [\text{N}_2\text{O}] - 1.013 \cdot 10^{-3} \cdot [\text{N}_2\text{O}]^2$$
$$+ 1.984 \cdot 10^{-6} \cdot [\text{N}_2\text{O}]^3 - 1.119 \cdot 10^{-9} \cdot [\text{N}_2\text{O}]^4 \tag{3}$$

In the MACPEX case, NO_y and Cl_y were initialized based on N_2O measurements. NO_y was calculated using the correlation in Eq. 3. Cl_y was calculated using Eq. 1. Therefore first CH_4 (im ppmv) had to be calculated based on a correlation (Eq. 4) with N_2O (in ppbv) (Grooß et al., 2014).

$$[\text{CH}_4] = 0.1917 + 0.01333 \cdot [\text{N}_2\text{O}] - 8.239 \cdot 10^{-5} \cdot [\text{N}_2\text{O}]^2$$
$$+ 2.840 \cdot 10^{-7} \cdot [\text{N}_2\text{O}]^3 - 3.376 \cdot 10^{-10} \cdot [\text{N}_2\text{O}]^4 \tag{4}$$

Appendix C

Maintenance of activated chlorine

In Sec. 4.2.2 chlorine catalysed ozone loss cycles are analysed and the maintenance of activated chlorine is described schematically based on Fig. 4.7. Here, the pathways leading to the maintenance of activated chlorine and low NO_x mixing ratios are described in more detail, including all radical balancing reactions. Since the pathway balancing HCl-formation and -destruction is coupled with the pathway balancing HNO_3-formation and -destruction, both are combined here. In total, two pathways are described, which balance HCl-formation and -destruction as well as HNO_3-formation and -destruction, and which mainly differ in the reaction of the methylperoxy radical ($H_3COO + NO$, R 35, or $H_3COO + ClO$, R 36).

At water vapour mixing ratios slightly higher than the water vapour threshold, H_3COO reacts rather with NO. Hence, pathway AC1 mainly balances HCl and ClO_x as well as HNO_3 and NO_x.

$$
\begin{aligned}
\mathrm{Cl} + \mathrm{CH_4} &\rightarrow \mathrm{HCl} + \mathrm{CH_3} & \mathrm{(R\,24)} \\
\mathrm{CH_3} + \mathrm{O_2} &\rightarrow \mathrm{H_3COO} & \mathrm{(R\,39)} \\
\mathrm{H_3COO} + \mathrm{NO} &\rightarrow \mathrm{NO_2} + \mathrm{H_3CO} & \mathrm{(R\,35)} \\
\mathrm{H_3CO} + \mathrm{O_2} &\rightarrow \mathrm{HCHO} + \mathrm{HO_2} & \mathrm{(R\,40)} \\
\mathrm{ClO} + \mathrm{NO_2} + \mathrm{M} &\rightarrow \mathrm{ClONO_2} + \mathrm{M} & \mathrm{(R\,30)} \\
\mathrm{ClONO_2} + \mathrm{HCl} &\xrightarrow{\text{het.}} \mathrm{HNO_3} + \mathrm{Cl_2} & \mathrm{(R\,21)} \\
\mathrm{OH} + \mathrm{HNO_3} &\rightarrow \mathrm{H_2O} + \mathrm{NO_3} & \mathrm{(R\,33)} \\
\mathrm{Cl_2} + \mathrm{h}\nu &\rightarrow 2\,\mathrm{Cl} & \mathrm{(R\,31)} \\
2 \times (\mathrm{Cl} + \mathrm{O_3} &\rightarrow \mathrm{ClO} + \mathrm{O_2}) & \mathrm{(R\,16)} \\
\mathrm{NO_2} + \mathrm{h}\nu &\rightarrow \mathrm{NO} + \mathrm{O(^3P)} & \mathrm{(R\,12)} \\
\mathrm{NO_3} + \mathrm{h}\nu &\rightarrow \mathrm{NO_2} + \mathrm{O(^3P)} & \mathrm{(R\,41)} \\
\mathrm{HO_2} + \mathrm{ClO} &\rightarrow \mathrm{HOCl} + \mathrm{O_2} & \mathrm{(R\,19)} \\
\mathrm{HOCl} + \mathrm{h}\nu &\rightarrow \mathrm{OH} + \mathrm{Cl} & \mathrm{(R\,20)} \\
2 \times (\mathrm{O(^3P)} + \mathrm{O_2} + \mathrm{M} &\rightarrow \mathrm{O_3} + \mathrm{M}) & \mathrm{(R\,2)}
\end{aligned}
$$

$$
\text{net: } \mathrm{CH_4} + \mathrm{O_2} \rightarrow \mathrm{HCHO} + \mathrm{H_2O} \qquad \mathrm{(AC1)}
$$
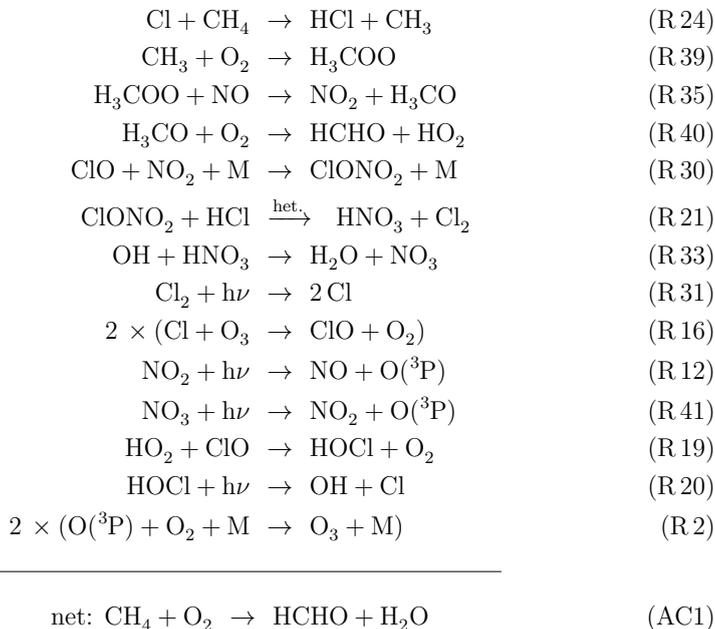
In pathway AC1, HCl is formed in R 24. The methylradical formed in R 24 reacts fastly with oxygen in R 39 yielding a methylperoxy radical $\mathrm{H_3COO}$, which reacts with NO in R 35. In reaction R 30 $\mathrm{ClONO_2}$ is formed, which reacts with HCl heterogeneously in R 21 (and thus leads to an HCl depletion). $\mathrm{HNO_3}$ formed in R 21 is depleted in R 33 reacting with the OH-radical. These reactions constitute the balance between HCl and $\mathrm{HNO_3}$-formation and -destruction. The reactions R 31 and R 16 balance the $\mathrm{ClO_x}$-species, R 12 and R 41 the $\mathrm{NO_x}$-species, reactions R 19 and R 20 the $\mathrm{HO_x}$-species and R 2 odd oxygen ($\mathrm{O_x}$). All of these radical reactions are significantly faster than the reactions, which constitute the balance between HCl and $\mathrm{HNO_3}$ formation and destruction. The net reaction of this pathway is the oxidation of $\mathrm{CH_4}$ to HCHO (formaldehyde).

In cycle AC1 the $\mathrm{H_3COO}$-radical reacts with NO (R 35). As an alternative the $\mathrm{H_3COO}$-radical reacts with ClO (R 36) at high water vapour mixing ratios yielding cycle AC2 as balance between HCl and $\mathrm{HNO_3}$ formation and destruction.

$$\begin{aligned}
\text{Cl} + \text{CH}_4 &\rightarrow \text{HCl} + \text{CH}_3 & \text{(R\,24)} \\
\text{CH}_3 + \text{O}_2 &\rightarrow \text{H}_3\text{COO} & \text{(R\,39)} \\
\text{H}_3\text{COO} + \text{ClO} &\rightarrow \text{HCHO} + \text{HO}_2 + \text{Cl} & \text{(R\,36)} \\
\text{ClO} + \text{NO}_2 + \text{M} &\rightarrow \text{ClONO}_2 + \text{M} & \text{(R\,30)} \\
\text{ClONO}_2 + \text{HCl} &\xrightarrow{het.} \text{HNO}_3 + \text{Cl}_2 & \text{(R\,21)} \\
\text{OH} + \text{HNO}_3 &\rightarrow \text{H}_2\text{O} + \text{NO}_3 & \text{(R\,33)} \\
\text{Cl}_2 + \text{h}\nu &\rightarrow 2\,\text{Cl} & \text{(R\,31)} \\
3 \times (\text{Cl} + \text{O}_3 &\rightarrow \text{ClO} + \text{O}_2) & \text{(R\,16)} \\
\text{HO}_2 + \text{ClO} &\rightarrow \text{HOCl} + \text{O}_2 & \text{(R\,19)} \\
\text{HOCl} + \text{h}\nu &\rightarrow \text{OH} + \text{Cl} & \text{(R\,20)} \\
\text{O}(^3\text{P}) + \text{O}_2 + \text{M} &\rightarrow \text{O}_3 + \text{M} & \text{(R\,2)}
\end{aligned}$$

$$\text{net: } \text{CH}_4 + 2\,\text{O}_3 \rightarrow \text{HCHO} + \text{H}_2\text{O} + 2\,\text{O}_2 \qquad \text{(AC2)}$$
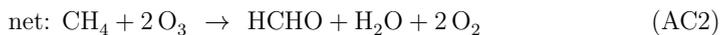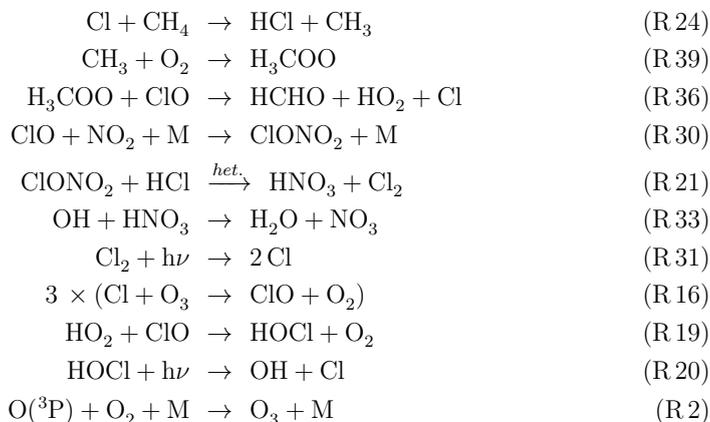
The main difference between pathway AC1 and AC2 is the reaction of the H_3COO-radical. The reactions R 24, R 39, R 30, R 21 and R 33 balance HCl and ClO_x as well as HNO_3 and NO_x. The reactions R 31, R 16, R 19, R 20 and R 2 convert the radical species and are very fast. The net reaction of this pathway is the oxidation of methane (CH_4) into formaldehyde (HCHO) with a simultaneous ozone destruction. Since the ozone destruction due to the catalytic ozone loss cycles discussed in Sec. 4.2.2 is much faster, the ozone destruction in AC2 is negligible compared to the ozone loss cycles discussed in Sec. 2.3.

Appendix D

MACPEX case

The MACPEX (Mid-latitude airborne Cirrus Properties EXperiment) case is conducted to complement the results obtained from the standard case (Sec. 4.3) as a further example for an event with high stratospheric water vapour based on airborne measurements. In this section, first the model setup for the MACPEX case is described. In a second step, the results of model calculations of the MACPEX case are presented, comprising the chosen trajectory for chemical simulations and the sensitivity of ozone chemistry to various conditions.

D.1   Model Setup

Simulations are performed similar to the SEAC[4]RS case (see. Sec. 4.1) based on measurements with enhanced water vapour of at least $10\,\mathrm{ppmv}$ taken during the MACPEX campaign (Rollins et al., 2014). Chemistry is calculated for single air parcels along trajectories including diabatic descent. Trajectories are calculated as described in Sec. 4.1.2. For chemical initialization, important trace gases for ozone chemistry – O_3, Cl_y and NO_y – are initialized based on MACPEX measurements. Ozone and water vapour were measured directly during the aircraft campaign, Cl_y and NO_y are inferred from tracer-tracer relations using N_2O measured on the aircraft employed. The initialization of all further trace gases except of water vapour were taken from the full chemistry

3D-CLaMS simulation (Vogel et al., 2015, 2016) for summer 2012 at the location of the
measurement. Chemistry was initialized 7 days before the measurement.

The MACPEX campaign (Rollins et al., 2014) took place in the spring 2011 and was
based at Houston, Texas. The water vapour values used here were measured by the Fast
In-situ Stratospheric Hygrometer (FISH), which employs the Lyman-α photofragment
fluorescence technique (Meyer et al., 2015). MACPEX ozone was measured by the
UAS-O_3 instrument (Gao et al., 2012). Initial Cl_y and NO_y were assumed based on
tracer-tracer correlations with N_2O that was measured by the Jet Propulsion Labora-
tory's Aircraft Laser Infrared Absorption Spectrometer (ALIAS) instrument (Webster
et al., 1994).

Initial Cl_y and NO_y is calculated based on N_2O tracer-tracer correlations (Grooß et al.,
2014, see also App. B) with corrections considering a N_2O increase from 2009 to 2013.
Cl_y is determined using the same correlation with CH_4 as for the standard case (see
Sec. 4.1.3). Therefore CH_4 is first calculated using measured N_2O of 320.28 ppbv and
a correlation based on measurements from 2009 (Grooß et al., 2014). The increase
of stratospheric CH_4 and N_2O is considered as described for the standard case (GHG
Bulletin, 2014). First, an increase in N_2O of 1.6 ppbv from 2009 to 2011 is estimated to
adjust N_2O. Furthermore calculated CH_4 is adjusted considering a difference between
CH_4 in 2000 and 2009 of 0.026 ppmv. The annual decrease of Cl_y from 2000 to 2011 is
assumed to be 0.8% (WMO, 2014). A summary of the initial values for main tracers
assumed in the MACPEX case are given in Table D.1. Furthermore sensitivity studies
assuming only 80% of initial Cl_y (0.8 Cl_y), 80% of initial NO_y (0.8 NO_y), and an elevated
H_2SO_4-background (0.6 ppbv H_2SO_4) are conducted.

D.2   Results of MACPEX simulations

During the MACPEX campaign only few cases with enhanced stratospheric water
vapour were observed. Here an example is presented for a trajectory calculated based
on such a case. This trajectory is used to test the sensitivity of lowermost stratospheric

Table D.1: Mixing ratios and sources used for initialization of relevant trace gases for the MACPEX case. Cl_y and NO_y values were determined based on tracer-tracer correlations (see text). Initial mixing ratios of ClO_x species were assumed to be zero.

Species	Value	Source
O_3	283.0 ppbv	UAS-O_3
CH_4	1.68 ppmv	CLaMS-3D
CO	19.0 ppbv	CLaMS-3D
Cl_y	55 pptv	tracer corr.
HCl	52.7 pptv	tracer corr.
$ClONO_2$	2.19 pptv	tracer corr.
NO_y	620 pptv	tracer corr.
HNO_3	390.3 pptv	tracer corr.
NO	114.6 pptv	tracer corr.
NO_2	114.6 pptv	tracer corr.
Br_y	1.2 pptv	CLaMS-3D
H_2O	5–20 ppmv	
H_2SO_4	0.2 ppbv, 0.6 ppbv	

ozone in mid-latitudes on the water vapour, Cl_y and NO_y mixing ratio and on an enhancement of stratospheric sulfate.

D.2.1 MACPEX Trajectory

The selected trajectory for the MACPEX case is shown in Fig. D.1. It refers to a measurement on 11 April 2011 during the MACPEX campaign. In the left panel, a backward trajectory is presented in the range of -7 to 0 days from the time of measurement and a forward trajectory in the range from 0 to 7 days. In the right panel, the location of the measurement is shown by a red square.

The potential temperature level of this trajectory is around 380 K and above the tropopause located at $\sim$350 K, which was deduced from the temperature profile measured during the flight on 11 April 2011. The forward trajectory shows a strongly increasing
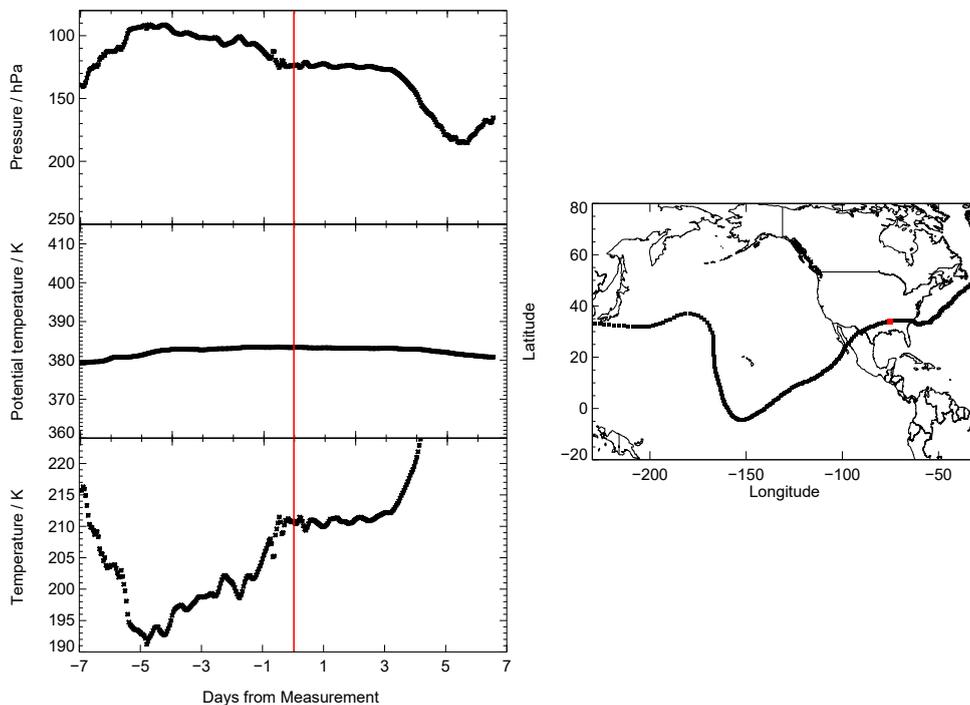
Figure D.1: Pressure, potential temperature, temperature and location of the selected trajectory calculated based on measurements with enhanced water vapour during the MACPEX aircraft campaign. The red line (left panels) marks the time of measurement and the red squares (right panels) mark the location of the measurement. Since the tropopause is very low, it is not plotted here. In the right panel, the begin of the trajectory (4. April 2011) is at the left edge of the panel. In the bottom panel (left), the MACPEX trajectory consists of single squares due to a faster movement of the air parcel in that region.

temperature and pressure level due to a decrease in altitude. Coming from the Western Pacific, this air parcel passes the North American continent briefly. The backward trajectory reaches very low temperatures with a minimum temperature of 191 K. Because of its low temperature, which promotes the occurrence of heterogeneous reactions, the backward trajectory is chosen as a second example for the sensitivity of lowermost stratospheric ozone to a variety of conditions.
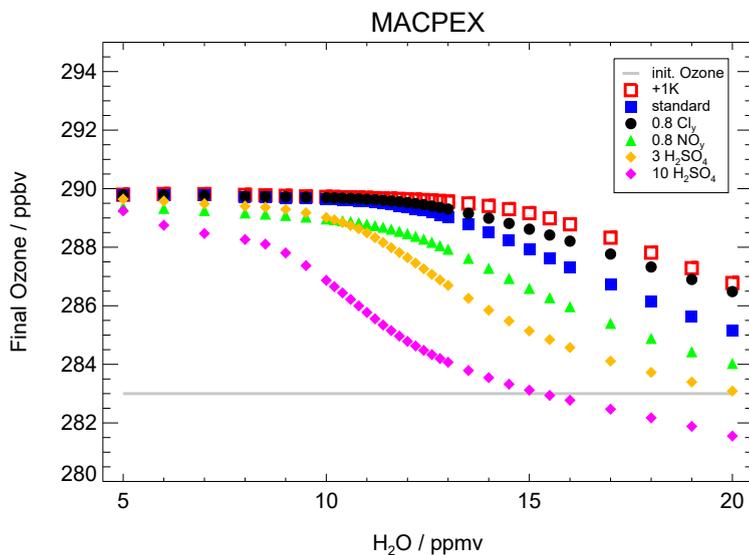
Figure D.2: Impact of the water vapour content on the ozone mixing ratio (final ozone) reached at the end of the 7-day simulation along the MACPEX trajectory. The standard case is shown in blue and the initial ozone amount is marked by the grey line. An impact on the final ozone mixing ratios is observable after exceeding a critical threshold in water vapour. This threshold changes with a shift in the temperature (+1K, red), the Cl_y mixing ratio to $0.8\,Cl_y$ (black), the NO_y mixing ratio ($0.8\,NO_y$, green) and the sulfate content ($3\times$ standard H_2SO_4, yellow, $10\times$ standard H_2SO_4, pink).

D.2.2   Sensitivity studies

Chemical simulations assuming the MACPEX initialization (Tab. D.1) and a water vapour mixing ratio varying between 5 and 20 ppmv are perfomed along the MACPEX 7-day backwards trajectory. Final ozone, reached at the end of this simulations, is shown as blue squares in Fig. D.2.

The water vapour threshold necessary for chlorine activation to occur is reached at 8 ppmv H_2O. It is a lower water vapour mixing ratio than for the SEAC[4]RS case, beacause of the very low temperatures reached. For the MACPEX trajectory and 8 ppmv H_2O, the time until chlorine is activated takes 63 h from the begin of the trajectory. Because of increasing temperatures (see Fig. D.2), chlorine activation can be maintained for 14 h at this water vapour mixing ratio. Hence, no decrease of final ozone can be observed during this simulation. For higher water vapour mixing ratios,

chlorine activation is maintained for a longer time and final ozone is reduced comparing with final ozone reached for low water vapour mixing ratios.

In general, the decrease in final ozone is much lower for the MACPEX case than for the SEAC[4]RS case. In the MACPEX initialization, Cl_y accounts to as a third of Cl_y in the SEAC[4]RS initialization. Hence, catalytic ozone loss has lower rates for MACPEX conditions and ozone is less affected by chlorine activation. Even assuming a high water vapour mixing ratio of 20 ppmv yields higher final ozone than initial ozone for MACPEX conditions. Although chlorine is activated in the MACPEX case, no net ozone destruction occurs.

The impact of changes in sulfate, Cl_y and NO_y is tested for the MACPEX case, as well. The changes affect the water vapour threshold in the same way as in the SEAC[4]RS case. An enhancement of sulfate (Fig. 4.8, left, yellow and pink diamonds), and a reduction of NO_y (green triangles) shifts the water vapour threshold to lower water vapour mixing ratios. A reduction of Cl_y (black circles) shifts it to higher water vapour mixing ratios. Thus, the sensitivities to ozone in the MACPEX case agree with those in the SEAC[4]RS simulation (Chapter 4).

Appendix E

Comparison of the GLENS mixing layer with START08 measurements

In Sec. 5.2.1, the GLENS results for conditions in the mixing layer between tropospheric and stratospheric air were compared with measurements of the SEAC[4]RS campaign. In addition, GLENS results of the mixing layer today (case C2010) are compared with measurements of the Stratosphere-Troposphere Analyses of Regional Transport (START08) aircraft campaign (Pan et al., 2010). START08 aimed to investigate the stratosphere-to-troposphere transport focussing on stratospheric intrusions into the troposphere and tropospheric intrusions transporting air masses from the upper tropical troposphere to the extra-tropical lowermost stratosphere. Flights during START08 took place from April – June 2008 and covered the area above central North America (25–65°N, 80–120°W) up to an altitude of ∼14.3 km (Pan et al., 2010).

In Fig. E.1, the GLENS tracer-tracer-correlation of the GLENS mixing layer in case C2010 is compared with the mixing layer deduced from START08 measurements. Air masses corresponding to the mixing layer between stratospheric and tropospheric air are assumed to be located above the thermal tropopause estimated based on the temperature–altitude profile during the flight. In addition they are selected to show more than 30 ppbv CO and more than 150 ppbv O_3. In contrast to the SEAC[4]RS mixing layer (Sec. 5.2.1), the ozone criteria is added to determine the mixing layer from START08 measurements, because many data points above the tropopause deduced

from temperatures measured during the flight exhibited very low ozone mixing ratios indicating a high fraction of air from the troposphere above the tropopause. This tropospheric air masses crossing the thermal tropopause were aimed to be probed during the START08 campaign.

The comparison of the stratospheric GLENS E90-O_3-correlation with the START08 CO-O_3-correlation is shown in black in Fig. E.1 (top). In contrast to GLENS results, ozone measurements during START08 only reach up to $\sim$1400 ppbv O_3, because of the limitation of the probed altitude by the maximum flight height of $\sim$14.3 km. However, the mixing layer in GLENS (red) comprises a similar ozone range as the mixing layer deduced from START08 measurements.

In Fig E.1 (middle), the H_2O-temperature correlation (left) and the H_2O-O_3 correlation (right) for the entire latitude region considered in this study is shown for the GLENS results. Fig E.1 (bottom) shows the same correlations for the mixing layer deduced from START08 measurements. GLENS results show an overall agreement with START08 measurements. The water vapour mixing ratio exceeds in both model results and measurements more than 30 ppmv and the ozone mixing ratio ranges mainly between 300 and 500 ppbv. However, GLENS temperatures are somewhat lower than temperatures measured during START08.
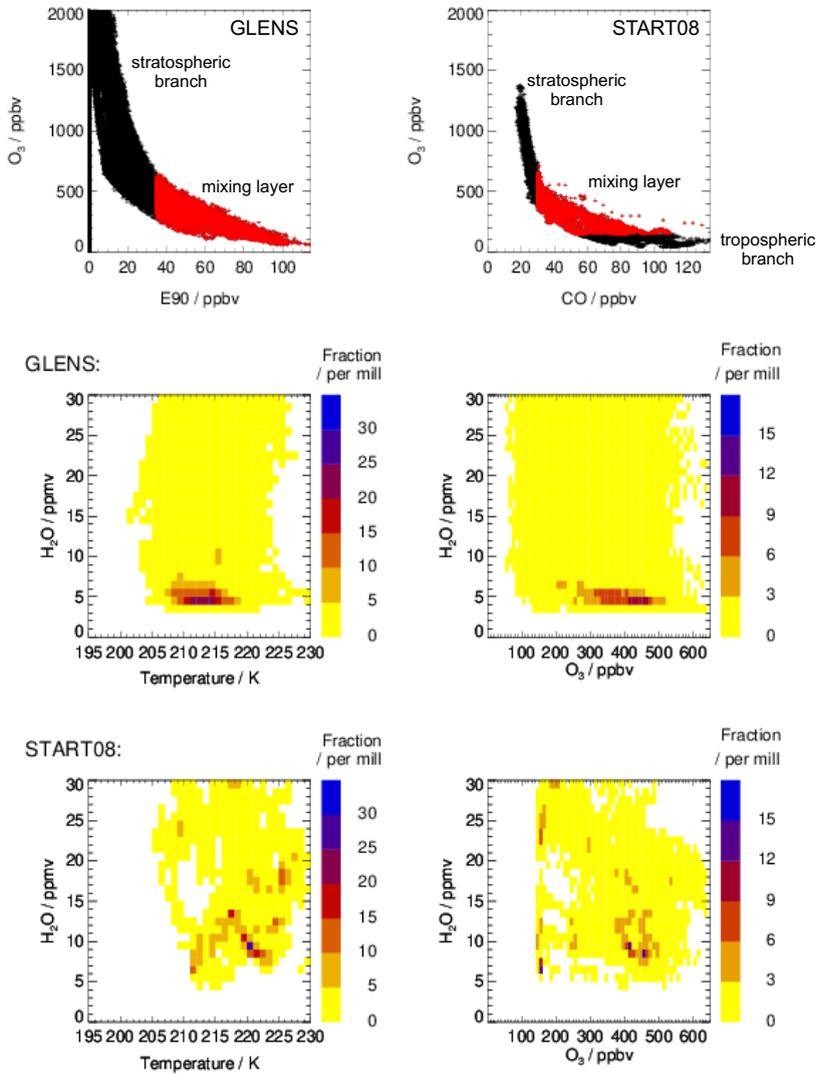
Figure E.1: Comparison of the GLENS mixing layer between stratospheric and tropospheric air masses of the C2010 case with measurements of the START08 aircraft campaign. Top panels show the E90-O_3 correlation of GLENS air masses (left) and the CO-O_3-relative frequency distribution of START08 measurements (right) for stratospheric air masses (black) and air masses corresponding to the mixing layer (red). The middle panels show the relative frequency distribution in the H_2O-Temperature (left) and the H_2O-O_3 (right) correlation of the GLENS mixing layer and bottom panels of the mixing layer deduced from START08 measurements.

Appendix F

Abbreviations and Glossary

Activated chlorine ClO_x contributes 10% or more to Cl_y

Albedo   Measure for the reflexivity of the Earth surface

BDC   Brewer-Dobson-Circulation: meridional stratospheric circulation causing an upwards transport of air masses in the tropics and a downwelling in middle and high latitudes

BrO_x Reactive bromine species, BrO_x=Br+BrO

CFC   Chlorofluorocarbon

Chlorine activation   Transformation of Cl_y reservoir species (HCl, $ClONO_2$) into ClO_x radicals

Chlorine activation threshold   here: Array of water vapour mixing ratios and temperatures, which divide atmospheric conditions in those leading or not leading to chlorine activation

Chlorine deactivation	Transformation of ClO_x radicals into Cl_y reservoir species (HCl, $ClONO_2$)
CLaMS	Chemical Lagrangian Model of the Stratosphere
ClO_x	Reactive chlorine species, $ClO_x = Cl + ClO + 2 \times Cl_2O_2$
Convective overshooting	here: vertical transport passing through the tropopause in mid-latitudes
EESC	Equivalent effective stratospheric chlorine: a measure for the ozone depleting effect of all stratospheric halogen compounds
GLENS	Geoengineering Large ENsemble Simulations
Geoengineering	Term for several techniques consciously interfering the Earth climate for attenuating the effects of climate change
HCl-null-cycle	Reaction cycle, which balances HCl formation and destruction and thus maintains activated chlorine conditions
HO_x	Reactive hydrogen species, $HO_x = OH + H + HO_2$
Lowermost stratosphere	Lowest part of the stratosphere, where mixing between stratospheric and tropospheric air masses can occur

MACPEX	Mid-latitude airborne Cirrus Properties Experiment, aircraft campaign above North America
Montreal Protocol	Convention of all countries to reduce CFC emissions
Mt. Pinatubo eruption	Strong volcanic eruption in the year 1991 which reduced the global mean temperature significantly in the subsequent year
Net chlorine activation	The rate of chlorine activation exceeds the rate of chlorine deactivation
NO_x	Reactive nitrogen species, $NO_x = NO + NO_2 + NO_3$
ODS	Ozone Depleting Substances
O_x	Reactive oxygen species, $O_x = O_3 + O(^3P) + O(^1D)$
Ozone column	Sum of all ozone within a column above a specific area of the Earth surface
Ozone hole	Large area in which column ozone is almost completely destroyed during Antarctic winter
Ozone layer	Altitude of 15–30 km in which most atmospheric ozone is located
RCP8.5	Representative Concentration Pathway 8.5: A worst case scenario for human made greenhouse gas emissions where the global mean temperature increases $\sim 5\,K$ until the year 2100

Relative frequency distribution   here: The relative distribution of occurrence frequency of data points in a $1\,\mathrm{K}$ $(10\,\mathrm{ppbv}\ O_3)\times 1\,\mathrm{ppmv}$ H_2O bin in the temperature-water vapour (ozone-water vapour) correlation. The number of data points of each bin is normalized by the total number of considered data

SEAC^{4}RS   Studies of Emissions and Atmospheric Composition, Clouds and Climate Coupling by Regional Surveys: aircraft campaign above North America

Standard case   here: Reference assumption for analysing the chemical ozone loss mechanism potentially occurring in the mid-latitude lowermost stratosphere during summer

Sulfate geoengineering   Injection of sulfate aerosols into the stratosphere to reduce the light, which reaches the earth surface, and thus to cool the Earth surface temperature down

Thermal tropopause   Lowest altitude level at which the temperature decreases to $2\,\mathrm{K/km}$ or less with altitude (WMO, 1957)

Trajectory   Describes the movement and time dependent conditions in an air parcel

Tropopause   Boundary between troposphere and stratosphere, which in general forms a transport barrier

Troposphere	Lowest layer of the Earth atmosphere, which reaches from the ground up to an altitude of 6–9 km in polar regions and of 16–18 km in the tropics. In the troposphere temperatures decrease with increasing altitude
WACCM	Whole Atmosphere Community Climate Model
Water vapour threshold	here: Lowest water vapour mixing ratio at which chlorine activation can occur for a specific temperature

Band / Volume 533
**Mechanische Eigenschaften von katalysatorbeschichteten Membranen
für die Polymer-Elektrolyt-Membran Elektrolyse**
E. Borgardt (2021), viii, 181 pp
ISBN: 978-3-95806-533-8

Band / Volume 534
**Techno-economic Assessment of Hybrid Post-combustion Carbon
Capture Systems in Coal-fired Power Plants and Steel Plants**
Y. Wang (2021), IV, xx, 230 pp
ISBN: 978-3-95806-545-1

Band / Volume 535
**Wissenschaftliche Begleitstudie der Wasserstoff Roadmap
Nordrhein-Westfalen**
S. Cerniauskas, P. Markewitz, J. Linßen, F. Kullmann, T. Groß,
P. Lopion, P-M. Heuser, T. Grube, M. Robinius und D. Stolten
(2021), IV, 89 pp
ISBN: 978-3-95806-547-5

Band / Volume 536
**High-Resolution Photocurrent Mapping of Thin-Film Silicon Solar Cells
Using Scanning Near-Field Optical Microscopy**
Z. Cao (2021), xiii, 148 pp
ISBN: 978-3-95806-548-2

Band / Volume 537
**Kompressionseigenschaften der Gasdiffusionslage einer
Hochtemperatur-Polymerelektrolyt-Brennstoffzelle**
E. Hoppe (2021), viii, 153 pp
ISBN: 978-3-95806-549-9

Band / Volume 538
Transparent Passivating Contact for Crystalline Silicon Solar Cells
M. Köhler (2021), 186 pp
ISBN: 978-3-95806-550-5

Band / Volume 539
Distribution of trace gases with adverse effects on fuel cells
D. Klemp, R. Wegener, R. Dubus, L. Karadurmus, N. Kille, Z. Tan (2021),
160 pp
ISBN: 978-3-95806-551-2

JÜLICH
Forschungszentrum